

# Perforated Ground Plane Structures for RF and Wireless Components

Guest Editors: Haiwen Liu, Lei Zhu, Dal Ahn, Amin Abbosh, and Sha Luo





---

# **Perforated Ground Plane Structures for RF and Wireless Components**

International Journal of Antennas and Propagation

---

## **Perforated Ground Plane Structures for RF and Wireless Components**

Guest Editors: Haiwen Liu, Lei Zhu, Dal Ahn, Amin Abbosh,  
and Sha Luo



---

Copyright © 2013 Hindawi Publishing Corporation. All rights reserved.

This is a special issue published in “International Journal of Antennas and Propagation.” All articles are open access articles distributed under the Creative Commons Attribution License, which permits unrestricted use, distribution, and reproduction in any medium, provided the original work is properly cited.

## Editorial Board

M. Ali, USA  
Charles Bunting, USA  
Felipe Cátedra, Spain  
Dau-Chyrh Chang, Taiwan  
Deb Chatterjee, USA  
Z. N. Chen, Singapore  
Michael Yan Wah Chia, Singapore  
Christos Christodoulou, USA  
Shyh-Jong Chung, Taiwan  
Lorenzo Crocco, Italy  
Tayeb A. Denidni, Canada  
Antonije R. Djordjevic, Serbia  
Karu P. Esselle, Australia  
Francisco Falcone, Spain  
Miguel Ferrando, Spain  
Vincenzo Galdi, Italy  
Wei Hong, China  
Hon Tat Hui, Singapore  
Tamer S. Ibrahim, USA  
Shyh-Kang Jeng, Taiwan

Mandeep Jit Singh, Malaysia  
Nemai Karmakar, Australia  
Se-Yun Kim, Republic of Korea  
Ahmed A. Kishk, Canada  
Tribikram Kundu, USA  
Byungje Lee, Republic of Korea  
Ju-Hong Lee, Taiwan  
L. Li, Singapore  
Yilong Lu, Singapore  
Atsushi Mase, Japan  
Andrea Massa, Italy  
Giuseppe Mazzeola, Italy  
Derek McNamara, Canada  
C. F. Mecklenbräuker, Austria  
Michele Midrio, Italy  
Mark Mirotznik, USA  
Ananda S. Mohan, Australia  
P. Mohanan, India  
Pavel Nikitin, USA  
A. D. Panagopoulos, Greece

Matteo Pastorino, Italy  
Massimiliano Pieraccini, Italy  
Sadasiva M. Rao, USA  
Sembiam R. Rengarajan, USA  
Ahmad Safaai-Jazi, USA  
Safieddin Safavi Naeini, Canada  
Magdalena Salazar-Palma, Spain  
Stefano Selleri, Italy  
Krishnasamy T. Selvan, India  
Zhongxiang Q. Shen, Singapore  
John J. Shynk, USA  
Seong-Youp Suh, USA  
Parveen Wahid, USA  
Yuanxun Ethan Wang, USA  
Daniel S. Weile, USA  
Quan Xue, Hong Kong  
Tat Soon Yeo, Singapore  
Jong Won Yu, Republic of Korea  
Wenhua Yu, USA  
Anping Zhao, China

# Contents

**Perforated Ground Plane Structures for RF and Wireless Components**, Haiwen Liu, Lei Zhu, Dal Ahn, Amin Abbosh, and Sha Luo

Volume 2013, Article ID 709310, 2 pages

**Analysis of High  $T_c$  Superconducting Rectangular Microstrip Patches over Ground Planes with Rectangular Apertures in Substrates Containing Anisotropic Materials**, Abderraouf Messai,

Siham Benkouda, Mounir Amir, Sami Bedra, and Tarek Fortaki

Volume 2013, Article ID 169893, 7 pages

**A Defected Ground Structure without Ground Contact Problem and Application to Branch Line Couplers**, Jongsik Lim, Dal Ahn, Sang-Min Han, Yongchae Jeong, and Haiwen Liu

Volume 2013, Article ID 232317, 5 pages

**Flexible Microwave Tag System Based on DGS Multiple Resonators**, Seok-Jae Lee, Jongsik Lim, Dal Ahn, and Sang-Min Han

Volume 2013, Article ID 415607, 7 pages

**Differential and Single-Ended Microstrip Lines Loaded with Slotted Magnetic-LC Resonators**, J. Naqui, M. Durán-Sindreu, and F. Martín

Volume 2013, Article ID 640514, 8 pages

**Impact of the Gate Width of  $\text{Al}_{0.27}\text{Ga}_{0.73}\text{N}/\text{AlN}/\text{Al}_{0.04}\text{Ga}_{0.96}\text{N}/\text{GaN}$  HEMT on Its Characteristics**, Liwei Jin, Zhiquan Cheng, and Qingna Wang

Volume 2013, Article ID 738659, 3 pages

**A Miniaturized Dual-Mode Bandpass Filter Using Slot Spurline Technique**, Haiwen Liu, Jiuhuai Lei, Jing Wan, Yan Wang, Feng Yang, and Suping Peng

Volume 2013, Article ID 853594, 6 pages

**A Novel Triple-Mode Bandpass Filter Based on a Dual-Mode Defected Ground Structure Resonator and a Microstrip Resonator**, Xuehui Guan, Ye Yuan, Lan Song, Xiaoyan Wang, Jiuhuai Lei, Lei Zhu, and Peng Cai

Volume 2013, Article ID 852035, 5 pages

**Overview on Multipattern and Multipolarization Antennas for Aerospace and Terrestrial Applications**, Aixin Chen, Weiwei Jiang, Zhizhang Chen, and Jiaheng Wang

Volume 2013, Article ID 102925, 11 pages

## Editorial

# Perforated Ground Plane Structures for RF and Wireless Components

Haiwen Liu,<sup>1</sup> Lei Zhu,<sup>2</sup> Dal Ahn,<sup>3</sup> Amin Abbosh,<sup>4</sup> and Sha Luo<sup>5</sup>

<sup>1</sup> School of Information Engineering, East China Jiaotong University, Nanchang 330013, China

<sup>2</sup> Faculty of Science and Technology, University of Macau, Macau SAR, Macau, China

<sup>3</sup> Department of Electrical Communication Engineering, Soonchunhyang University, Asan, Republic of Korea

<sup>4</sup> School of Information Technology and Electrical Engineering, University of Queensland, Brisbane, QLD, Australia

<sup>5</sup> Department of Electrical and Computer Engineering, National University of Singapore, Singapore

Correspondence should be addressed to Haiwen Liu; liuhaiwen@gmail.com

Received 10 November 2013; Accepted 10 November 2013

Copyright © 2013 Haiwen Liu et al. This is an open access article distributed under the Creative Commons Attribution License, which permits unrestricted use, distribution, and reproduction in any medium, provided the original work is properly cited.

Perforated ground plane (PGP) structures have many interesting properties, such as low-wave effect, suppression of surface waves, high-impedance characteristics, and arbitrary stopbands (passbands). In recent years, PGP structures have attracted great interests in RF and wireless applications (such as passive and active circuits, antennas, waveguides, and packaging). PGP structures are created by assembling a periodic or nonperiodic structure composed of elements in ground plane which are small compared to the wavelength of the propagating electromagnetic wave. As a consequence, PGP structures alter electromagnetic waves propagate in the RF and wireless system.

The objective of this special issue is to provide an in-depth description of the state of the art of research and development in this area. The themes include the new challenges and recent applications in the field of PGP structures for RF and wireless components. Of 17 submissions, 8 papers are accepted for publication in this special issue. Each paper was reviewed by at least two reviewers and revised according to the reviewer's comments. The accepted papers cover the following topics: analysis of the microstrip patches over ground planes with rectangular apertures, couplers with defected ground structure (DGS) microstrip line, DGS resonators, slotted magnetic-LC resonators, bandpass filter (BPF) with slot spurline technique, reconfigurable antenna, and heterostructure high-mobility transistors (HEMTs).

Microstrip patch antennas offer many attractive features such as low profile, light weight, low cost, and ease for integration with printed feeding networks and active circuits.

The microstrip patch antenna can be fed through an aperture cut into a microstrip line ground plane. Several advantages, such as the weak parasitic radiation, tunable impedance and resonant frequency of antennas, have been obtained by using this feeding configuration. However, the algorithms developed for the analysis of these antennas should be able to account for the effect of possible apertures existing in the ground planes of the resonators. In A. Messai et al.'s paper, the authors present a rigorous full-wave analysis of high  $T_c$  superconducting rectangular microstrip patch over ground plane with rectangular aperture in the case where the patch is printed on a uniaxially anisotropic substrate material. The dyadic Green's functions of the considered structure are efficiently determined in the vector Fourier transform domain. The effects of uniaxial anisotropy in the substrate on the resonant frequencies of different TM modes of the superconducting microstrip antenna with rectangular aperture in the ground plane are analyzed. The accuracy of the analysis is tested by comparing the computed results with measurements and previously published data for several anisotropic substrate materials.

Microstrip lines with the defected ground structure (DGS), namely, DGS microstrip line or DGS line, can raise the realizable upper limit of the characteristic impedance of a microstrip line to around  $200\ \Omega$  and can be used in unequal power dividers and couplers. While there has been a serious problem when they are packaged in metallic housing because the bottom ground plane of the microstrip lines, where DGS patterns are realized, makes direct contact with

the metallic package, at this time, the advantageous effects of DGS are removed. In J. Lim et al.'s paper, the authors adopt a double-layered substrate structure to solve the ground contact problem of DGS lines. In the proposed structure, DGS patterns are realized on the ground plane of microstrip lines as in previous cases. However, the second substrate, of which dielectric material is exposed to the top plane, is attached to the ground plane of the first substrate, where the DGS patterns exist. Therefore, it is possible to remove the ground contact problem of DGS, while the advantages of DGS are preserved. At last, they have designed and measured a 10 dB branch line hybrid coupler using DGS line.

Recently, microwave circuits are popularly designed on the ground plane, such as defected ground structure (DGS) resonator, which fully utilize the printed circuit board and therefore reduce the overall circuit size, also with the high power capacity. It provides a novel way to realizing the microwave passive components. In this special issue, there are two papers on the topic of the DGS resonator or its application. In S. J. Lee et al.'s paper, the authors presented a flexible microwave tag system using a frequency-scanning type RFID with multiple DGS resonator. The DGS resonator is spiral shaped and implemented on the rear side of a transmission line, which has the advantages of excellent band notch characteristics as well as bit-error avoidance from the frequency selective reflection. In addition, the tag system is designed on a thin flexible substrate in order to be applicable for amorphous surfaces. In X. Guan et al.'s paper, the authors designed a triple-mode bandpass filter using a dual-mode DGS resonator and a microstrip resonator. The dual-mode characteristic is achieved by loading a defected T-shaped stub to a uniform impedance DGS resonator. A uniform impedance microstrip resonator is designed on the top layer of the DGS resonator and a compact bandpass filter with three resonant modes in the passband can be achieved. The authors have also given the coupling scheme and matrix for the structure.

Split-ring resonators (SRRs), capacitive loaded (C loaded) loops, folded stepped impedance resonators (SIRs), and their complementary counterparts have been extensively used for the implementation of metamaterials and many devices based on them. The magnetic-LC (MLC) resonator can be etched in the ground plane of a single-ended microstrip or a differential microstrip line. In J. Naqui et al.'s paper, the authors presented the MLC-inspired circuits where the MLC units are loaded in both single-ended microstrip and differential microstrip transmission lines. By loading an MLC with the differential microstrip line, for the differential mode, there is an electric wall at the symmetrical plane, and thus the MLC can be driven. Due to the symmetry property, the symmetrical plane of this MLC-loaded single-ended microstrip transmission line becomes a magnetic wall, and the MLC cannot be excited. They also demonstrated that the MLC resonators have many potential applications such as the implementation of balanced notch filters and stopband filters.

Dual-mode microstrip filters are widely used in wireless communications systems, which are based on the coupling of two degenerate modes and split by adding a perturbation element in a geometrically symmetrical resonator. Recently,

resonator with slotline structure has attracted more attention because of its compactness and high power capacity. In H. Liu et al.'s paper, the authors proposed a miniaturized dual-mode bandpass filter using slotline resonator, slot spur lines, and sagittate stubs. The type of the filter characteristic (chebyshev or elliptic) can be controlled by the location of the spur lines. In addition, the filter achieves large reduction in overall size by using the sagittate stubs instead of the traditional ones.

With advantage of multipattern and multipolarization, the reconfigurable antennas are popular and timely to address complex system requirements by modifying their geometry and electrical behavior, which can increase the capabilities of wireless integrated information systems, expand their functionality, or widen their bandwidths, with efficient spectrum and power utilization. In A. Chen et al.'s paper, the authors discussed different patterns and polarizations of reconfigurable antennas according to current research work in this area. The radiation pattern states of antennas include beam direction, shape, and gain, and the polarization states of antennas consist of horizontal/vertical linear,  $\pm$ slant  $45^\circ$  linear, left-hand, or right-band circular polarized. Different multi-pattern and multi-polarization antennas with various structures and working mechanisms are compared and discussed in the paper.

By the great development of the material quality and device processing techniques, AlGaIn/GaN HEMT has been much improved in both DC and RF performances. It will become an ideal candidate for high-power, high-frequency, and high-temperature electronic devices. There are many researches about improving its DC and AC performances by changing material or structure of epitaxial layer of AlGaIn/GaN HEMTs since the performances of monolithic microwave integrated circuits (MMICs) are influenced by the characteristics of active devices. In L. Jin et al.'s paper, the authors presented the impact of layout sizes of  $\text{Al}_{0.27}\text{Ga}_{0.73}\text{N}/\text{AlN}/\text{Al}_{0.04}\text{Ga}_{0.96}\text{N}/\text{GaN}$  HEMTs based on SiC substrate on its characteristics that include the threshold voltage, the maximum transconductance, characteristic frequency, and the maximum oscillation frequency. The changing parameters include the gate finger number and the gate width per finger. It is significant for designing AlGaIn/GaN HEMT with excellent performance.

These papers represent an exciting and insightful observation into the state of the art, as well as emerging research topics, in this important field.

## Acknowledgments

We hope that this special issue would attract a major attention of the peers. We would like to express our appreciation to all the authors and reviewers for great support to make this special issue possible.

*Haiwen Liu  
Lei Zhu  
Dal Ahn  
Amin Abbosh  
Sha Luo*

## Research Article

# Analysis of High $T_c$ Superconducting Rectangular Microstrip Patches over Ground Planes with Rectangular Apertures in Substrates Containing Anisotropic Materials

Abderraouf Messai,<sup>1</sup> Siham Benkouda,<sup>1</sup> Mounir Amir,<sup>2</sup> Sami Bedra,<sup>2</sup> and Tarek Fortaki<sup>2</sup>

<sup>1</sup> Electronics Department, University of Constantine, 25000 Constantine, Algeria

<sup>2</sup> Electronics Department, University of Batna, 05000 Batna, Algeria

Correspondence should be addressed to Tarek Fortaki; [t.fortaki@yahoo.fr](mailto:t.fortaki@yahoo.fr)

Received 30 March 2013; Accepted 22 June 2013

Academic Editor: Haiwen Liu

Copyright © 2013 Abderraouf Messai et al. This is an open access article distributed under the Creative Commons Attribution License, which permits unrestricted use, distribution, and reproduction in any medium, provided the original work is properly cited.

A rigorous full-wave analysis of high  $T_c$  superconducting rectangular microstrip patch over ground plane with rectangular aperture in the case where the patch is printed on a uniaxially anisotropic substrate material is presented. The dyadic Green's functions of the considered structure are efficiently determined in the vector Fourier transform domain. The effect of the superconductivity of the patch is taken into account using the concept of the complex resistive boundary condition. The accuracy of the analysis is tested by comparing the computed results with measurements and previously published data for several anisotropic substrate materials. Numerical results showing variation of the resonant frequency and the quality factor of the superconducting antenna with regard to operating temperature are given. Finally, the effects of uniaxial anisotropy in the substrate on the resonant frequencies of different TM modes of the superconducting microstrip antenna with rectangular aperture in the ground plane are presented.

## 1. Introduction

Microstrip patch resonators offer many attractive features such as low profile, light weight, low cost, and the ease with which they can be integrated with printed feeding networks and active circuits. They can be used either as antennas or as components of oscillators and filters in microwave-integrated circuits. When a microstrip patch resonator acts as an antenna, the microstrip patch can be fed through an aperture cut into a microstrip line ground plane. Several advantages have been obtained by using this feeding configuration [1, 2]. Such advantages include weak parasitic radiation in the useful direction with respect to conventionally fed antennas and optimal performance for both the feeding network and antenna element. In addition, the presence of aperture on the ground plane adds new design parameters that can be used to tune the antenna impedance and resonance frequency, without modifying the patch itself. Since ground-plane apertures can play a role in the design of microstrip patch antennas, the algorithms developed for the analysis

of these antennas should be able to account for the effect of possible apertures existing in the ground planes of the resonators.

Since the discovery of the high  $T_c$  superconducting materials which have critical temperatures above the boiling point of liquid nitrogen, the development of microwave application of high  $T_c$  superconductors has been extremely rapid and numbers of highly sophisticated subsystem level modules have been generated. Superconducting passive microwave devices such as antennas, filters, transmission line, and phase shifters have shown significant superiority over corresponding devices fabricated with normal conductors such as gold, silver, or copper due to the low surface resistance of superconductors. The low surface resistance corresponds to a large quality factor and improved performance such as higher gain and lower insertion loss in passive microwave devices [3–7].

Setting aside the topic of superconducting materials, in the last few years, there has been a growing interest in studying how the performance of microstrip antennas is

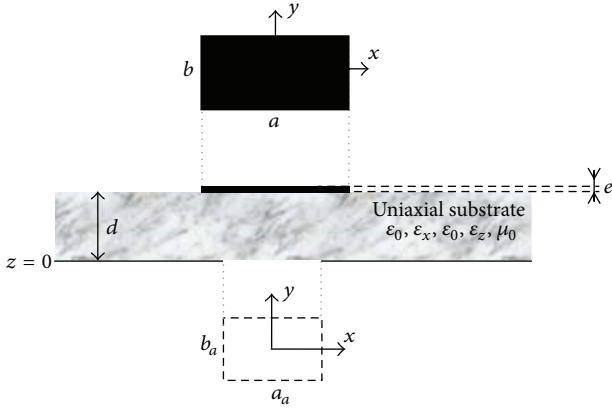


FIGURE 1: Geometrical structure of a high  $T_c$  superconducting rectangular microstrip patch over a ground plane with a rectangular aperture in the case where the superconducting patch is printed on an anisotropic dielectric substrate.

affected when anisotropic dielectrics are used as substrates of those antennas [8–14]. We bear in mind that some dielectric substances used as substrates of microstrip antennas exhibit anisotropy due to their natural crystal structures or as the result of their production processes. Isotropic substances may also exhibit anisotropy at high frequencies. The overall results of the previous studies indicate that operational behavior of such structures may not be as expected especially at higher millimetre wave frequencies when anisotropy of the substrate material is ignored.

This paper presents a rigorous full-wave analysis of high  $T_c$  superconducting rectangular microstrip patch over ground plane with rectangular aperture. The rectangular patch is printed on a uniaxially anisotropic substrate material. As far as the authors know, this subject has not been reported in the open literature; the only published results on the full-wave analysis of superconducting microstrip antennas with apertures in the ground planes refer to isotropic substrates [15]. This paper is organized as follows. In Section 2, the dyadic Green's functions of the considered structure are efficiently determined in the vector Fourier transform domain. The effect of the superconductivity of the patch is taken into account using the concept of the complex resistive boundary condition. Various numerical results are given in Section 3. Finally, concluding remarks are summarised in Section 4.

## 2. Theory

The problem to be solved is illustrated in Figure 1. We have a high  $T_c$  superconducting rectangular microstrip patch of thickness  $e$  over a ground plane with a rectangular aperture. The substrate material is uniaxially anisotropic with the optical axis being normal to the patch. The uniaxial substrate is characterized by the free-space permeability  $\mu_0$  and a permittivity tensor of the form

$$\bar{\boldsymbol{\epsilon}} = \epsilon_0 \begin{bmatrix} \epsilon_x & 0 & 0 \\ 0 & \epsilon_x & 0 \\ 0 & 0 & \epsilon_z \end{bmatrix}, \quad (1)$$

where  $\epsilon_0$  is the free-space permittivity. Equation (1) can be specialized to the isotropic substrate by allowing  $\epsilon_x = \epsilon_z = \epsilon_r$ . All fields and currents are time harmonic with the  $e^{i\omega t}$  time dependence being suppressed. The transverse fields inside the anisotropic region ( $0 < z < d$ ) can be obtained via the inverse vector Fourier transforms as shown in [16]

$$\begin{aligned} \mathbf{E}(\mathbf{r}_s, z) &= \begin{bmatrix} E_x(\mathbf{r}_s, z) \\ E_y(\mathbf{r}_s, z) \end{bmatrix} \\ &= \frac{1}{4\pi^2} \int \int_{-\infty}^{+\infty} \bar{\mathbf{F}}(\mathbf{k}_s, \mathbf{r}_s) \cdot \mathbf{e}(\mathbf{k}_s, z) dk_x dk_y, \\ \mathbf{H}(\mathbf{r}_s, z) &= \begin{bmatrix} H_y(\mathbf{r}_s, z) \\ -H_x(\mathbf{r}_s, z) \end{bmatrix} \\ &= \frac{1}{4\pi^2} \int \int_{-\infty}^{+\infty} \bar{\mathbf{F}}(\mathbf{k}_s, \mathbf{r}_s) \cdot \mathbf{h}(\mathbf{k}_s, z) dk_x dk_y, \end{aligned} \quad (2)$$

where  $\bar{\mathbf{F}}(\mathbf{k}_s, \mathbf{r}_s)$  is the kernel of the vector Fourier transform [16], and

$$\begin{aligned} \mathbf{e}(\mathbf{k}_s, z) &= \begin{bmatrix} e^e(\mathbf{k}_s, z) \\ e^h(\mathbf{k}_s, z) \end{bmatrix} = \begin{bmatrix} \frac{i}{k_s} \frac{\epsilon_z}{\epsilon_x} \frac{\partial \tilde{E}_z(\mathbf{k}_s, z)}{\partial z} \\ \frac{\omega \mu_0}{k_s} \tilde{H}_z(\mathbf{k}_s, z) \end{bmatrix}, \\ \mathbf{h}(\mathbf{k}_s, z) &= \begin{bmatrix} h^e(\mathbf{k}_s, z) \\ h^h(\mathbf{k}_s, z) \end{bmatrix} = \begin{bmatrix} \frac{\omega \epsilon_0 \epsilon_z}{k_s} \tilde{E}_z(\mathbf{k}_s, z) \\ \frac{i}{k_s} \frac{\partial \tilde{H}_z(\mathbf{k}_s, z)}{\partial z} \end{bmatrix}. \end{aligned} \quad (3)$$

The superscripts  $e$  and  $h$  denote the TM and TE waves, respectively, and  $\tilde{E}_z$  is the scalar Fourier transform of  $E_z$ . The general form of  $\tilde{E}_z$  and  $\tilde{H}_z$  is [17]

$$\begin{aligned} \tilde{E}_z(\mathbf{k}_s, z) &= A^e e^{-ik_z^e z} + B^e e^{ik_z^e z}, \\ \tilde{H}_z(\mathbf{k}_s, z) &= A^h e^{-ik_z^h z} + B^h e^{ik_z^h z}, \end{aligned} \quad (4)$$

where  $A^e$ ,  $B^e$ ,  $A^h$ , and  $B^h$  are the field spectral amplitudes and

$$\begin{aligned} k_z^e &= \left( \epsilon_x k_0^2 - \frac{\epsilon_x}{\epsilon_z} k_s^2 \right)^{1/2}, & k_z^h &= \left( \epsilon_x k_0^2 - k_s^2 \right)^{1/2}, \\ k_0^2 &= \omega^2 \epsilon_0 \mu_0. \end{aligned} \quad (5)$$

$k_z^e$  and  $k_z^h$  are, respectively, propagation constants for TM and TE waves in the uniaxially anisotropic substrate [2]. After

substitution of the expressions of  $\vec{E}_z$  and  $\vec{H}_z$  given by (4) into (3), we get [17]

$$\begin{aligned}\mathbf{e}(\mathbf{k}_s, z) &= \begin{bmatrix} e^e(\mathbf{k}_s, z) \\ e^h(\mathbf{k}_s, z) \end{bmatrix} \\ &= e^{-i\bar{\mathbf{k}}_z z} \cdot \mathbf{A}(\mathbf{k}_s) + e^{i\bar{\mathbf{k}}_z z} \cdot \mathbf{B}(\mathbf{k}_s), \\ \mathbf{h}(\mathbf{k}_s, z) &= \begin{bmatrix} h^e(\mathbf{k}_s, z) \\ h^h(\mathbf{k}_s, z) \end{bmatrix} \\ &= \bar{\mathbf{g}}(\mathbf{k}_s) \cdot \left[ e^{-i\bar{\mathbf{k}}_z z} \cdot \mathbf{A}(\mathbf{k}_s) - e^{i\bar{\mathbf{k}}_z z} \cdot \mathbf{B}(\mathbf{k}_s) \right].\end{aligned}\quad (6)$$

In (6),  $\mathbf{A}$ , and  $\mathbf{B}$  are two-component unknown vectors and

$$\bar{\mathbf{k}}_z = \begin{bmatrix} k_z^e & 0 \\ 0 & k_z^h \end{bmatrix}, \quad \bar{\mathbf{g}}(\mathbf{k}_s) = \begin{bmatrix} \frac{\omega \varepsilon_0 \varepsilon_x}{k_z^e} & 0 \\ 0 & \frac{k_z^h}{\omega \mu_0} \end{bmatrix}. \quad (7)$$

Writing (6) in the planes  $z = 0$  and  $z = d$ , and by eliminating the unknowns  $\mathbf{A}$  and  $\mathbf{B}$ , we obtain the matrix form

$$\begin{bmatrix} \mathbf{e}(\mathbf{k}_s, d^-) \\ \mathbf{h}(\mathbf{k}_s, d^-) \end{bmatrix} = \bar{\mathbf{T}} \cdot \begin{bmatrix} \mathbf{e}(\mathbf{k}_s, 0^+) \\ \mathbf{h}(\mathbf{k}_s, 0^+) \end{bmatrix} \quad (8)$$

with

$$\bar{\mathbf{T}} = \begin{bmatrix} \bar{\mathbf{T}}^{11} & \bar{\mathbf{T}}^{12} \\ \bar{\mathbf{T}}^{21} & \bar{\mathbf{T}}^{22} \end{bmatrix} = \begin{bmatrix} \cos(\bar{\mathbf{k}}_z d) & -i\bar{\mathbf{g}}^{-1} \cdot \sin(\bar{\mathbf{k}}_z d) \\ -i\bar{\mathbf{g}} \cdot \sin(\bar{\mathbf{k}}_z d) & \cos(\bar{\mathbf{k}}_z d) \end{bmatrix}, \quad (9)$$

which combines  $\mathbf{e}$  and  $\mathbf{h}$  on both sides of the anisotropic region as input and output quantities. Now that we have the matrix representation of the anisotropic substrate, it is easy to derive the dyadic Green's functions of the problem. Let  $\mathbf{J}_0(x, y)$  be the surface current density on the ground plane with rectangular aperture, and let  $\mathbf{J}(x, y)$  be the surface current density on the superconducting rectangular patch. Also, let  $\mathbf{E}(x, y, 0)$  and  $\mathbf{E}(x, y, d)$  be the values of the transverse electric field at the plane of the aperture and at the plane of the superconducting patch, respectively. Following a mathematical reasoning similar to that shown in [16], we can obtain a relation among  $\mathbf{J}_0(x, y)$ ,  $\mathbf{J}(x, y)$ ,  $\mathbf{E}(x, y, 0)$ , and  $\mathbf{E}(x, y, d)$  in the vector Fourier transform domain given by

$$\mathbf{e}(\mathbf{k}_s, d) = \bar{\mathbf{G}}(\mathbf{k}_s) \cdot \mathbf{j}(\mathbf{k}_s) + \bar{\mathbf{F}}(\mathbf{k}_s) \cdot \mathbf{e}(\mathbf{k}_s, 0), \quad (10)$$

$$\mathbf{j}_0(\mathbf{k}_s) = -\bar{\mathbf{F}}(\mathbf{k}_s) \cdot \mathbf{j}(\mathbf{k}_s) + \bar{\mathbf{Y}}(\mathbf{k}_s) \cdot \mathbf{e}(\mathbf{k}_s, 0), \quad (11)$$

where the  $2 \times 2$  diagonal matrices  $\bar{\mathbf{G}}(\mathbf{k}_s)$ ,  $\bar{\mathbf{F}}(\mathbf{k}_s)$ , and  $\bar{\mathbf{Y}}(\mathbf{k}_s)$  stand for a set of dyadic Green's functions in the vector Fourier transform domain. It is to be noted that  $\bar{\mathbf{G}}(\mathbf{k}_s)$  is related to the patch current and  $\bar{\mathbf{Y}}(\mathbf{k}_s)$  is related to the aperture field. The matrix  $\bar{\mathbf{F}}(\mathbf{k}_s)$  represents the mutual coupling between the patch current and aperture field. Considering the superconducting effect, we need simply to modify (10) by

replacing  $\bar{\mathbf{G}}(\mathbf{k}_s)$  by  $\bar{\mathbf{G}}_s(\mathbf{k}_s) = \bar{\mathbf{G}}(\mathbf{k}_s) - Z_s \cdot \bar{\mathbf{I}}$ , where  $\bar{\mathbf{I}}$  stands for the  $2 \times 2$  unit matrix and  $Z_s$  is the surface impedance of the superconducting patch. When the thickness of the superconducting patch is less than three times the zero-temperature penetration depth ( $\lambda_0$ ),  $Z_s$  can be expressed as follows [7, 15]:

$$Z_s = \frac{1}{e\sigma}, \quad (12)$$

where  $\sigma$  is the complex conductivity of the superconducting film. It is determined by using London's equation and the Gorter-Casimir two-fluid model as [7, 15]

$$\sigma = \sigma_n \left( \frac{T}{T_c} \right)^4 - i \frac{1 - (T/T_c)^4}{\omega \mu_0 \lambda_0^2}, \quad (13)$$

where  $T$  is the temperature,  $T_c$  is the transition temperature,  $\sigma_n$  is the normal state conductivity at  $T = T_c$ , and  $\omega$  is the angular frequency. Now that we have included the effect of the superconductivity of the rectangular patch in the Green's functions formulation, the well-known Galerkin procedure of the moment method can be easily applied to obtain the resonant frequencies and quality factors of the resonant modes of the high  $T_c$  superconducting rectangular microstrip patch shown in Figure 1.

Using the moment method, with weighting modes chosen to be identical to the expansion modes, (10) and (11) are reduced to a system of linear equations which can be written compactly in matrix form as [17]

$$\bar{\mathbf{Z}} \cdot \mathbf{C} = \mathbf{0}, \quad (14)$$

where  $\bar{\mathbf{Z}}$  is the impedance matrix and the elements of the vector  $\mathbf{C}$  are the modes expansion coefficient to be sought [17]. The system of linear equations given in (14) has nontrivial solutions when

$$\det[\bar{\mathbf{Z}}(\omega)] = 0. \quad (15)$$

Equation (15) is an eigenequation for  $\omega$ , from which the resonant frequency and quality factor of the structure of Figure 1 can be obtained. In fact, let  $\omega = 2\pi(f_r + if_i)$  be the complex root of (15). In that case, the quantity  $f_r$  stands for the resonant frequency and the quantity  $Q = f_r/(2f_i)$  stands for the quality factor.

### 3. Numerical Results and Discussion

**3.1. Comparison of Numerical Results.** In this study, the considered mode is the  $\text{TM}_{01}$  mode with the dominant current in the  $y$  direction (higher order TM modes are considered only in Section 3.4). The basis functions considered here for approximating the unknown current on the superconducting rectangular patch are formed by the set of TM modes of a rectangular cavity with magnetic side walls and electric top and bottom walls. Also, the same basis functions are used for approximating the magnetic current density on the aperture in accordance with the concept of complementary electromagnetic structures [1, 2].

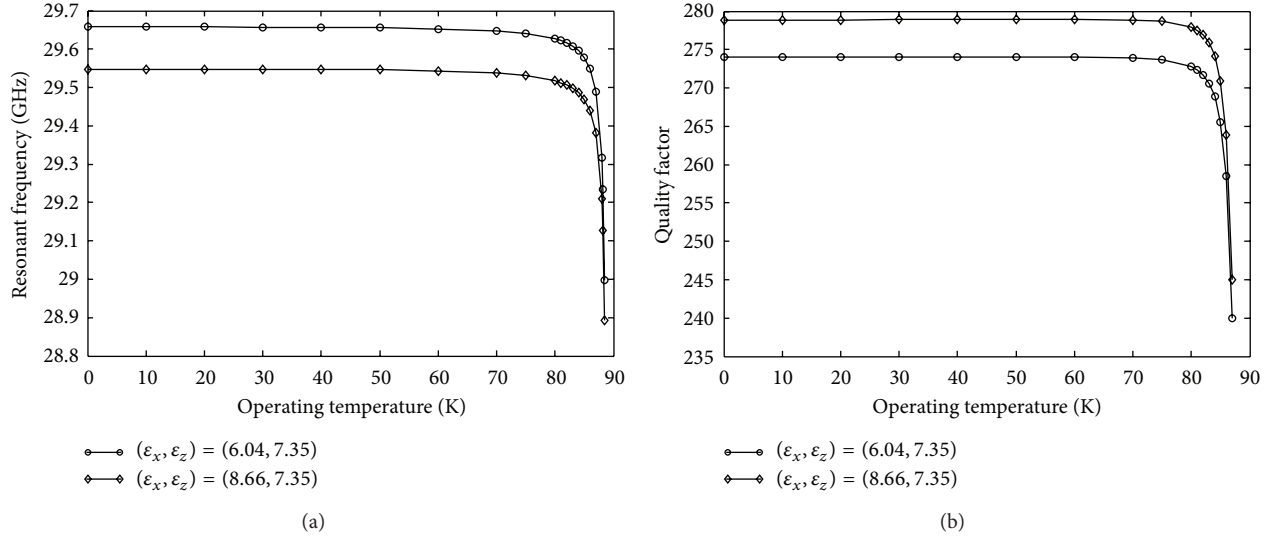


FIGURE 2: Resonant frequency and quality factor of the high  $T_c$  superconducting rectangular microstrip patch over ground plane with rectangular aperture against operating temperature. The superconducting patch is printed on two different anisotropic substrate materials;  $a \times b = 1630 \mu\text{m} \times 1870 \mu\text{m}$ ,  $a_n \times b_n = 53 \mu\text{m} \times 187 \mu\text{m}$ ,  $d = 56.1 \mu\text{m}$ ,  $\sigma_n = 10^6 \text{ S/m}$ ,  $\lambda_0 = 140 \text{ nm}$ ,  $T_c = 89 \text{ K}$ , and  $e = 350 \text{ nm}$ .

To check the correctness of our computer program, our numerical results are compared with those obtained from the magnetic-wall cavity model of Richard et al. [18], when there is no aperture in the ground plane. Numerical evaluations have been done with a patch of dimension  $1.5 \text{ cm} \times 1 \text{ cm}$  printed on anisotropic substrates. The patch is fabricated with a YBCO superconducting thin film with parameters  $\sigma_n = 10^6 \text{ S/m}$ ,  $\lambda_0 = 140 \text{ nm}$ ,  $T_c = 89 \text{ K}$ , and  $e = 350 \text{ nm}$ . The operating temperature is  $T = 60 \text{ K}$ . Table 1 summarizes our computed resonant frequencies and those obtained via the magnetic-wall cavity model [18] for four different non-magnetic anisotropic substrate materials. These anisotropic materials are Sapphire, Epsilam-10, Pyrolytic boron nitride, and PTFE. It is clear from Table 1 that the agreement between our results and those obtained via the magnetic-wall cavity model [18] is very good since the discrepancies between the two sets of results are below 1%. Note that in order to make the magnetic-wall cavity model of Richard et al. [18] able to account for uniaxial anisotropy in the substrate, we have associated with this model the electromagnetic knowledge [13]. The idea is to determine effective parameters for the uniaxially anisotropic substrate using [13, Equations (3) and (4)], and then we use these parameters in the magnetic-wall cavity model of Richard et al. [18].

We have also compared our results with experimental data available in the literature [18]. Table 2 shows the comparison between our calculations and the theoretical and experimental results reported in [18]. It is clear from Table 2 that our results are better than the theoretical values in [18]. The previous comparisons show a very good agreement between our results and those of the literature. This validates the theory proposed in this paper.

**3.2. Influence of the Temperature on the Resonant Frequency and Quality Factor.** Now, we investigate the influence of the

operating temperature on the resonant frequency and quality factor of the superconducting rectangular microstrip antenna with a rectangular aperture in the ground plane. The patch of size  $1630 \mu\text{m} \times 1870 \mu\text{m}$  is made of  $350 \text{ nm}$  thick YBCO thin film with a normal state conductivity at the transition temperature  $\sigma_n = 10^6 \text{ S/m}$ , a zero-temperature penetration depth  $\lambda_0 = 140 \text{ nm}$ , and a transition temperature  $T_c = 89 \text{ K}$ . The rectangular aperture has a size of  $53 \mu\text{m} \times 187 \mu\text{m}$ . The resonant frequency and the quality factor of the superconducting antenna against operating temperature for two different anisotropic substrate materials are shown in Figures 2(a) and 2(b), respectively. The first uniaxially anisotropic material has the pair of relative permittivities  $(\epsilon_x, \epsilon_z) = (6.04, 7.35)$ . The second uniaxially anisotropic material is characterized by an electric anisotropy of negative type [14]  $((\epsilon_x, \epsilon_z) = (8.66, 7.35))$ . Each dielectric substrate has a thickness of  $56.1 \mu\text{m}$ . From the results of Figure 2(a) (Figure 2(b)), it is found that the resonant frequencies (quality factors) obtained when the superconducting patch is printed on the first anisotropic material are higher (lower) than those obtained when the superconducting patch is printed on the second anisotropic material because the effective relative permittivity of the first uniaxial medium is lower than the one of second uniaxial medium. Concerning the influence of the operating temperature on the resonant frequency and quality factor of the superconducting microstrip patch shown in Figure 1, it can be seen that the effect of varying the temperature on the resonant frequency and quality factor is significant only for temperatures near the transition temperature. Note that the steep change in the resonant frequency and quality factor at temperatures near  $T_c$  can be attributed to a change in the magnetic penetration depth of the YBCO [18].

**3.3. Influence of Uniaxial Anisotropy in the Substrate on the Resonant Frequency.** In Table 3, results are presented for the

TABLE 1: Comparison of our calculated resonant frequencies with those obtained via the cavity model [18] combined with electromagnetic knowledge [13] for various anisotropic substrate materials;  $a \times b = 1.5 \text{ cm} \times 1 \text{ cm}$ ,  $a_a = 0$ ,  $d = 0.2 \text{ mm}$ ,  $\sigma_n = 10^6 \text{ S/m}$ ,  $\lambda_0 = 140 \text{ nm}$ ,  $T_c = 89 \text{ K}$ ,  $e = 350 \text{ nm}$ , and  $T = 60 \text{ K}$ .

Anisotropic substrate		Resonant frequency (GHz)		
Dielectric	$(\epsilon_x, \epsilon_z)$	This work	Cavity model [18] combined with electromagnetic knowledge [13]	Error (%)
Sapphire	(9.4, 11.6)	4.371	4.363	0.18
Epsilon-10	(13, 10.3)	4.631	4.620	0.24
Pyrolytic boron nitride	(5.12, 3.4)	7.996	8.034	0.47
PTFE	(2.88, 2.43)	9.428	9.515	0.92

TABLE 2: Comparison of our calculated resonant frequencies with the theoretical and experimental data reported in [18];  $a \times b = 1630 \mu\text{m} \times 935 \mu\text{m}$ ,  $\epsilon_r = 23.81$ ,  $d = 254 \mu\text{m}$ ,  $a_a = 0$ ,  $\sigma_n = 10^6 \text{ S/m}$ ,  $\lambda_0 = 140 \text{ nm}$ ,  $T_c = 89 \text{ K}$ , and  $e = 350 \text{ nm}$ .

Temperature (K)	Resonant frequencies (GHz)		
	Our results	Theoretical data [18]	Experimental data [18]
50	28.764	28.906	28.660
87.4	28.634	28.744	28.380

resonant frequencies of rectangular microstrip patch over ground planes with and without rectangular apertures in the case where the high  $T_c$  superconducting patch is printed on an anisotropic dielectric substrate, that is, Pyrolytic boron nitride, which exhibits a negative uniaxial anisotropy. The patch of size  $1.5 \text{ cm} \times 1 \text{ cm}$  is fabricated with a YBCO superconducting thin film with parameters  $\sigma_n = 10^6 \text{ S/m}$ ,  $\lambda_0 = 140 \text{ nm}$ ,  $T_c = 89 \text{ K}$ , and  $e = 350 \text{ nm}$ . The substrate has a thickness of  $1 \text{ mm}$ . The operating temperature is  $T = 50 \text{ K}$ . In Table 3, the results obtained for the high  $T_c$  superconducting patch printed on anisotropic Pyrolytic boron nitride are compared with the results that would be obtained if the anisotropy of Pyrolytic boron nitride were neglected. In the case where  $a_a \times b_a = a \times b$ , the differences between the results obtained considering anisotropy and neglecting anisotropy are 5.45%. However, in the other considered cases, these differences are much smaller with the maximum change being 2.70% when  $a_a \times b_a = 0.75a \times 0.75b$ . Therefore, dielectric anisotropy effect is especially significant when the size of the aperture is similar to that of the high  $T_c$  superconducting patch. This result agrees with that discovered theoretically for perfectly conducting rectangular microstrip patches over ground planes with rectangular apertures [2].

*3.4. Effect of the Anisotropy on Different Modes of the Superconducting Antenna.* In Table 4, the effect of uniaxial anisotropy in the substrate on the resonant frequencies of superconducting rectangular microstrip patch over ground plane with rectangular aperture is also investigated. In this table, the considered dielectric is Sapphire, which exhibits a positive uniaxial anisotropy. Unlike Section 3.3, both fundamental mode and higher order TM modes are considered. The patch of size  $1.5 \text{ cm} \times 1 \text{ cm}$  is fabricated with a YBCO superconducting thin film with parameters  $\sigma_n = 10^6 \text{ S/m}$ ,  $\lambda_0 = 140 \text{ nm}$ ,  $T_c = 89 \text{ K}$ , and  $e = 350 \text{ nm}$ . The substrate has a thickness of  $2 \text{ mm}$ , and the aperture size is  $2.1 \text{ mm} \times 1.4 \text{ mm}$ . The operating temperature is  $T = 40 \text{ K}$ . For the

modes having the dominant current in the  $x$  direction ( $\text{TM}_{10}$  and  $\text{TM}_{20}$ ), the differences between the results obtained considering anisotropy and neglecting anisotropy are smaller compared to those of the other considered modes. It is also seen from Table 4 that for the mode  $\text{TM}_{02}$ , the difference between the results obtained considering anisotropy and neglecting anisotropy is 2.27%. However, in the other considered modes, these differences are much smaller with the maximum change being 1.72% for the mode  $\text{TM}_{11}$ . Therefore, dielectric anisotropy effect is especially significant for the mode  $\text{TM}_{02}$ .

## 4. Conclusion

We have described an accurate analysis of high  $T_c$  superconducting rectangular microstrip patch over ground plane with rectangular aperture in the case where the superconducting patch is printed on an anisotropic dielectric substrate. The dyadic Green's functions of the considered anisotropic structure have been efficiently determined in the vector Fourier transform domain. The effect of the superconductivity of the patch has been taken into account using the concept of the complex resistive boundary condition. Galerkin's method has been used to solve for the surface current density on the superconducting patch and the transverse electric field at the aperture. The accuracy of the method was checked by performing a set of results in terms of resonant frequencies for various anisotropic substrate materials. In all cases, very good agreements compared with the literature were obtained. Numerical results show that the influence of the operating temperature on the resonant frequency and quality factor of superconducting rectangular microstrip patches over ground planes with rectangular apertures in substrates containing anisotropic materials is especially significant for temperatures near the transition temperature. Other results also have indicated that dielectric anisotropy effect is especially significant when the size of the aperture is similar to that of the

TABLE 3: Resonant frequencies of high  $T_c$  superconducting rectangular microstrip patch printed on anisotropic Pyrolytic boron nitride over ground planes with and without rectangular apertures;  $a \times b = 1.5 \text{ cm} \times 1 \text{ cm}$ ,  $d = 1 \text{ mm}$ ,  $\sigma_n = 10^6 \text{ S/m}$ ,  $\lambda_0 = 140 \text{ nm}$ ,  $T_c = 89 \text{ K}$ ,  $e = 350 \text{ nm}$ , and  $T = 50 \text{ K}$ .

Aperture size $a_a \times b_a$	Resonant frequencies (GHz)		Fractional change (%)
	Considering anisotropy $(\epsilon_x, \epsilon_z) = (5.12, 3.4)$	Neglecting anisotropy $(\epsilon_x, \epsilon_z) = (3.4, 3.4)$	
0	7.399	7.531	1.78
$0.25a \times 0.25b$	7.044	7.165	1.72
$0.5a \times 0.5b$	5.935	6.052	1.97
$0.75a \times 0.75b$	4.955	5.089	2.70
$a \times b$	4.277	4.510	5.45

TABLE 4: Resonant frequencies of different TM modes of high  $T_c$  superconducting rectangular microstrip patch printed on anisotropic Sapphire over ground plane with rectangular aperture;  $a \times b = 1.5 \text{ cm} \times 1 \text{ cm}$ ,  $a_a \times b_a = 2.1 \text{ mm} \times 1.4 \text{ mm}$ ,  $d = 2 \text{ mm}$ ,  $\sigma_n = 10^6 \text{ S/m}$ ,  $\lambda_0 = 140 \text{ nm}$ ,  $T_c = 89 \text{ K}$ ,  $e = 350 \text{ nm}$ , and  $T = 40 \text{ K}$ .

Mode $\text{TM}_{nm}$	Resonant frequencies (GHz)		Fractional change (%)
	Considering anisotropy $(\epsilon_x, \epsilon_z) = (9.4, 11.6)$	Neglecting anisotropy $(\epsilon_x, \epsilon_z) = (11.6, 11.6)$	
$\text{TM}_{10}$	2.946	2.909	1.26
$\text{TM}_{01}$	4.032	3.967	1.61
$\text{TM}_{11}$	5.288	5.197	1.72
$\text{TM}_{20}$	5.643	5.567	1.35
$\text{TM}_{02}$	7.626	7.453	2.27

high  $T_c$  superconducting patch. This result agrees with that discovered theoretically for perfectly conducting rectangular microstrip patches over ground planes with rectangular apertures [2]. Concerning the influence of uniaxial anisotropy in the substrate on different TM modes of the superconducting antenna, we have found that dielectric anisotropy effect is especially significant for the mode  $\text{TM}_{02}$ .

## References

- [1] V. Losada, R. R. Boix, and M. Horno, "Resonant modes of circular microstrip patches over ground planes with circular apertures in multilayered substrates containing anisotropic and ferrite materials," *IEEE Transactions on Microwave Theory and Techniques*, vol. 48, no. 10, pp. 1756–1762, 2000.
- [2] T. Fortaki and A. Benghalia, "Rigorous full-wave analysis of rectangular microstrip patches over ground planes with rectangular apertures in multilayered substrates that contain isotropic and uniaxial anisotropic materials," *Microwave and Optical Technology Letters*, vol. 41, no. 6, pp. 496–500, 2004.
- [3] S. Liu and B. Guan, "Wideband high-temperature superconducting microstrip antenna," *Electronics Letters*, vol. 41, no. 17, pp. 947–948, 2005.
- [4] N. Sekiya, A. Kubota, A. Kondo, S. Hirano, A. Saito, and S. Ohshima, "Broadband superconducting microstrip patch antenna using additional gap-coupled resonators," *Physica C*, vol. 445–448, no. 1–2, pp. 994–997, 2006.
- [5] O. Barkat and A. Benghalia, "Radiation and resonant frequency of superconducting annular ring microstrip antenna on uniaxial anisotropic media," *Journal of Infrared, Millimeter, and Terahertz Waves*, vol. 30, no. 10, pp. 1053–1066, 2009.
- [6] F. Benmeddour, C. Dumond, F. Benabdelaziz, and F. Bouttout, "Improving the performances of a high  $T_c$  superconducting circular microstrip antenna with multilayered configuration and anisotropic dielectrics," *Progress In Electromagnetics Research C*, vol. 18, pp. 169–183, 2011.
- [7] S. Benkouda, M. Amir, T. Fortaki, and A. Benghalia, "Dual-frequency behavior of stacked high  $T_c$  superconducting microstrip patches," *Journal of Infrared, Millimeter, and Terahertz Waves*, vol. 32, no. 11, pp. 1350–1366, 2011.
- [8] T. Fortaki, L. Djouane, F. Chebara, and A. Benghalia, "On the dual-frequency behavior of stacked microstrip patches," *IEEE Antennas and Wireless Propagation Letters*, vol. 7, pp. 310–313, 2008.
- [9] O. Barkat and A. Benghalia, "Synthesis of superconducting circular antennas placed on circular array using a particle swarm optimisation and the fullwave method," *Progress In Electromagnetics Research B*, no. 22, pp. 103–119, 2010.
- [10] Ç. S. Gürel and E. Yazgan, "Resonant frequency analysis of annular ring microstrip patch on uniaxial medium via hankel transform domain immittance approach," *Progress In Electromagnetics Research M*, vol. 11, pp. 37–52, 2010.
- [11] Ç. S. Gürel and E. Yazgan, "Resonance in microstrip ring resonator with uniaxially anisotropic substrate and superstrate layers," *Journal of Electromagnetic Waves and Applications*, vol. 24, no. 8–9, pp. 1135–1144, 2010.
- [12] A. Motevasselian, "Spectral domain analysis of resonant characteristics and radiation patterns of a circular disc and an annular ring microstrip antenna on uniaxial substrate," *Progress In Electromagnetics Research M*, vol. 21, pp. 237–251, 2011.
- [13] Y. Tighilt, F. Bouttout, and A. Khellaf, "Modeling and design of printed antennas using neural networks," *International Journal of RF and Microwave Computer-Aided Engineering*, vol. 21, no. 2, pp. 228–233, 2011.
- [14] L. Djouablia, I. Messaouden, and A. Benghalia, "Uniaxial anisotropic substrate effects on the resonance of an equitriangular MI-crostrip patch antenna," *Progress in Electromagnetics Research M*, vol. 24, pp. 45–56, 2012.

- [15] F. Chebbara, S. Benkouda, and T. Fortaki, "Fourier transform domain analysis of high  $T_c$  superconducting rectangular microstrip patch over ground plane with rectangular aperture," *Journal of Infrared, Millimeter, and Terahertz Waves*, vol. 31, no. 7, pp. 821–832, 2010.
- [16] T. Fortaki, L. Djouane, F. Chebara, and A. Benghalia, "Radiation of a rectangular microstrip patch antenna covered with a dielectric layer," *International Journal of Electronics*, vol. 95, no. 9, pp. 989–998, 2008.
- [17] T. Fortaki, D. Khedrouche, F. Bouttout, and A. Benghalia, "A numerically efficient full-wave analysis of a tunable rectangular microstrip patch," *International Journal of Electronics*, vol. 91, no. 1, pp. 57–70, 2004.
- [18] M. A. Richard, K. B. Bhasin, and P. C. Claspy, "Superconducting microstrip antennas: an experimental comparison of two feeding methods," *IEEE Transactions on Antennas and Propagation*, vol. 41, no. 7, pp. 967–974, 1993.

## Research Article

# A Defected Ground Structure without Ground Contact Problem and Application to Branch Line Couplers

Jongsik Lim,<sup>1</sup> Dal Ahn,<sup>1</sup> Sang-Min Han,<sup>1</sup> Yongchae Jeong,<sup>2</sup> and Haiwen Liu<sup>3</sup>

<sup>1</sup> Soonchunhyang University, Asan, Chungnam 336-745, Republic of Korea

<sup>2</sup> Chonbuk National University, Jeonju, Chonbuk 561-756, Republic of Korea

<sup>3</sup> East China of Jiaotong University, Nanchang 330013, China

Correspondence should be addressed to Jongsik Lim; [jslim@sch.ac.kr](mailto:jslim@sch.ac.kr)

Received 26 March 2013; Revised 11 June 2013; Accepted 23 June 2013

Academic Editor: Sha Luo

Copyright © 2013 Jongsik Lim et al. This is an open access article distributed under the Creative Commons Attribution License, which permits unrestricted use, distribution, and reproduction in any medium, provided the original work is properly cited.

A new defected ground structure (DGS) microstrip line that is free from the ground contact problem is described together with its application example. The proposed DGS microstrip line adopts a double-layered substrate. The first layer contains the microstrip line and DGS patterns on the top and bottom planes as with the conventional DGS line. The second substrate, of which upper metal plane has already been removed, is attached to the bottom ground plane of the first layer. This structure prevents the ground plane of the first substrate with DGS patterns from making contact with the metal housing. The proposed DGS microstrip line has advantageous transmission and rejection characteristics, without the ground contact problem of DGS patterns, which has been a critical problem of previous DGS lines. A 10 dB branch line hybrid coupler is designed and measured, as an example of application of the proposed DGS microstrip line.

## 1. Introduction

Normal microstrip lines theoretically have all pass characteristics. However, it has been extensively known that if perforating patterns, such as photonic bandgap (PBG) and defected ground structure (DGS), are inserted on the ground plane, the transmission characteristics change severely from those of normal transmission lines [1, 2].

The advantages of DGS described in previous studies are the as follows. (1) It is easily performed to extract the equivalent circuit model [3], (2) it is well applied to RF/microwave circuits to reduce sizes or improve performances [4], and (3) DGS raises the realizable upper limit of the characteristic impedance of a microstrip line to around 200  $\Omega$  [5–7]. According to previous works, 150  $\Omega$ , 158  $\Omega$ , and 207  $\Omega$  microstrip lines have been realized due to DGS and used in unequal power dividers and couplers. It should be noted that the realizable limit of characteristic impedance of normal microstrip lines is around 110  $\Omega$  ~ 120  $\Omega$  [8].

However, in the previous microstrip lines with DGS, hereinafter “DGS microstrip line” or “DGS line,” there has been a serious problem when they are packaged in metallic

housing because the bottom ground plane of microstrip lines, where DGS patterns are realized, makes direct contact with the metallic package. Then, it is definite that the advantageous effects of DGS are removed, when the inner bottom of the housing and the lower plane of microstrip lines make contact with each other.

In this work, the DGS line that adopts a double-layered substrate structure is described, in order to solve the ground contact problem of DGS lines. In the proposed structure, DGS patterns are realized on the ground plane of microstrip lines as in previous cases. However, the second substrate, of which dielectric material is exposed to the top plane, is attached to the ground plane of the first substrate, where the DGS patterns exist. Therefore, it is possible to remove the ground contact problem of DGS, while the advantages of DGS are preserved. As an example of application, a 10 dB branch line hybrid coupler is designed and measured.

## 2. DGS Lines Using Double-Layered Substrate

Figure 1 shows the existing DGS microstrip line. Even though it has advantages over normal microstrip lines, it has also

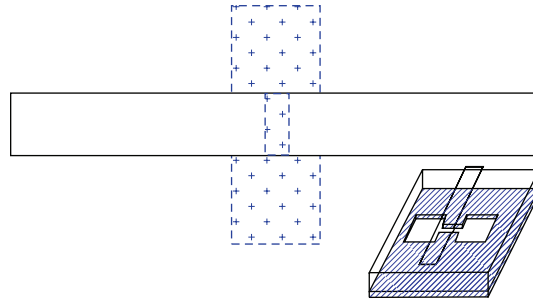


FIGURE 1: Microstrip line having DGS on the ground plane.

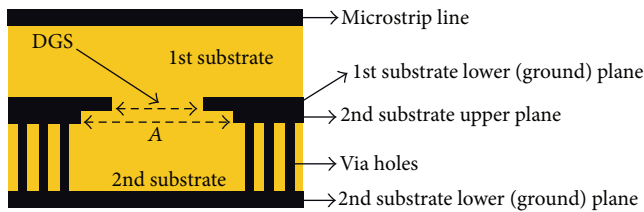


FIGURE 2: DGS line using the double-layered substrate. Area “A” completely contains the DGS patterns.

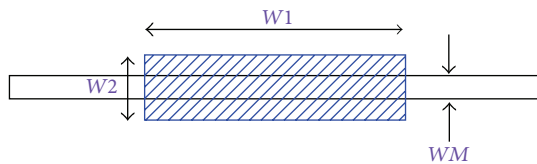


FIGURE 3: Microstrip line having double-layered substrate and rectangular DGS.

the critical problem that it cannot be inserted into a metal housing. If the bottom ground plane is directly faced with a metal box, the main characteristics of DGS immediately disappear because the etched DGS patterns are compensated for by the metallic bottom surface of the housing, so it becomes a new normal microstrip line. Therefore, the DGS plane should be separated from the metallic package for the advantages of DGS to be preserved.

Figure 2 shows the DGS microstrip line with a double-layered substrate in this work. It is easily understood that the structure in Figure 2 prevents the DGS patterns from directly contacting the surface of the metallic housing. In the conventional DGS lines, DGS patterns are realized on the ground plane of the first substrate. However in this work, the second substrate is attached to the first substrate, so that the DGS cannot directly face the metal housing. Basically, the whole upper metal plane of the second substrate might be removed. However; the specific area designated as “A” in Figure 2 may be selectively erased. It is important that area “A” should completely contain the DGS patterns.

It is important that the bottom planes of the first and second substrates should be connected through lots of via holes for the same ground potential. Although it is preferred that the thickness of the second substrate should be as thin as possible, this is not critical because the top and bottom metal planes of the second substrate are connected by a lot of via

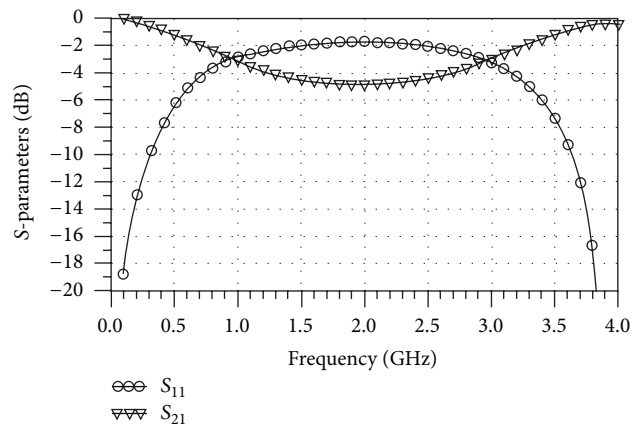


FIGURE 4: Electromagnetically calculated S-parameter of the DGS line shown in Figure 3 ( $W1 = 20$  mm,  $W2 = 5$  mm,  $WM = 0.20$  mm).

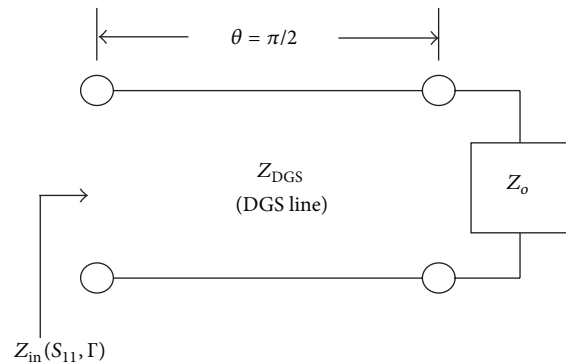


FIGURE 5: Equivalent circuit model to determine the characteristic impedance of the DGS line.

holes for the same ground potential. It is easily understood that the ground plane of the second substrate makes contact with the inner bottom of the metallic housing.

### 3. Characteristic Impedance Analysis

Figure 3 shows the top view of the adopted DGS line in this work, which consists of a microstrip line and rectangular-shaped DGS on the bottom ground plane of the first substrate. The second substrate is not shown here, even though it is attached to the first substrate. “W1” and “W2” are

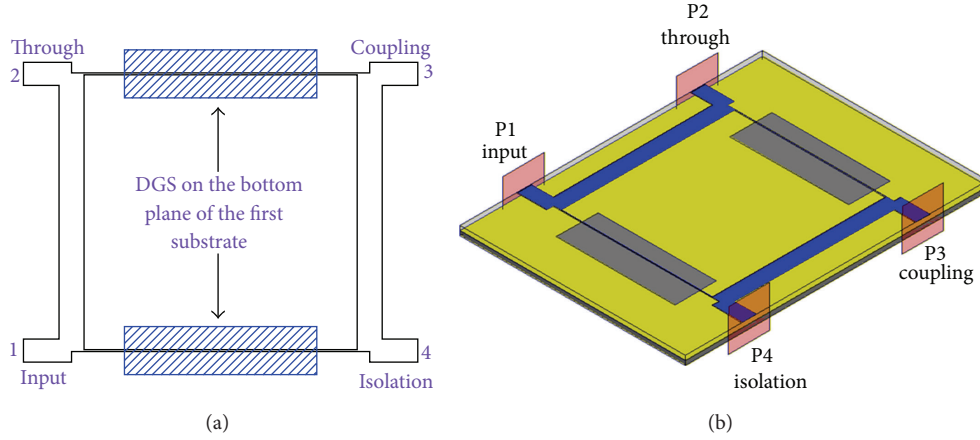


FIGURE 6: Layout of the proposed 10 dB hybrid coupler using DGS and double-layered substrate: (a) 2-dimensional view and (b) 3-dimensional view.

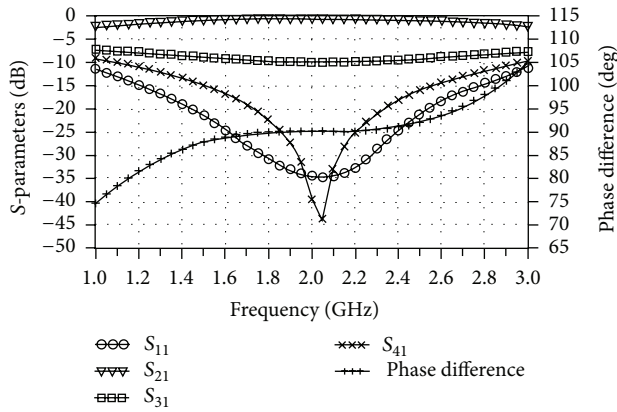


FIGURE 7: Simulated performances of the 10 dB branch line hybrid coupler.

the dimensions of the rectangular DGS, and “ $WM$ ” is the width of the microstrip line on the top plane of the first substrate. The dielectric constant ( $\epsilon_r$ ) and thickness of the first substrate in this work are 2.2 and 31 mils, respectively. The same substrate has been selected as the second substrate, for convenience.

When the rectangular-shaped DGS is realized on the ground plane of the first substrate, the effectively added inductance highly increases, as has already been discussed in many previous works, while the added effective capacitance is relatively small. As the result, a microstrip line is obtained with higher characteristic impedance than the normal one for the same line width.

Figure 4 illustrates the electromagnetically simulated  $S$ -parameter of the DGS line shown in Figure 3. The  $S_{11}$  is around  $-1.9$  dB, which corresponds to  $150 \Omega$  line impedance.

Figure 5 and (1)–(3) are useful for calculating the characteristic impedance of the DGS line. Figure 5 shows the transmission line model of the DGS line to determine the characteristic impedance ( $Z_{DGS}$ ). When  $\theta = \pi/2$  at the center frequency, the magnitude of the reflection coefficient ( $|\Gamma|$ ) is maximum, so it can be calculated from  $S_{11}$  by (1). Once  $|\Gamma|$

is known,  $Z_{in}$  is calculated by (2). Finally,  $Z_{DGS}$  is calculated from (3):

$$S_{11} [\text{dB}] = 20 \log |\Gamma|, \quad (1)$$

$$Z_{in} = Z_0 \frac{1 + |\Gamma|}{1 - |\Gamma|}, \quad (2)$$

$$Z_{DGS} = \sqrt{Z_{in} Z_0} = Z_0 \sqrt{\frac{1 + |\Gamma|}{1 - |\Gamma|}}. \quad (3)$$

#### 4. Application to Branch Line Hybrid Couplers

A 10 dB branch line hybrid coupler having a conventional 1-layered DGS has already been proposed in [7]. Quarter-wave microstrip lines with  $150 \Omega$  and  $47.4 \Omega$  of characteristic impedances should be provided to design 10 dB hybrid couplers. It is very difficult to realize  $150 \Omega$  of microstrip line using a reasonable aspect ratio of the conventional microstrip line. Furthermore, a serious ground problem exists in the previous  $150 \Omega$  DGS line.

Figure 6 shows the 2- and 3-dimensional views of the designed 10 dB hybrid coupler using the proposed DGS line structure. The rectangular DGS shown in Figure 3 is used for the  $150 \Omega$  line.

Figure 7 illustrates the simulated  $S$ -parameters of the 10 dB hybrid coupler. Electromagnetic (EM) simulations have been performed on Ansoft HFSS and Agilent ADS Momentum, and these two simulators produced the similar results. The predicted  $S_{21}$  and  $S_{31}$  at the center frequency are  $-0.6$  dB and  $-10.3$  dB, respectively.

Figure 8 shows circuit layouts of the fabricated 10 dB hybrid coupler. DGS patterns are directly contacted with the broadly exposed area (“ $A$ ”) of the second substrate. In Figure 8(b), the other metal area remains, except “ $A$ ” in the upper plane of the second substrate, as has been illustrated in Figure 2. The dimensions of the rectangular-shaped DGS and exposed area “ $A$ ” are “ $20 \text{ mm} \times 5 \text{ mm}$ ” and “ $26 \text{ mm} \times 10 \text{ mm}$ ,” respectively.

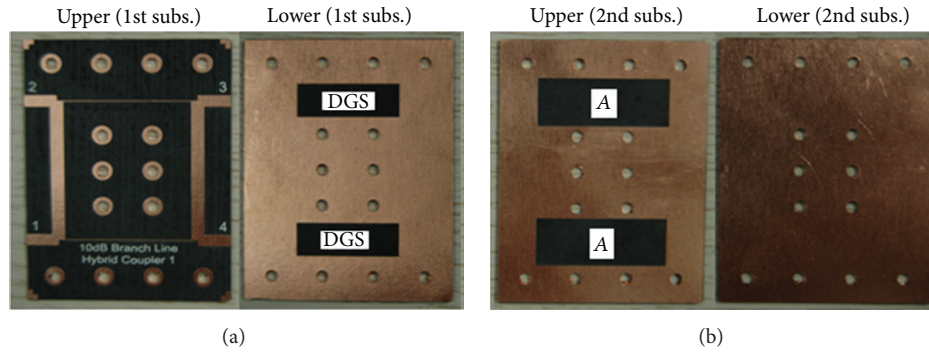


FIGURE 8: Photographs of the fabricated substrates of 10 dB hybrid coupler (a) first substrate and (b) second substrate.

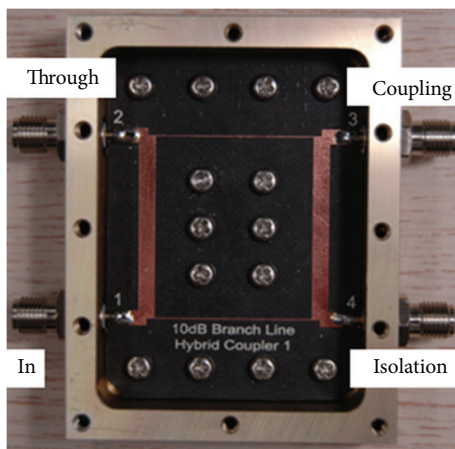


FIGURE 9: Fabricated 10 dB hybrid coupler inserted into a metal housing.

discrepancies are observed, the measured performances show an excellent agreement with the predicted ones in matching, inserting loss, and isolation characteristics. The measured  $S_{21}$  and  $S_{31}$  at center frequency are  $-0.45$  dB and  $-11.5$  dB, respectively, which well prove the performances of the 10 dB coupler.

### 5. Conclusions

In this work, a DGS line adopting a double-layered substrate has been described that has no ground contact problem in metallic packages. The DGS patterns have been separated from the metallic housing, by adding a second substrate to the conventional 1-layered DGS plane. As an application example, a  $150 \Omega$  DGS line has been designed and applied to a 10 dB branch line hybrid coupler. The measured performances were in excellent agreement with the predicted ones.

It has been shown that the proposed DGS line with double-layered substrate solved the ground contact problem of the conventional DGS line, while the advantages of DGS are preserved. Unlike the previous works, the realized 10 dB hybrid coupler in this work has been inserted into a metallic package and successfully measured. It is expected that the proposed method can be applied to other RF/microwave circuits that have perforated ground patterns, such as DGS and PBG.

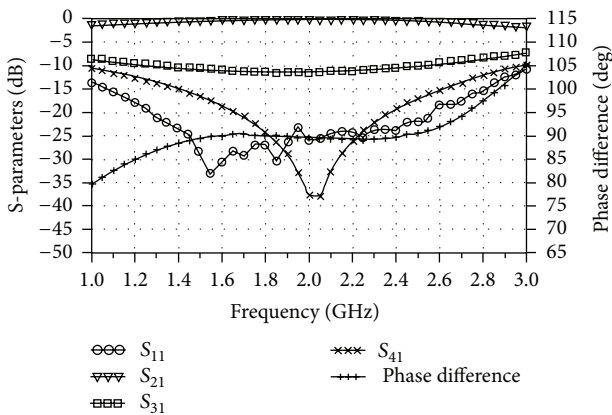


FIGURE 10: Measured S-parameters of the fabricated 10 dB branch line hybrid coupler.

Figure 9 shows the fabricated 10 dB hybrid coupler inserted in a metallic housing. In packaging the 10 dB coupler into the housing, no ground contact problem of DGS occurs, unlike the conventional DGS cases with single layer.

Figure 10 shows the measured S-parameters of the fabricated 10 dB hybrid coupler. Even though some minor

### References

- [1] V. Radisic, Y. Qian, R. Coccioli, and T. Itoh, "Novel 2-D photonic bandgap structure for microstrip lines," *IEEE Microwave and Guided Wave Letters*, vol. 8, no. 2, pp. 69–71, 1998.
- [2] C.-S. Kim, J.-S. Park, D. Ahn, and J.-B. Lim, "A novel 1-D periodic defected ground structure for planar circuits," *IEEE Microwave and Wireless Components Letters*, vol. 10, no. 4, pp. 131–133, 2000.
- [3] D. Ahn, J.-S. Park, C.-S. Kim, J. Kim, Y. Qian, and T. Itoh, "A design of the low-pass filter using the novel microstrip defected ground structure," *IEEE Transactions on Microwave Theory and Techniques*, vol. 49, no. 1, pp. 86–93, 2001.
- [4] J.-S. Lim, J.-S. Park, Y.-T. Lee, D. Ahn, and S. Nam, "Application of defected ground structure in reducing the size of amplifiers," *IEEE Microwave and Wireless Components Letters*, vol. 12, no. 7, pp. 261–263, 2002.

- [5] J.-S. Lim, S.-W. Lee, C.-S. Kim, J.-S. Park, D. Ahn, and S. Nam, "A 4:1 unequal Wilkinson power divider," *IEEE Microwave and Wireless Components Letters*, vol. 11, no. 3, pp. 124–126, 2001.
- [6] J.-S. Lim, G.-Y. Lee, Y.-C. Jeong, D. Ahn, and K.-S. Choi, "A 1:6 unequal wilkinson power divider," in *Proceedings of the 36th European Microwave Conference (EuMC '06)*, pp. 200–203, September 2006.
- [7] J.-S. Lim, C.-S. Kim, J.-S. Park, D. Ahn, and S. Nam, "Design of 10 dB 90° branch line coupler using microstrip line with defected ground structure," *Electronics Letters*, vol. 36, no. 21, pp. 1784–1785, 2000.
- [8] K. C. Gupta, *Microstrip Lines and Slotlines*, Artech House, Norwood, Mass, USA, 1996.

## Research Article

# Flexible Microwave Tag System Based on DGS Multiple Resonators

Seok-Jae Lee,<sup>1</sup> Jongsik Lim,<sup>2</sup> Dal Ahn,<sup>2</sup> and Sang-Min Han<sup>1</sup>

<sup>1</sup> Department of Information and Communication Engineering, Soonchunhyang University, Asan, Chungnam 336-745, Republic of Korea

<sup>2</sup> Department of Electrical Engineering, Soonchunhyang University, Asan, Chungnam 336-745, Republic of Korea

Correspondence should be addressed to Sang-Min Han; [auspice@ieee.org](mailto:auspice@ieee.org)

Received 2 April 2013; Accepted 13 May 2013

Academic Editor: Haiwen Liu

Copyright © 2013 Seok-Jae Lee et al. This is an open access article distributed under the Creative Commons Attribution License, which permits unrestricted use, distribution, and reproduction in any medium, provided the original work is properly cited.

A new flexible microwave tag system using a frequency-scanning type RFID is proposed with multiple resonators based on defected ground structures (DGSs). The proposed system achieves fully passive tag systems using multiple resonators with a spiral-shaped DGS over a wide frequency range. The resonator implemented on the rear side of a transmission line has the advantages of excellent band notch characteristics as well as bit-error avoidance from the frequency selective reflection. In addition, the tag system is designed on a thin flexible substrate in order to be applicable for amorphous surfaces. The proposed microwave tags have been implemented with wideband antennas at 3–7 GHz on thick and thin flexible substrates. The flexibility of the thin substrate has been evaluated in terms of cognitive capability for various radiuses of curvatures. From the experimental results in an anechoic chamber, the excellent recognition of various multibits identification codes in a wireless transmission environment has been verified.

## 1. Introduction

Since the sensor network was issued with various short-range wireless connectivity technologies, interest has been shown in diverse applications for the recognition of identifications (IDs) that can replace bar code systems. Conventional ID systems have developed from a contact type RFID at 13.56 MHz to a contactless type at a UHF band to increase code capacity. Because the recent RFID is used in various ways in collaboration with mobile communication networks, it needs to be of low cost, low power, and large data capacity. The near field communication (NFC) and the chipless RFID become the promising technology candidates for next generation ID systems [1–3].

As the chipless RFID technology has pursued the fully passive tag without semiconductor chips, the ID code should be represented by another feature such as a signal response [4, 5], phase/delay difference [6, 7], or spectral signature [6, 8–10], that is, realized through electromagnetic resonances. However, the conventional chipless RFID has been

implemented on a hard plate to maintain the shape of the electromagnetic resonator. Moreover, the resonant circuits shown on the same surface as the receiving and transmitting antennas make a direct reflection of an interrogating signal, which affects the spectral characteristics of the decoded signals. The flexible fabrication of the microwave resonators on the flexible PCBs [11] and textiles [12] has been issued for patch antennas as part of the system components. However, because the tag system should be fully integrated with all circuit components, it is required to be designed on a flexible media which is able to attach to amorphous shaped items.

In this paper, a fully integrated tag system is designed for all passive components on a planar flexible thin substrate. The system can be fabricated using a one-step printing technology to achieve an inexpensive tag price, while the bendable circuit on the flexible substrate can make it feasible for more various applications of the identifications. Moreover, the architecture of the tag is considered for isolated resonance and high resolution. The multiple resonator circuit with a defected ground structure (DGS) is designed with a spiral shape for

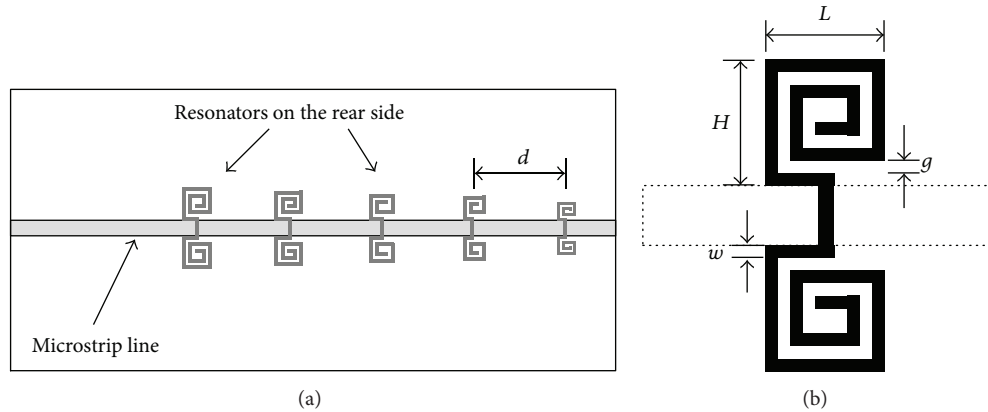


FIGURE 1: Layout of the multiple resonator circuit using defected ground structures. (a) Multiple resonator circuits. (b) Spiral-shaped DGS resonator.

band notch characteristics of a high Q-factor [13, 14]. In addition, thanks to the etched ground structures on the back sides of PCBs, the architecture can avoid direct reflection phenomena. Therefore, the microwave interrogating system can reduce the effect of interferences and achieve a long cognitive distance compared with conventional RFIDs.

This paper is organized as follows. Section 2 introduces the design of the flexible microwave tag systems on thick and thin substrates. The system implementation is described in Section 3. Section 4 shows the experimental results of the system performance evaluations. Finally, the commercial feasibility of the proposed system is mentioned in Section 5.

## 2. Design of a Flexible Tag with Multiple DGSs

In frequency scanning type chipless tag systems, an interrogator exposes frequency-swept microwave signals with constant amplitude and linear phase onto the tag surfaces. The received frequency components experience the series multiple resonant characteristics of the amplitude depth and phase nonlinearity at the assigned resonant frequencies. These variations can be recognized from a retransmitted wideband signal at a reader system. In order to detect the resonant bits clearly, the reader needs to receive the only resonant characteristics from the tag. As the multi-resonator-based chipless tag has several resonators located on the same surface with a receiving antenna [6, 8, 9], the wideband RF is reflected by the resonant circuits that operate as a frequency selective surface (FSS), producing a noisy interferer that prevents fine decoding at a reader. Therefore, these types of tag systems should be designed with consideration of electromagnetic reflections.

In this section, multiple resonator circuits with DGSs and planar wideband antennas are designed for the microwave tag systems. Figure 1(a) presents the layout of the proposed multiple resonator circuit. The resonator is designed with a DGS on the rear side of a substrate, while a transmission line is solely implemented on the front side on which the wideband antenna is mounted. The separation distances

between each resonator are assigned for the isolation and resolution, which are determined as  $d = 12$  mm and 15 mm for thick and thin substrates, respectively. The DGSs are designed as a spiral shape for the band notch characteristic with excellent Q-factor and can be directly mounted on the rear side of a microstrip line. The notch represents a digital bit of “ONE,” whereas the code “ZERO” is recognized by the frequency component without the notch. Therefore, the code can be designed with the presence of resonators.

The multiple resonators are designed on two types of substrates: a thick substrate for design feasibility and a thin substrate for fabrication flexibility at 3–7 GHz. Figure 1(b) shows the spiral DGS layout. By considering the circuit size and notch performance, the DGSs are designed as dual spirals with a maximum of two windings. Each arm has a symmetric square of height  $H$  and length  $L$ . The line width  $w$  and the gap size  $g$  are adjusted to control resonant frequencies and Q-factors and are determined up to the fabrication limit to achieve a Q-factor that is as high as possible.

For the implementation on the thick substrate, five types of spiral-shaped DGSs have been designed for 5 bits with more than 10 dB resolution at each center frequency ( $f_o$ ) of 3 GHz, 3.45 GHz, 4.25 GHz, 5.2 GHz, and 6.2 GHz, respectively. The thick substrate employs FR4 with a thickness of 1 mm and a dielectric constant of 4.4. The design performances have been investigated using a commercial software, the high frequency structure simulator (HFSS) of the ANSYS Inc. Figure 2 presents the design results of the multiple DGS resonators with code “11111.” Each DGS operates to a well-matched performance with  $-30$  dB to  $-40$  dB resonant characteristics and more than 10 dB resolution.

Flexible multiple resonators are designed on a thin substrate of the RT/Duroid 5880 with a thickness of 5 miles and a dielectric constant of 2.2. Four bits’ codes are realized with resonant frequencies of 2.95 GHz, 3.45 GHz, 4.2 GHz, and 5.55 GHz, respectively. Three types of codes are investigated using the same method as that used on the thick substrate. The design results are compared for various codes, as shown in Figure 3. Each bit is evaluated to be clearly recognized

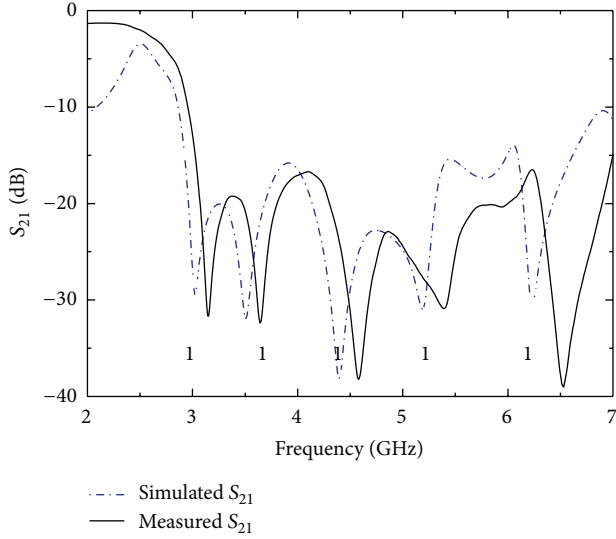


FIGURE 2: Simulated and measured results of multiple resonators on the thick substrate.

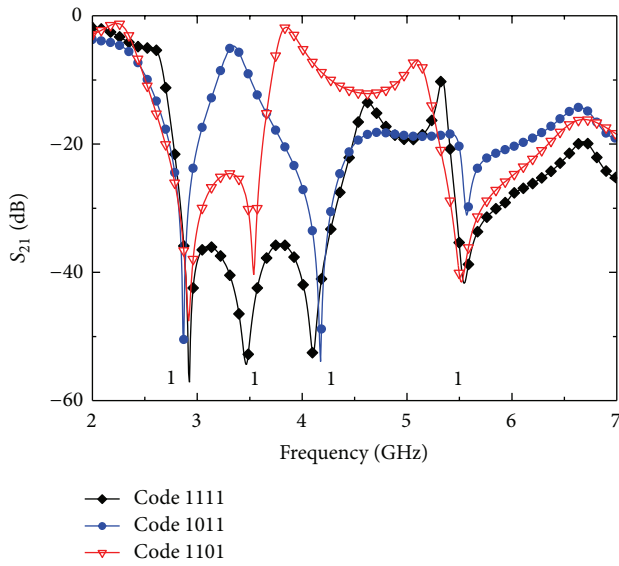


FIGURE 3: Simulated results for frequency resonant bits on the flexible substrate.

by differentiating amplitudes. Table 1 summarizes the design parameters of the multiple resonators on thick and thin substrates.

The tag antenna is designed at an ultrawideband of 2–8 GHz to cover the all resonant frequencies of total resonant bits at 3–7 GHz. It is designed as a planar monopole type to be integrated on the same substrate as the multiple resonator circuit [15–17]. Figure 4 presents the layout of the tag antenna. The planar antenna consists of a radiation patch and a feedline on a substrate with an etched ground plane. The feedline  $W_f \times L_f$  is implemented on a microstrip line with and without a ground plane. The resonant frequency is determined by

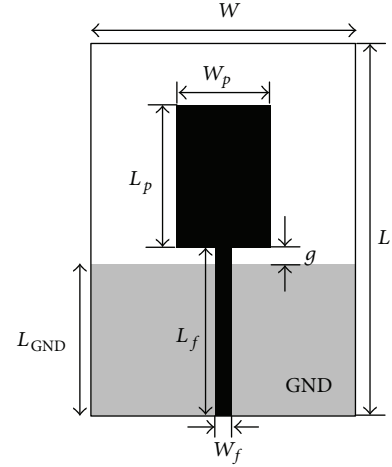


FIGURE 4: Wideband monopole antenna layout.

TABLE 1: Design parameters of the multiple resonators (dimension: mm).

	$f_o$ (GHz)	$H$	$L$	$w$	$g$
Thick substrate	3.0	4.0	3.8	0.4	0.4
	3.45	3.6	3.6	0.4	0.4
	4.25	3.2	3.2	0.4	0.4
	5.2	3.0	2.8	0.4	0.4
	6.2	2.2	2.4	0.3	0.3
Thin substrate	2.95	4.2	4.2	0.3	0.3
	3.45	4.4	4.4	0.4	0.4
	4.2	4.0	4.0	0.4	0.4
	5.55	3.0	3.0	0.3	0.3

TABLE 2: Design parameters of the wideband antennas.

	$W$	$L$	$W_p$	$L_p$	$g$	$W_f$	$L_f$	$L_{GND}$
Thick	31.2	44.2	14.0	17.0	2.0	1.9	20.2	18.2
Thin	33.5	46.7	12.3	16.5	1.0	0.4	20.2	19.2

the monopole patch design  $W_p \times L_p$ . The ground size  $W \times L_{GND}$  and the gap  $g$  between the antenna and the ground are considered as the design parameters for a wide bandwidth. The boundary of the ground plane becomes an important matching parameter as well as a ground reflector. Table 2 presents the design results for both substrates.

As shown in Figure 5, the design and experimental results cover the frequency band of tag systems. The wideband antenna on a thick substrate presents the bandwidth of 2.6 GHz to 8.0 GHz, while that on a thin substrate shows 2.7 GHz to 8.2 GHz. The specification of the antenna is satisfied with both the Tx. and Rx. tag antennas.

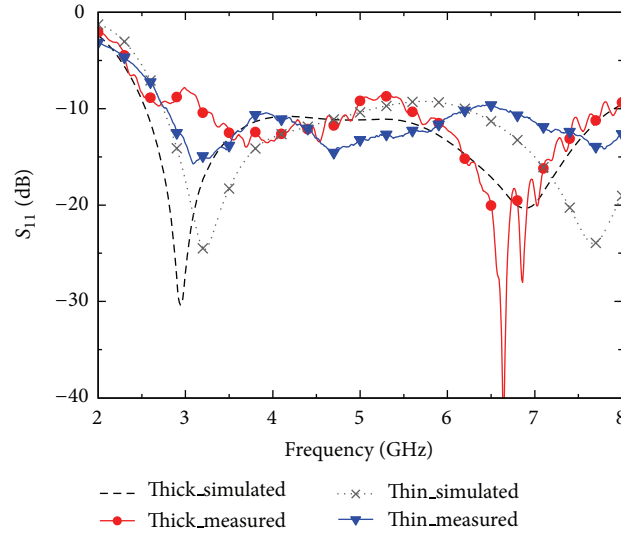


FIGURE 5: Simulated and measured return losses of the UWB antenna.

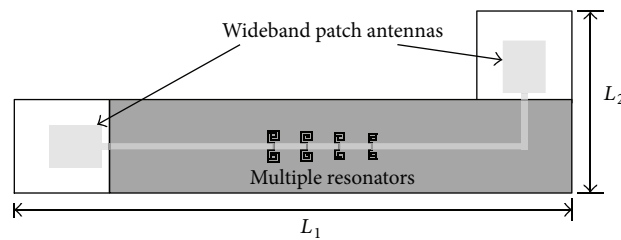


FIGURE 6: Layout of the microwave tag system (on the thin substrate).

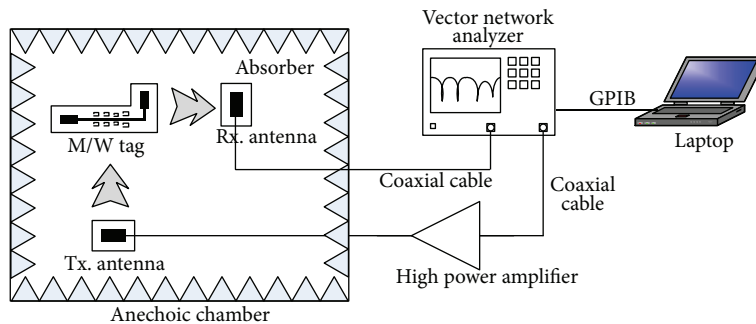


FIGURE 7: Interrogating system set up for wireless transmission tests.

### 3. Implementation of the Microwave Tag System

The proposed flexible microwave tag system with DGSS has been implemented on thick FR4 and thin flexible Teflon substrates. The tags with various 4- or 5-bit codes are evaluated for the recognition of the ID characteristics. The resonator circuits and UWB antennas are integrated on a single PCB. Thanks to the full passive architecture, the proposed tag system can be implemented using a one-step printing fabrication process.

The layout of the implemented tag system is presented in Figure 6. In order to take the polarization diversity that can prevent jamming signals and cross talks, the transmitting and receiving antennas are mounted with an orthogonal orientation to each other. The full tag dimensions are  $L_1 \times L_2 = 188.85 \times 72.75 \text{ mm}^2$  for the thick substrate and  $L_1 \times L_2 = 135.85 \times 63.25 \text{ mm}^2$  for the thin substrate.

Figure 7 shows the interrogating system set up for wireless transmission tests. The performances of the wireless microwave tags have been evaluated in an anechoic chamber

surrounded by electromagnetic absorbers to eliminate multipath effects. The microwave tag and Tx./Rx. reader antennas are fixed on stands fabricated from acrylic and styrofoam material. The Tx./Rx. reader antennas are connected to a Vector Network Analyzer (VNA; E5071C, Agilent Technologies Ltd.) by coaxial cables. For the purpose of providing sufficient transmitting power, a High Power Amplifier (HPA; ZVE-3W-83+, Mini-Circuits Ltd.) is inserted between the Tx. reader antenna and the VNA port. The HPA presents a high gain of 40 dB and a large dynamic range of  $P_{\text{1dB}} = 33$  dBm over 2–8 GHz. The received RF signal at the Rx. antenna passes the multiple resonator circuit and reradiates via the Tx. antenna. The transmitted signal contains bit information of frequency resonance such as amplitude variations and phase nonlinearities, which are compared at the reader system. The detected information has been decoded and analyzed using a laptop computer connected to the VNA.

#### 4. Performance Evaluation of the Proposed Flexible Tag System

In this section, the performance of the proposed tag system is evaluated from two experimental phases. While one experimental phase involves cognitive capability tests that correspond to the bent rate of the flexible thin tag, the other experimental phase is the ID code recognition test on a wireless transmission environment. Each ID code has been presented by measuring the relative insertion losses. The aggregator system organized by the VNA was calibrated to enhance the bit resolution. The calibration was performed by measuring a reference tag that has the same size and substrate as those of the device under test (DUT) tag without any resonators. Because the reference tag represents the code of “00000,” the codes of DUT can be more clearly detected by comparing the measured results between the DUT and the reference tag. The resonant ID codes have been recognized by computing the calibrated datum. In this measurement, the detection criteria are referred to the resolution of the 10 dB amplitude difference.

Flexibility tests have been conducted in order to consider the practical environments for which the flexible tag is applied. Because the tag should be operated in the state of wrinkled and bent shapes, performance variation can be created in a resonant frequency and radiation, and so forth. In this measurement, the proposed flexible tags were bent on a styrofoam jig with a specified radius of curvature,  $r$ , as shown in Figure 8. The flexible tags bent with various radiuses of curvature were measured in an anechoic chamber surrounded by electromagnetic absorbers.

Table 3 presents the measured relative insertion losses at the expected resonant frequencies from most significant bit (MSB) to least significant bit (LSB). The tag under the test is designed using the code “1101.” Four conditions have been tested: an ideal flat surface and radiuses of curvature of 12 mm, 10 mm, and 8 mm, respectively. The ideal flat is considered for the reference values which present more than a 30 dB difference. As the radius of curvature decreases,

TABLE 3: Bit resolution for radiuses of curvature of flexible tags (code 1101).

$r$	1 (MSB)	1	0	1 (LSB)
Ideal	-47.62	-40.41	-7.73	-41.51
12	-29.28	-15.40	-0.05	-13.60
10	-18.70	-22.99	-1.96	-11.01
8	-22.92	-4.36	-1.14	-10.15

the resolution becomes degraded. In the case of  $r = 8$  mm, the amplitude difference of code “1” and “0” is reduced to less than 10 dB. Therefore, the flexible tag has a bending limitation to resolve the resonant frequencies and radiation characteristics in order to mount the applications on amorphous materials.

Figure 9 presents the experimental results of the proposed microwave tags using DGSs on the thick and thin flexible substrates. In Figures 9(a) and 9(b), the code detections of the microwave tags on thick substrates are presented for “10101” and “11001,” respectively. In Figures 9(c) and 9(d), the bit representations at the reader are shown for the tag systems with codes of “1101” and “1011” on thin substrates, respectively. The experimental results have presented good agreement with the S21 values of the resonator circuit without antennas. Even though some frequency shifts at the bit position are found, these are determined to be detectable for code recognitions. In addition, each bit represented by a band notch is well recognized for wireless transmission tests. Figure 10 shows photographs of the proposed microwave tags fabricated on the thick FR4 and thin flexible Teflon substrates.

#### 5. Conclusions

In this paper, the multiple resonator-based microwave tag system with DGSs has been proposed in flexible fabrication technology. The proposed architecture can avoid the direct reflection from a reader antenna and present an excellent resolution to realize the resonant bits. The resonant circuits have been implemented on the thick and thin flexible substrates. The cognitive capabilities have been experimented for various curvatures of flexible tags and wireless transmission performances. From the measured results, wireless transmission performances have presented good agreement with the ideal resonant bit characteristics. Additionally, the design limitation has been presented for a radius of curvature of flexible tags. Therefore, compared with a conventional UHF RFID system, the proposed microwave tag system can be an excellent candidate for a contactless ID tag system with low-cost and mass-productive merits. It can overcome the limitation of conventional RFIDs by fabricating a one-step process and mounting on amorphous items.

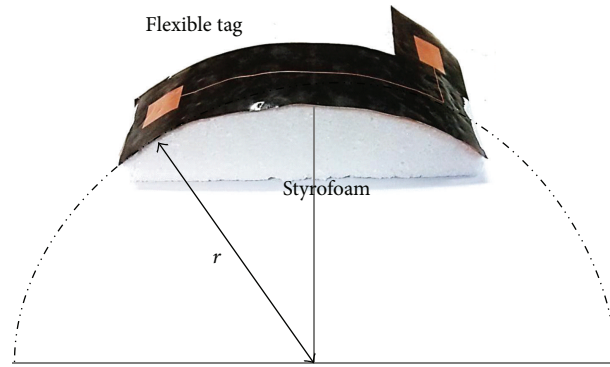
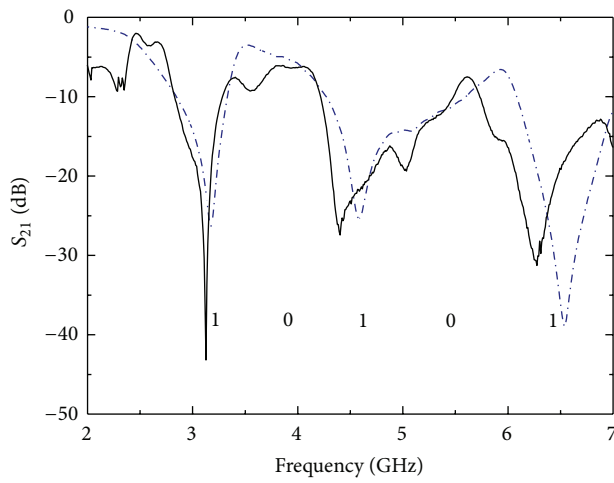
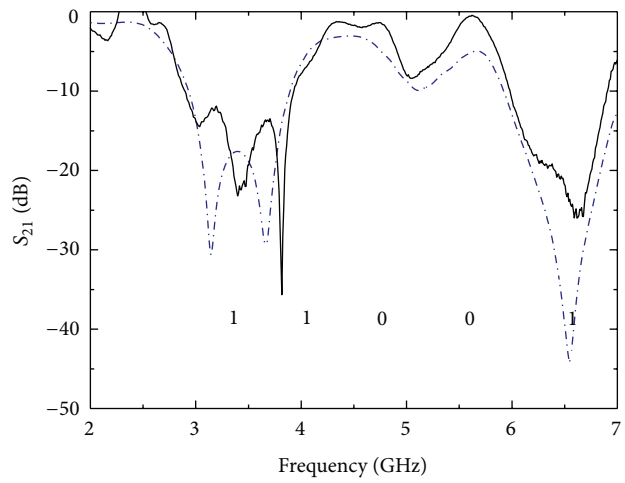


FIGURE 8: Photograph of the bent flexible tag mounted on a bending jig.



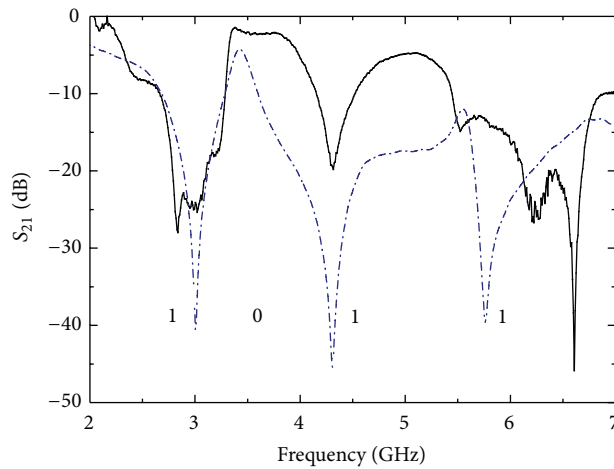
--- Resonator  $S_{21}$ -10101  
 — Wireless tag-10101

(a) Code 10101 on a thick substrate



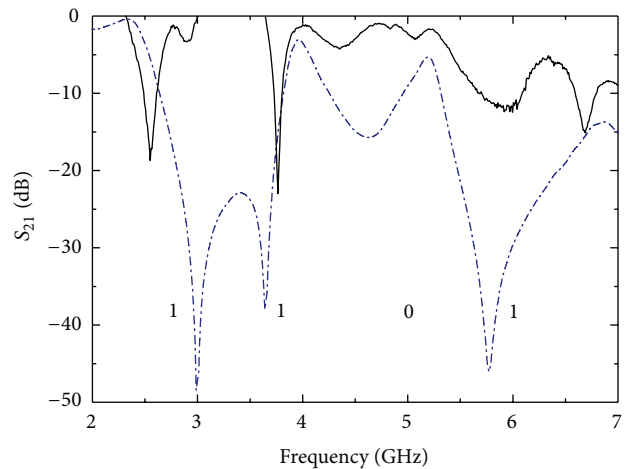
--- Resonator  $S_{21}$ -11001  
 — Wireless tag-11001

(b) Code 11001 on a thick substrate



--- Resonator  $S_{21}$ -1011  
 — Wireless tag-1011

(c) Code 1011 on a thin substrate



--- Resonator  $S_{21}$ -1101  
 — Wireless tag-1101

(d) Code 1101 on a thin substrate

FIGURE 9: Measured results of the proposed microwave tag in wireless experiments.

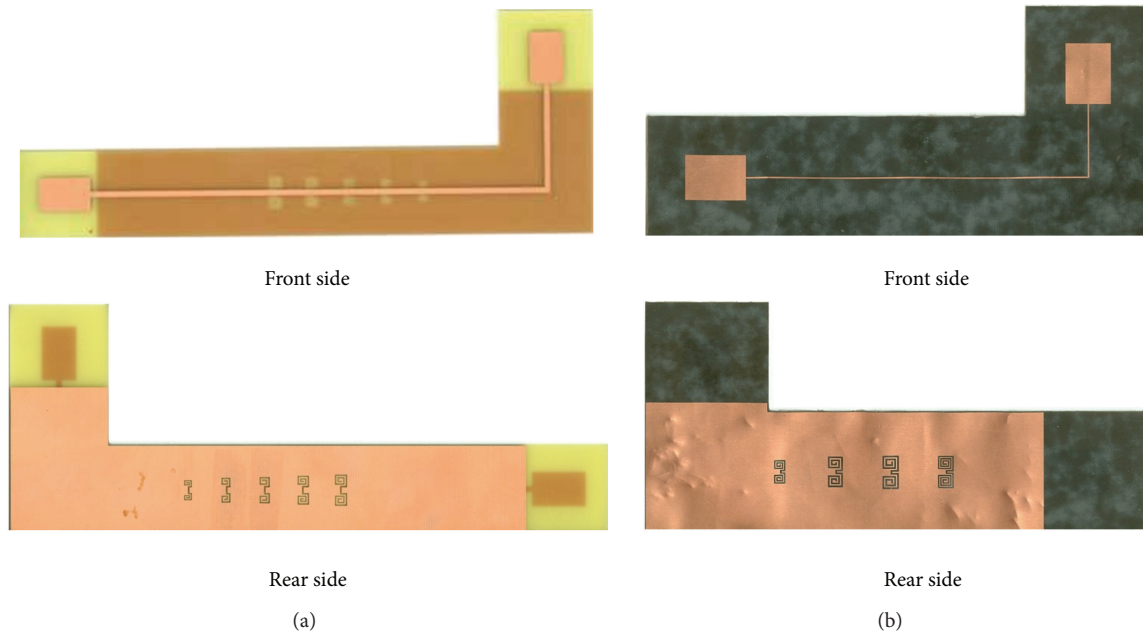


FIGURE 10: Photographs of implemented microwave tag systems: (a) on the thick substrate, (b) on the flexible thin substrate.

## References

- [1] S. Preradovic and N. C. Karmakar, "Chipless RFID: bar code of the future," *IEEE Microwave Magazine*, vol. 11, no. 7, pp. 87–97, 2010.
- [2] F. Michahelles, F. Thiesse, A. Schmidt, and J. R. Williams, "Pervasive RFID and near field communication technology," *IEEE Pervasive Computing*, vol. 6, no. 3, pp. 94–97, 2007.
- [3] S.-M. Han, O. Popov, and A. Dmitriev, "Flexible chaotic UWB communication system with adjustable channel bandwidth in CMOS technology," *IEEE Transactions on Microwave Theory and Techniques*, vol. 56, no. 10, pp. 2229–2236, 2008.
- [4] I. Jalaly and I. D. Robertson, "RF barcodes using multiple frequency bands," in *Proceedings of the IEEE MTT-S International Microwave Symposium*, pp. 139–142, June 2005.
- [5] S. Härmä, V. P. Plessky, X. Li, and P. Hartogh, "Feasibility of ultra-wideband SAW RFID tags meeting FCC rules," *IEEE Transactions on Ultrasonics, Ferroelectrics, and Frequency Control*, vol. 56, no. 4, pp. 812–820, 2009.
- [6] S. Preradovic, I. Balbin, N. C. Karmakar, and G. F. Swiegers, "Multiresonator-based chipless RFID system for low-cost item tracking," *IEEE Transactions on Microwave Theory and Techniques*, vol. 57, no. 5, pp. 1411–1419, 2009.
- [7] M. Schüßler, C. Mandel, M. Maasch, A. Giere, and R. Jakoby, "Phase modulation scheme for chipless RFID- and wireless sensor tags," in *Proceedings of the Asia Pacific Microwave Conference 2009 (APMC '09)*, pp. 229–232, Singapore, December 2009.
- [8] S. Preradovic and N. C. Karmakar, "Multiresonator based chipless RFID tag and dedicated RFID reader," in *Proceedings of the IEEE MTT-S International Microwave Symposium (MTT '10)*, pp. 1520–1523, May 2010.
- [9] A. Islam, S. Bhuiyan, and N. Karmakar, "A novel compact chipless RFID tag and near-field reader," in *Proceedings of the Asia Pacific Microwave Conference*, pp. 1518–1521, December 2011.
- [10] H.-S. Jang, W.-G. Lim, K.-S. Oh, S.-M. Moon, and J.-W. Yu, "Design of low-cost chipless system using printable chipless tag with electromagnetic code," *IEEE Microwave and Wireless Components Letters*, vol. 20, no. 11, pp. 640–642, 2010.
- [11] J. Jung, H. Lee, and Y. Lim, "Broadband flexible comb-shaped monopole antenna," *IET Microwaves, Antennas and Propagation*, vol. 3, no. 2, pp. 325–332, 2009.
- [12] S. Zhu and R. Langley, "Dual-band wearable textile antenna on an EBG substrate," *IEEE Transactions on Antennas and Propagation*, vol. 57, no. 4, pp. 926–935, 2009.
- [13] C.-S. Kim, J. S. Lim, S. Nam, K. Y. Kang, and D. Ahn, "Equivalent circuit modeling of spiral defected ground structure for microstrip line," *Electronics Letters*, vol. 38, no. 19, pp. 1109–1110, 2002.
- [14] D. Ahn, J. S. Park, C. S. Kim, J. Kim, Y. Qian, and T. Itoh, "A design of the low-pass filter using the novel microstrip defected ground structure," *IEEE Transactions on Microwave Theory and Techniques*, vol. 49, no. 1, pp. 86–93, 2001.
- [15] T. Aboufoul, A. Alomainy, and C. Parini, "Reconfiguring UWB monopole antenna for cognitive radio applications using GaAs FET switches," *IEEE Antennas and Wireless Propagation Letters*, vol. 11, pp. 392–394, 2012.
- [16] P. Moeikham, C. Mahatthanajatuphat, and P. Akkaraekthalin, "A compact UWB antenna with a quarter-wavelength strip in a rectangular slot for 5.5 GHz band notch," *International Journal of Antennas and Propagation*, vol. 2013, no. 9, Article ID 574128, 2013.
- [17] C. A. Balanis, *Antenna Theory*, Wiley & Sons, New York, NY, USA, 2nd edition, 2001.

## Research Article

# Differential and Single-Ended Microstrip Lines Loaded with Slotted Magnetic-LC Resonators

J. Naqui, M. Durán-Sindreu, and F. Martín

*GEMMA/CIMITEC, Departament d'Enginyeria Electrònica, Universitat Autònoma de Barcelona, Bellaterra, 08193 Barcelona, Spain*

Correspondence should be addressed to F. Martín; [ferran.martin@uab.es](mailto:ferran.martin@uab.es)

Received 28 February 2013; Revised 25 April 2013; Accepted 20 May 2013

Academic Editor: Sha Luo

Copyright © 2013 J. Naqui et al. This is an open access article distributed under the Creative Commons Attribution License, which permits unrestricted use, distribution, and reproduction in any medium, provided the original work is properly cited.

This paper is focused on magnetic-LC (MLC) resonators, namely, slotted resonators that can be considered the complementary counterparts of the so-called electric-LC (ELC) resonators. Both resonators exhibit two symmetry planes (i.e., they are bisymmetric), one of them being an electric wall and the other a magnetic wall at the fundamental resonance. Therefore, compared to other electrically small resonators such as folded stepped impedance resonators (SIRs), split ring resonators (SRRs), and their complementary counterparts, MLC and ELC resonators exhibit a very rich phenomenology. In this paper, single-ended microstrip lines and differential microstrip lines loaded with MLC resonators are studied, and potential applications are highlighted.

## 1. Introduction

Split-ring resonators (SRRs) [1, 2] and their complementary counterparts (CSRRs) [3] (Figure 1) have been extensively used for the implementation of metamaterials and many devices based on them [4]. SRRs can be excited by means of a uniform axial ( $z$  direction) time-varying magnetic field and/or by an electric field applied in the plane of the particle ( $y$  direction); that is, the particle exhibits bianisotropy [5]. The distribution of charges at the fundamental resonance (see Figure 1(a)) reveals that the symmetry plane of the SRR is an electric wall at that frequency. From duality considerations, it follows that the CSRR can be excited through an axial electric field and/or a magnetic field applied in the  $y$  direction, whose symmetry plane behaves as a virtual magnetic wall at the fundamental resonance [6]. Capacitively loaded (C loaded) loops and folded stepped impedance resonators (SIRs), and their complementary counterparts (Figure 2), exhibit a similar phenomenology when they are illuminated with properly polarized radiation to drive the particles.

As long as SRRs, C-loaded loops, folded SIRs, and their dual particles are electrically small, they can be used for the implementation of effective media metamaterials. Specifically, SRRs, C-loaded loops, and folded SIRs are useful for

the implementation of negative permeability media following the Lorentz model [1, 7], whereas CSRRs, complementary C-loaded loops, and complementary SIRs can be used as building blocks for the implementation of negative permittivity artificial media [3, 8]. However, resonant-type negative permittivity media can also be achieved by means of metallic particles, as it was pointed out by Schurig and co workers [9]. The particle reported in [9] and depicted in Figure 3 was called electric-LC (ELC) resonator. It was argued that such particle cannot be excited by means of a uniform axial magnetic field since the currents in both loops are opposite at the fundamental resonance; namely, the instantaneous current is clockwise in one of the loops and counterclockwise in the other one. This means that, at the fundamental resonance, the ELC does not exhibit a net magnetic dipole moment in the axial direction, and for such reason it cannot be driven by means of a uniform axial time-varying magnetic field. However, an electric dipole moment appears in the orthogonal direction to the electric wall (indicated in Figure 3), which means that the ELC can be excited through a uniform time-varying electric field applied to that direction. This is the reason that explains the terminology used to designate this particle, which prevents bianisotropy. Notice also that there is another symmetry plane in the particle that acts as a magnetic

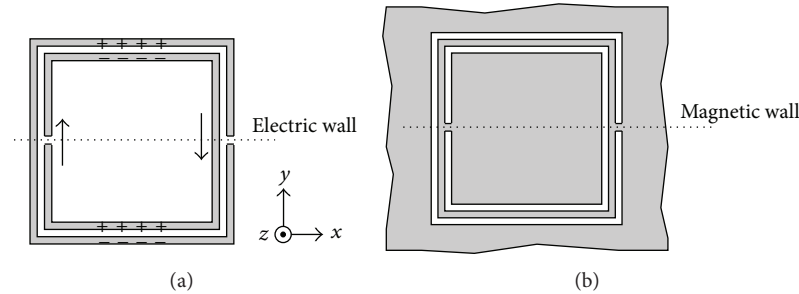


FIGURE 1: Typical topology of an SRR (a) and a CSRR (b). A sketch of the currents and the distribution of charges for the SRR at the fundamental resonance is also indicated (notice that the symmetry plane is an electric wall). From Babinet's principle, it follows that the CSRR exhibits a magnetic wall at the symmetry plane.

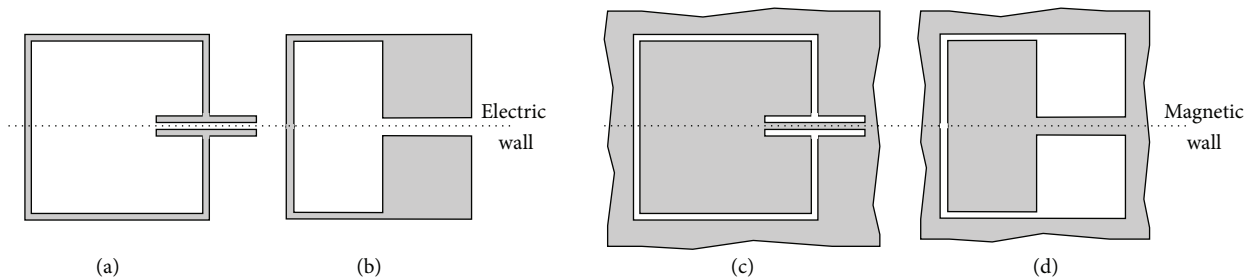


FIGURE 2: Typical topology of a capacitively loaded loop (a), a folded SIR (b), a complementary capacitively loaded loop (c), and a complementary folded SIR (d).

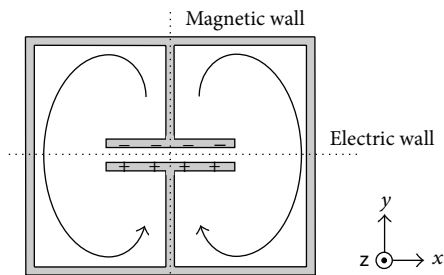


FIGURE 3: Typical topology of an ELC resonator, indicating the electric and magnetic walls and a sketch of the currents and the charge distribution at the fundamental resonance.

wall at the fundamental resonance by virtue of the symmetry in the currents and charges with regard to that plane.

The previous electrically small resonators, including the ELC, can also be used as loading resonant elements in planar transmission lines, where the fields are no longer uniform. In particular, for the ELC, if the driving fields are not uniform, it is also possible to magnetically drive the particle. This can be achieved, for instance, by forcing opposite magnetic flux lines in the loops of the ELC. According to this, the ELC can be a very interesting and useful particle as a loading element in planar transmission lines. However, the main focus in this paper is the study of the dual particle of the ELC, that is, the magnetic-LC (MLC) resonator. This is a slot resonator that can be etched in the ground plane of a single-ended microstrip or a differential microstrip line. The analysis of this

particle as well as the potential applications in microstrip configuration, is the main objective of the present work.

## 2. Magnetic-LC (MLC) Resonators

A typical topology of a square-shaped MLC resonator is depicted in Figure 4(a). It is the negative image of the ELC. Hence, by applying the Babinet's principle, it follows that the MLC can be excited by means of a time-varying magnetic field applied in the plane of the particle ( $y$  direction), but not by a uniform electric field normal to the particle plane (which is the usual driving mechanism in CSRRs [3] and in the complementary structures of Figure 2).

Like the ELC, the MLC exhibits two symmetry planes, one being a magnetic wall and the other an electric wall at the fundamental resonance. However, notice that the magnetic and electric walls are rotated  $90^\circ$  compared to those of the ELC. If the aspect ratio of the slot widths  $w_1/w_2$  is high enough, a quasistatic approximation can be made, and the particle can be described by means of a lumped element-equivalent circuit model, depicted in Figure 4(b). The inductance  $L_m$  accounts for the inductive path connecting the two inner metallic regions of the particle. This inductance is parallel connected to the capacitances designated as  $C_m$  that model the slots present between both inner halves of the MLC. Finally, the edge capacitance of the external square-shaped slot ring is called  $C_g$ , and it can be divided into the capacitances of the two MLC halves, as depicted in Figure 4(b).

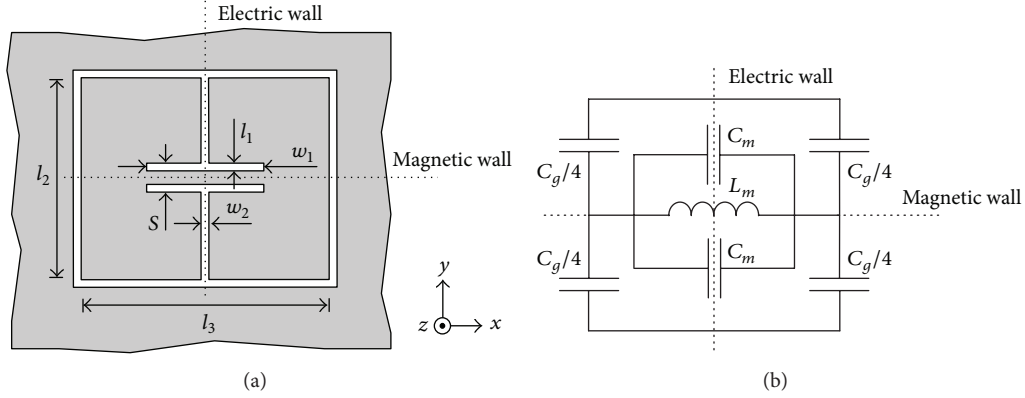


FIGURE 4: Typical topology of an MLC (a) and its equivalent circuit model (b). The relevant dimensions and the electric and magnetic walls are indicated.

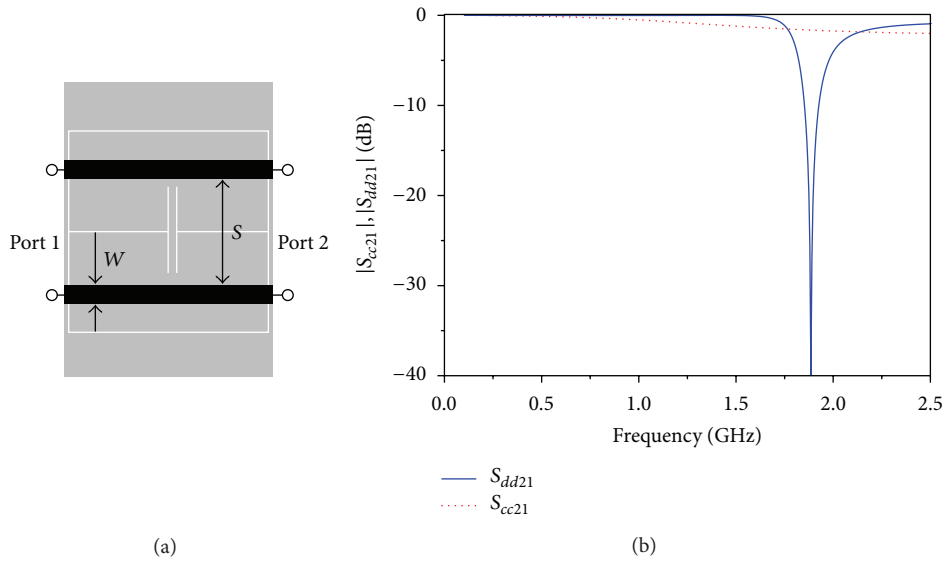


FIGURE 5: Differential microstrip line loaded with an MLC with the electric wall aligned with the line (a) and frequency response (transmission coefficient) for the common ( $S_{cc21}$ ) and differential ( $S_{dd21}$ ) modes (b). The substrate is Rogers RO3010 with thickness  $h = 1.27$  mm and dielectric constant  $\epsilon_r = 11.2$ . The line dimensions are  $W = 1$  mm and  $S = 5$  mm, corresponding to a  $50 \Omega$  odd-mode impedance without the presence of the MLC. The MLC dimensions are  $w_1 = 4$  mm,  $w_2 = l_1 = s = 0.2$  mm, and  $l_2 = l_3 = 10$  mm.

Compared to the other complementary structures shown in Figures 1 and 2, which exhibit a magnetic wall at its unique symmetry plane, the MLC exhibits not only a magnetic wall, but also an electric wall, and this additional wall can be useful in certain applications, as it is discussed in the next sections.

### 3. Single-Ended Microstrip and Differential Microstrip Lines Loaded with MLCs

The unusual electric wall that the MLC exhibits at resonance (in comparison to other slotted resonators) opens new research lines. Let us now consider the MLC loading both single-ended microstrip and differential microstrip transmission lines by assuming that the electric wall of the MLC is aligned with the symmetry plane of the lines.

**3.1. Differential Microstrip Lines Loaded with MLCs.** Figure 5(a) depicts a differential microstrip line loaded with an MLC with the electric wall aligned with the symmetry plane of the line. For the common mode, the symmetry plane of the line is a magnetic wall. Therefore, MLC excitation is not expected for this mode. Conversely, for the differential mode, there is an electric wall at the symmetry plane, and the MLC can be driven. The vertical components of the electric field generated by each individual line under differential mode operation are contra directional (i.e., upwards in one line and downwards in the other line of the pair). Therefore, as long as each inner half of the MLC is below each line of the differential pair, the particle can be excited by the non uniform electric field generated under differential mode excitation. This behavior has been verified through the electromagnetic

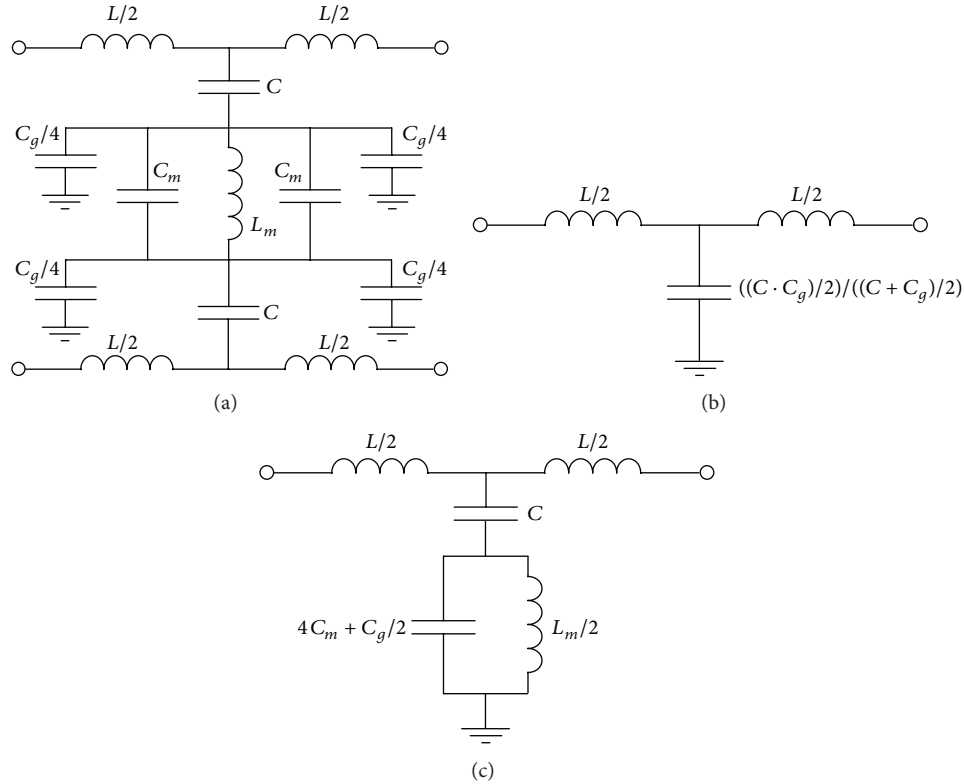


FIGURE 6: (a) Lumped element-equivalent circuit model of a differential microstrip line loaded with an MLC with the electric wall aligned with the line; (b) circuit model for the even mode, where the symmetry plane is an open circuit; (c) circuit model for the odd mode, the symmetry plane being a short circuit.

simulation of the structure depicted in Figure 5(a) by means of the *Agilent Momentum* commercial software for both the common and the differential mode (see Figure 5(b)). As expected, the differential line is roughly transparent for the common mode, but it exhibits a notch in the transmission coefficient for the differential mode.

The circuit model of the structure of Figure 5(a) is depicted in Figure 6, where the equivalent circuits for the odd (or differential) and even (or common) modes are also included. The model includes the elements describing the MLC, plus the line inductance  $L$  and capacitance  $C$ . Actually, the former is the line inductance with the presence of the MLC and the latter accounts for the electric coupling between the line and the MLC. As it can be appreciated, for the common mode there is no transmission zero even though the shunt capacitance is modified. On the contrary, for the differential mode, the resulting model is the same as that for a CSRR-loaded microstrip line which exhibits a transmission notch [10]. In order to validate the model for the differential mode, we have considered the structure depicted in Figure 7(a) which is electrically smaller at resonance than that in Figure 5(a) mainly by virtue of the higher aspect ratio  $w_1/w_2$  (by enlarging the capacitor length  $l_1$  also achieves an electrical size reduction). Under these conditions, it is expected that the model is valid in a wider frequency range. We have performed the full-wave electromagnetic simulation of the structure for the differential mode, and we have extracted the elements

of that model by means of a procedure reported elsewhere [10]. Qualitatively, that technique is based on measurable characteristics of the transmission and reflection coefficients provided by the electromagnetic simulation. Briefly, the lumped elements are obtained by means of the following conditions: (i) the transmission zero frequency corresponds to the frequency that the shunt impedance nulls, (ii) the frequency for which the shunt admittance vanishes is the resonant frequency of the parallel tank, (iii) the frequency whose phase of the transmission coefficient is  $\pi/2$  is where the series and the shunt impedances are conjugate, and (iv) the intersection between the reflection coefficient and the unit normalized resistance circle gives the series impedance. The electromagnetic simulation and the circuit simulation of the equivalent circuit model using the extracted parameters are depicted in Figure 7(b). As can be seen the agreement is good, hence validating the proposed model of the MLC-loaded differential microstrip line.

**3.2. Single-Ended Microstrip Lines Loaded with MLCs.** Let us now consider the MLC loading a single-ended microstrip transmission line, as depicted in Figure 8. Since the symmetry plane is a magnetic wall, the MLC cannot be excited. The proposed circuit model is depicted in Figure 9(a), which is similar to that reported in [11] for folded SIR-loaded coplanar waveguides. After applying the magnetic wall concept, this circuit model can be simplified as Figure 9(b) illustrates;

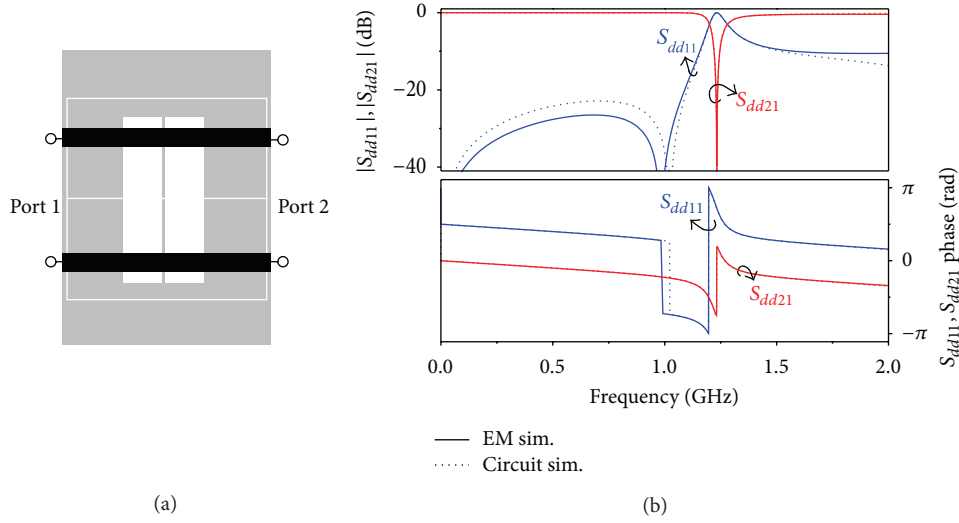


FIGURE 7: Layout (a) and differential mode frequency response (b) for a differential microstrip line loaded with an MLC with the electric wall aligned with the line and for its circuit model of Figure 6. The dimensions and the substrate are the same as those given in the caption of Figure 5, except for  $l_1 = 2$  mm and  $w_1 = 8$  mm. The circuit parameters are  $L = 6.07$  nH,  $C = 1.53$  pF,  $4C_m + C_g/2 = 7.47$  pF (where for dimensions  $C_g \approx 14C_m$ ), and  $L_m = 3.71$  nH.

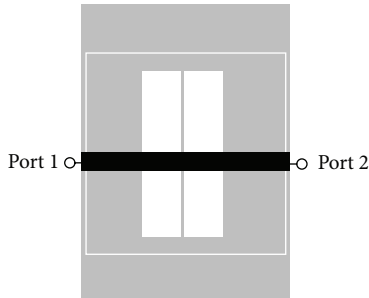


FIGURE 8: Microstrip line loaded with an MLC with the electric wall aligned with the line. The dimensions and the substrate are the same as those considered in Figure 7.

that is, it is a transmission line model with modified shunt capacitance. However, a notch in the transmission coefficient is not expected according to this model.

The interest in these single-ended microstrip transmission lines loaded with MLCs may be the truncation of symmetry, for instance, by means of a lateral displacement of the particle. In this case, the symmetry planes are no longer aligned, and the particle can be excited by the electric field generated by the line. The effect of this symmetry truncation by laterally shifting the MLC can be taken into account in the model of Figure 9(a) by simply considering the coupling capacitances (i.e.,  $C_1$  and  $C_2$ ) as variable capacitances. From the circuit model viewpoint, these asymmetric values of the coupling capacitances allow current flowing through the MLC inductance and capacitance, and hence the particle is electrically driven by the line. As reported in [11], such kind of circuit can be useful for the implementation of displacement sensors or radio frequency (RF) barcodes.

We have simulated the structure of Figure 8 by considering two different lateral displacements (0.5 and 2 mm) of the MLC. The results are depicted in Figure 10. In order to extract the lumped element values of its circuit model, as a starting point we consider the values given in the caption of Figure 7 since the same dimensions and substrate are considered. Afterwards, we have adjusted the variable coupling capacitances by curve fitting the electromagnetic simulation, which depend on the amount of displacement. The other elements of the circuit left nearly unaltered (a slight optimization may be required), except for the line inductance which is also modified by the position of the slotted resonator. The circuit simulations, also depicted in Figure 10, are in good agreement with the electromagnetic simulations. Therefore, the proposed model is validated, and it is demonstrated that the lateral shift of the MLC can be basically taken into account by modifying the coupling capacitances and the line inductance.

#### 4. Potential Applications

Etched in the ground plane of differential microstrip lines, MLC resonators can be used for the implementation of balanced notch filters and stop-band filters. This functionality is clear to the light of the results depicted in Figure 7, where a notch for the differential mode appears in the vicinity of the fundamental resonance of the MLC. The rejection band can be widened by etching further MLC resonators with slightly different resonance frequency (as reported in [12] for the design of SRR-based CPW stopband filters) or with identical resonance frequency but separated by a small distance in order to enhance interresonator's coupling (as discussed in [13] in reference to common mode suppression in differential lines by means of CSRRs).

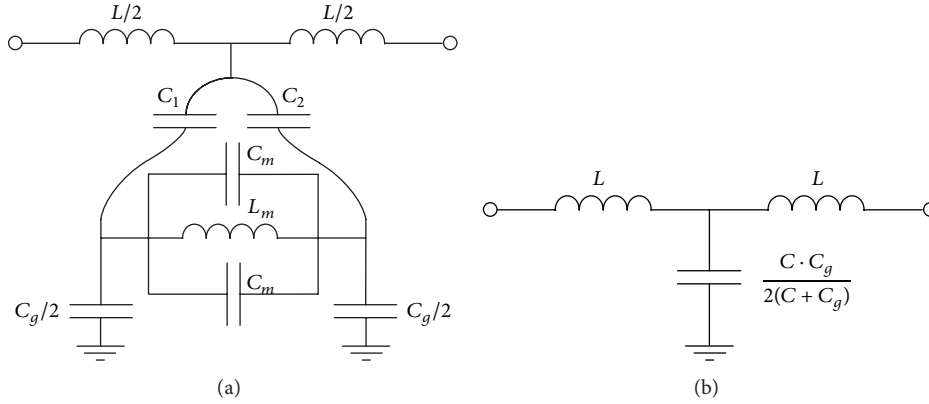


FIGURE 9: (a) Lumped element-equivalent circuit model of a microstrip line loaded with an MLC whose electric wall is aligned with or laterally displaced with regard to the line; (b) circuit model after applying the magnetic wall concept under the assumption of alignment, that is,  $C_1 = C_2 = C/2$ .

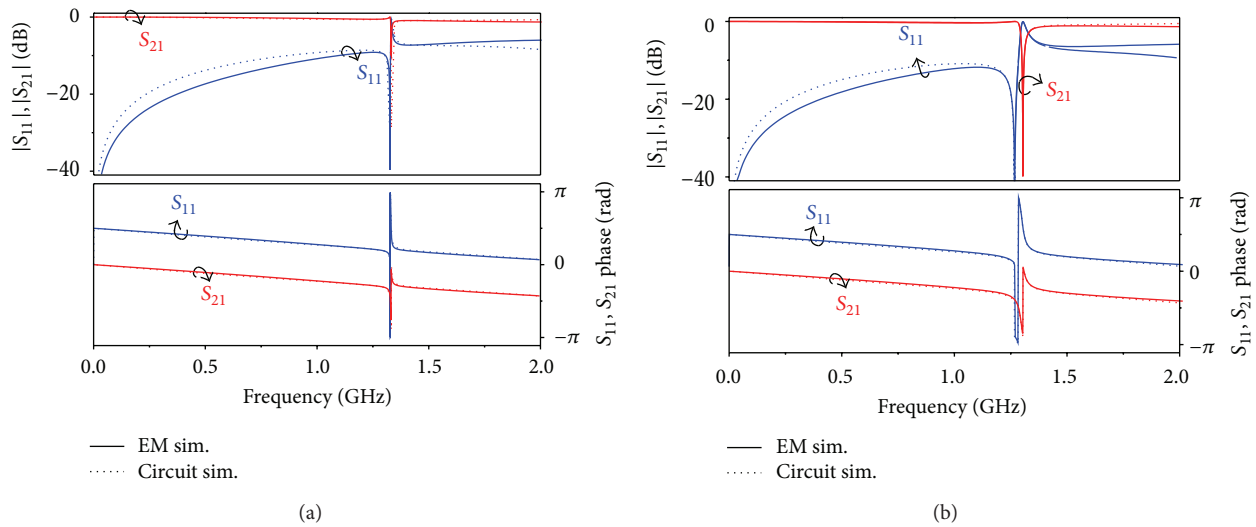


FIGURE 10: Frequency response for the structure of Figure 8 that results by laterally shifting the MLC 0.5 mm (a) and 2 mm (b) and for its circuit model of Figure 9. The circuit parameters are  $L_m = 3.71$  nH and  $C_g = 9.5$  pF; for 0.5 mm,  $L = 9.48$  nH,  $C_1 = 0.89$  pF,  $C_2 = 0.36$  pF, and  $C_m = 0.59$  pF; for 2 mm,  $L = 8.94$  nH,  $C_1 = 1.36$  pF,  $C_2 = 0.083$  pF, and  $C_m = 0.66$  pF.

With regard to microstrip lines loaded with MLCs, we can take benefit of the effects of a lateral shift (or another means of symmetry truncation) in the transmission coefficient. Namely, the line is transparent if the electric wall of the MLC is perfectly aligned with the symmetry plane of the line. However, a notch appears when the MLC is shifted in the transverse direction, and the bandwidth and magnitude of the notch increase with the displacement (see Figure 10). Similarly, a notch is expected if the MLC is not displaced, but it is nonsymmetrically loaded with a certain dielectric load. Thus, the structure can be used for sensing purposes [14–17]. Furthermore, microstrip lines loaded with multiple MLCs can be used as RF bar codes, where each bit is associated to a certain resonator (and its resonance frequency), and the logic states “1” or “0” are simply set by etching the MLCs symmetrically or laterally shifted or by other means of truncating the symmetry (RF bar codes not based on such

a symmetry approach were reported in [18]). As an example, Figure 11(a) shows a photograph of a 3-bit bar code with the central MLC aligned with the line and the external ones laterally displaced (corresponding to the code “101”). The frequency response is depicted in Figure 11(b) and exhibits a transmission zero at the frequencies of the external resonators, in coherence with the considered codification. The resonators were designed to achieve relatively narrow notches (this is a key issue to bits embedding and the related spectral band efficiency). Even though the notch level (intimately related to the bandwidth) is not very deep, this is not a critical drawback in binary bar codes. It is also interesting to mention that compared to CPW-based RF-bar codes, implemented by means of folded SIRs or SRRs (they also exhibit an electric wall at their symmetry plane) [11], the proposed bar code is more simple since no parasitic modes

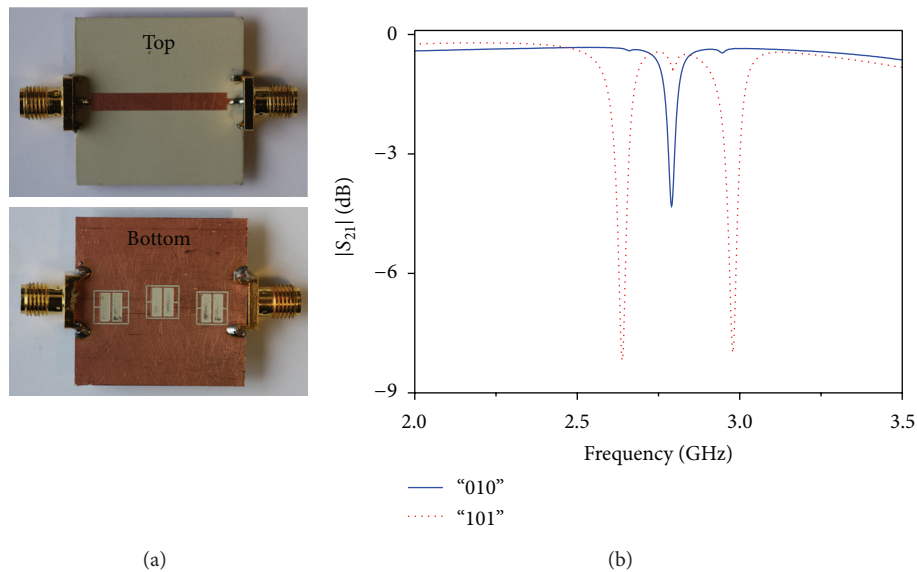


FIGURE 11: Photograph of a 3-bit RF bar code (codified as “101”) (a) and measured frequency response (b). For completeness, the measurement for the code “010” is also shown. The substrate is *Rogers RO3010* with thickness  $h = 1.27$  mm, dielectric constant  $\epsilon_r = 11.2$ , and loss tangent  $\tan \delta = 0.0023$ . The line width is designed to minimize the insertion loss with the presence of the MLCs symmetrically etched, that is,  $W = 3.13$  mm. The MLC dimensions are  $w_1 = 5.2$  mm,  $w_2 = s = 0.2$  mm,  $l_1 = 1.9$  mm,  $l_2(2.6 \text{ GHz}) = 6.32$  mm,  $l_2(2.8 \text{ GHz}) = 6$  mm,  $l_2(3 \text{ GHz}) = 5.72$  mm, and  $l_3 = 6$  mm. The distance between adjacent resonators is set to that for which interresonator coupling can be neglected, that is, 3 mm. The lateral displacement to set the logic state “1” is 1 mm.

are generated by displacing the MLCs (in contrast, air bridges were necessary in the CPW bar codes reported in [11]). Alternatively, codification can be achieved by symmetrically etching the MLCs and truncating symmetry in the required resonator by adding adhesives with metallic or dielectric loads.

## 5. Conclusions

In conclusion, it has been shown that the MLC is a slot resonator that exhibits two symmetry planes, one being a magnetic wall and the other one an electric wall at the fundamental resonance. Given that other related slot resonators do not exhibit any electric wall, this paper focuses on such wall, which brings a wider variety of applications. If the driving fields of the particle are uniform, the MLC cannot be excited by an electric field orthogonal to the particle plane, but by means of a magnetic field in the plane of the particle. However, it has been shown that, in single-ended microstrip lines and differential microstrip lines, where the fields are no longer uniform, the MLC can be electrically excited. Equivalent circuit models of both differential and single-ended microstrip lines loaded with MLCs with the electric wall aligned with the symmetry plane of the lines have been reported and validated. Finally, some applications have been highlighted, including balanced notch filters, as well as sensors and bar codes based on the truncation of symmetry.

## Acknowledgments

This work has been supported by MINECO, Spain (Projects TEC2010-17512, CSD2008-00066, and TEC2011-13615-E)

and by AGAUR-*Generalitat de Catalunya*, through Project 2009SGR-421. Jordi Naqui is also in debt to MINECO Spain for supporting his work through the FPU Grant AP2010-0431.

## References

- [1] J. B. Pendry, A. J. Holden, D. J. Robbins, and W. J. Stewart, “Magnetism from conductors and enhanced nonlinear phenomena,” *IEEE Transactions on Microwave Theory and Techniques*, vol. 47, no. 11, pp. 2075–2084, 1999.
- [2] F. Martín, J. Bonache, F. Falcone, M. Sorolla, and R. Marqués, “Split ring resonator-based left-handed coplanar waveguide,” *Applied Physics Letters*, vol. 83, no. 22, pp. 4652–4654, 2003.
- [3] F. Falcone, T. Lopetegi, J. D. Baena, R. Marqués, F. Martín, and M. Sorolla, “Effective negative- $\epsilon$  stopband microstrip lines based on complementary split ring resonators,” *IEEE Microwave and Wireless Components Letters*, vol. 14, no. 6, pp. 280–282, 2004.
- [4] R. Marqués, F. Martín, and M. Sorolla, *Metamaterials with Negative Parameters: Theory, Design and Microwave Applications*, John Wiley & Sons, New York, NY, USA, 2008.
- [5] R. Marques, F. Medina, and R. Rafii-El-Idrissi, “Role of bi-anisotropy in negative permeability and left handed metamaterials,” *Physical Review B*, vol. 65, paper 144441, 2002.
- [6] J. D. Baena, J. Bonache, F. Martín et al., “Equivalent-circuit models for split-ring resonators and complementary split-ring resonators coupled to planar transmission lines,” *IEEE Transactions on Microwave Theory and Techniques*, vol. 53, no. 4, pp. 1451–1460, 2005.
- [7] D. R. Smith, W. J. Padilla, D. C. Vier, S. C. Nemat-Nasser, and S. Schultz, “Composite medium with simultaneously negative

- permeability and permittivity,” *Physical Review Letters*, vol. 84, no. 18, pp. 4184–4187, 2000.
- [8] F. Falcone, T. Lopetegi, M. A. G. Laso et al., “Babinet principle applied to the design of metasurfaces and metamaterials,” *Physical Review Letters*, vol. 93, no. 19, Article ID 197401, 2004.
- [9] D. Schurig, J. J. Mock, and D. R. Smith, “Electric-field-coupled resonators for negative permittivity metamaterials,” *Applied Physics Letters*, vol. 88, no. 4, Article ID 041109, pp. 1–3, 2006.
- [10] J. Bonache, M. Gil, I. Gil, J. Garcia-García, and F. Martín, “On the electrical characteristics of complementary metamaterial resonators,” *IEEE Microwave and Wireless Components Letters*, vol. 16, pp. 543–545, 2006.
- [11] J. Naqui, M. Durán-Sindreu, and F. Martín, “On the symmetry properties of coplanar waveguides loaded with symmetric resonators: analysis and potential applications,” in *Proceedings of IEEE MTT-S International Microwave Symposium*, Montreal, Canada, June 2012.
- [12] F. Martín, F. Falcone, J. Bonache, R. Marqués, and M. Sorolla, “Miniaturized coplanar waveguide stop band filters based on multiple tuned split ring resonators,” *IEEE Microwave and Wireless Components Letters*, vol. 13, no. 12, pp. 511–513, 2003.
- [13] J. Naqui, A. Fernández-Prieto, M. Durán-Sindreu et al., “Common mode suppression in microstrip differential lines by means of complementary split ring resonators: theory and applications,” *IEEE Transactions on Microwave Theory and Techniques*, vol. 60, pp. 3023–3034, 2012.
- [14] C. Mandel, B. Kubina, M. Schusler, and R. Jakoby, “Passive chipless wireless sensor for two-dimensional displacement measurement,” in *Proceedings of the 14th European Microwave Conference (EuMC '11)*, pp. 79–82, October 2011.
- [15] J. Naqui, M. Durán-Sindreu, and F. Martín, “Alignment and position sensors based on split ring resonators,” *Sensors*, vol. 12, pp. 11790–11797, 2012.
- [16] M. Puentes, M. Maasch, M. Schubler, and R. Jakoby, “Frequency multiplexed 2-dimensional sensor array based on split-ring resonators for organic tissue analysis,” *IEEE Transactions on Microwave Theory and Techniques*, vol. 60, no. 6, pp. 1720–1727, 2012.
- [17] A. Karami Horestani, C. Fumeaux, S. F. Al-Sarawi, and D. Abbott, “Displacement sensor based on diamond-shaped tapered split ring resonator,” *IEEE Sensors Journal*, vol. 13, no. 4, pp. 1153–1160, 2013.
- [18] S. Preradovic and N. C. Karmakar, “Chipless RFID: bar code of the future,” *IEEE Microwave Magazine*, vol. 11, no. 7, pp. 87–97, 2010.

## Research Article

# Impact of the Gate Width of $\text{Al}_{0.27}\text{Ga}_{0.73}\text{N}/\text{AlN}/\text{Al}_{0.04}\text{Ga}_{0.96}\text{N}/\text{GaN}$ HEMT on Its Characteristics

Liwei Jin,<sup>1</sup> Zhiqun Cheng,<sup>1,2</sup> and Qingna Wang<sup>1</sup>

<sup>1</sup> Key Laboratory of RF Circuit and System, Education Ministry, Hangzhou Dianzi University, Hangzhou 310018, China

<sup>2</sup> Key Laboratory of Nanodevices and Applications, Suzhou Institute of Nano-Tech and Nano-Bionics, Chinese Academy of Sciences, Suzhou 215123, China

Correspondence should be addressed to Zhiqun Cheng; [zhiqun@hdu.edu.cn](mailto:zhiqun@hdu.edu.cn)

Received 17 March 2013; Accepted 25 April 2013

Academic Editor: Haiwen Liu

Copyright © 2013 Liwei Jin et al. This is an open access article distributed under the Creative Commons Attribution License, which permits unrestricted use, distribution, and reproduction in any medium, provided the original work is properly cited.

This paper presents impact of layout sizes of  $\text{Al}_{0.27}\text{Ga}_{0.73}\text{N}/\text{AlN}/\text{Al}_{0.04}\text{Ga}_{0.96}\text{N}/\text{GaN}$  HEMT heterostructure high-mobility transistors (HEMTs) on SiC substrate on its characteristics that include the threshold voltage, the maximum transconductance, characteristic frequency, and the maximum oscillation frequency. The changing parameters include the gate finger number, the gate width per finger. The measurement results based on common-source devices demonstrate that the above parameters have different effects on the threshold voltage, maximum transconductance, and frequency characteristics.

## 1. Introduction

As the third typical semiconductor material, GaN has been widely investigated for several years due to their wide gap and high breakdown field. It will become an ideal candidate for high-power, high-frequency, and high-temperature electronic devices [1–4]. By the great development of the material quality and device processing techniques, AlGaN/GaN HEMT has been much improved in both DC and RF performances.

Performances of monolithic microwave integrated circuits (MMICs) are influenced by the characteristics of active devices. There are many papers about improving its DC and AC performances by changing material or structure of epitaxial layer of AlGaN/GaN HEMTs [5–8]. In recent years, a novel structure  $\text{Al}_x\text{Ga}_{1-x}\text{N}/\text{Al}_y\text{Ga}_{1-y}\text{N}/\text{GaN}$  HEMT with low Al composite inserting layer  $\text{Al}_y\text{Ga}_{1-y}\text{N}$  has been reported [9–11] and MMICs based on AlGaN/GaN HEMT are designed by our group [12]. This paper will present the impact of layout sizes of  $\text{Al}_{0.27}\text{Ga}_{0.73}\text{N}/\text{AlN}/\text{Al}_{0.04}\text{Ga}_{0.96}\text{N}/\text{GaN}$  HEMTs based on SiC substrate on its characteristics.

## 2. Material Preparation and Device Fabrication

The layer structure of the device proposed in the study is grown on a SiC substrate. The epitaxial layer consists of an unintentionally doped  $1.5\ \mu\text{m}$  GaN buffer layer, 1 nm AlN spacer layer, 4 nm low Al component  $\text{Al}_{0.04}\text{Ga}_{0.96}\text{N}$ , and a 20 nm  $\text{Al}_{0.27}\text{Ga}_{0.73}\text{N}$  barrier layer as shown in Figure 1. Epitaxial layer structure of  $\text{Al}_{0.27}\text{Ga}_{0.73}\text{N}/\text{AlN}/\text{Al}_{0.04}\text{Ga}_{0.96}\text{N}/\text{GaN}$  HEMT is proposed and optimized by combining theory calculation and TCAD software; detail design process is given in our previous papers [13, 14].

An averaged electron mobility of  $1800\ \text{cm}^2/(\text{v}\cdot\text{s})$  and a sheet carrier density of  $1.0 \times 10^{13}/\text{cm}^2$  are obtained by room temperature Hall measurement. The AlGaN/GaN HEMT fabrication commences with metalizing by high-vacuum evaporation in drain and source; the Ohmic contacts are formed by depositing the metal Ti/Al/Ti/Au and then rapid thermal annealing (RTA) at  $870^\circ\text{C}$  for 50 s in  $\text{N}_2$  ambient. All these steps above result in a low ohmic contact resistance of  $0.6\ \Omega\cdot\text{mm}$ .  $\text{Si}_3\text{N}_4$  film used for passivation is grown by

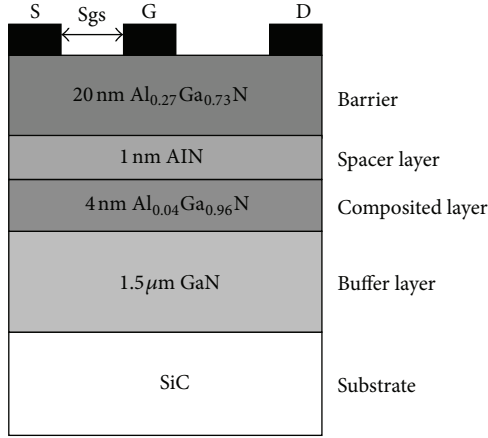


FIGURE 1: Cross section diagram of  $\text{Al}_{0.27}\text{Ga}_{0.73}\text{N}/\text{AlN}/\text{Al}_{0.04}\text{Ga}_{0.96}\text{N}/\text{GaN}$  HEMT.

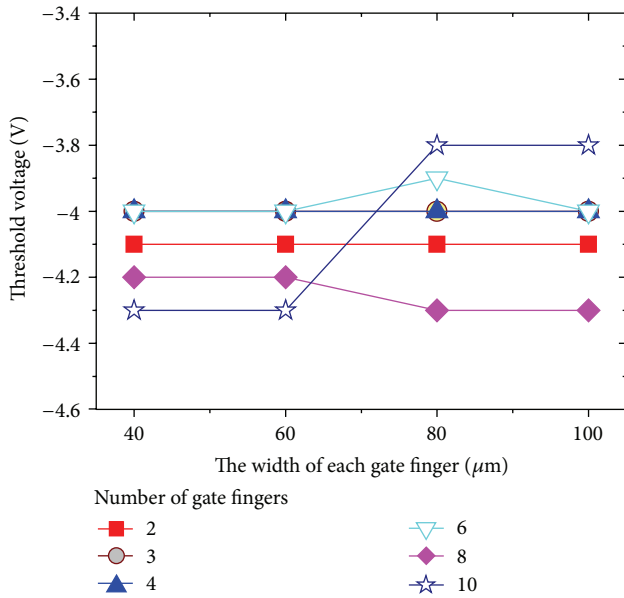


FIGURE 2: Threshold voltage versus the gate width.

PECVD. Then, the T-shaped Schottky gate is formed by Ni/Au evaporation and the subsequent lift-off process.

### 3. The Design of Layout and Analysis of Results

Layout of  $\text{Al}_{0.27}\text{Ga}_{0.73}\text{N}/\text{AlN}/\text{Al}_{0.04}\text{Ga}_{0.96}\text{N}/\text{GaN}$  HEMT is designed including 24 types of samples with different gate fingers numbers and width of each finger. Total gate width of device is supposed to be  $m \times n \mu\text{m}$  ( $m = 2, 3, 4, 6, 8, \text{ and } 10$ ;  $n = 40, 60, 80, \text{ and } 100$ ), where “ $m$ ” represents the finger numbers and “ $n$ ” stands for width of each gate finger. The space between gate and source is  $1 \mu\text{m}$  for all of devices.

**3.1. Threshold Voltage.** Figure 2 presents that threshold voltage of  $\text{Al}_{0.27}\text{Ga}_{0.73}\text{N}/\text{AlN}/\text{Al}_{0.04}\text{Ga}_{0.96}\text{N}/\text{GaN}$  HEMT changes with its gate width. The threshold voltages of the device

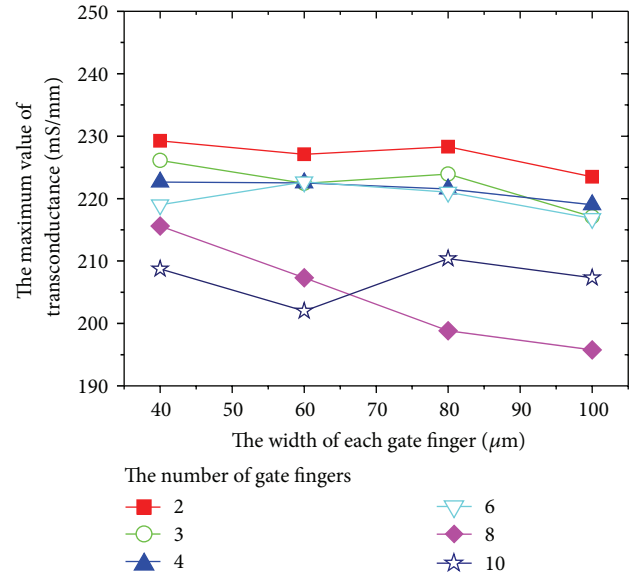


FIGURE 3: The maximum value of transconductance versus the gate width.

almost do not change with the width of each gate finger except gate finger number of 10 and change from  $-3.8$  to  $-4.3$  V with number of gate fingers.

**3.2. Maximum Transconductance.** Figure 3 presents that the maximum transconductance ( $G_{m_{\max}}$ ) of the GaN HEMTs changes with its gate width. The values of  $G_{m_{\max}}$  reduce with the width of each gate finger. When the number of gate fingers is 8, downslope of the values of  $G_{m_{\max}}$  is the largest of them with the width of each gate finger from 215 to 196 mS/mm.

**3.3. Frequency Characteristics.**  $S$  parameters are measured on line at the frequency from 500 MHz to 24 GHz. The current gain ( $|h_{21}|$ ) and the maximum available power gain (MAG) are calculated from measured  $S$  parameters as a function of frequency. The values of characteristic frequency ( $f_t$ ) and the maximum oscillation frequency ( $f_{\max}$ ) are determined by extrapolation of the  $|h_{21}|$  and MAG data at  $-20$  dB/decade. Figures 4 and 5 present that the characteristic frequency and the maximum oscillator frequency change with the gate width, respectively. Both of  $f_t$  and  $f_{\max}$  reduce with increasing the gate width. Both of  $f_t$  and  $f_{\max}$  are influenced larger by the number of gate fingers than by the width of each gate width.

### 4. Conclusion

A novel structure of  $\text{Al}_{0.27}\text{Ga}_{0.73}\text{N}/\text{AlN}/\text{Al}_{0.04}\text{Ga}_{0.96}\text{N}/\text{GaN}$  HEMT with different sizes of layout is successfully designed and fabricated. After measurement, the performances of the threshold voltage, the maximum transconductance, characteristic frequency, and the maximum oscillation frequency with different gate widths of  $\text{Al}_{0.27}\text{Ga}_{0.73}\text{N}/\text{AlN}/\text{Al}_{0.04}\text{Ga}_{0.96}\text{N}/\text{GaN}$  HEMT are analyzed carefully. It is

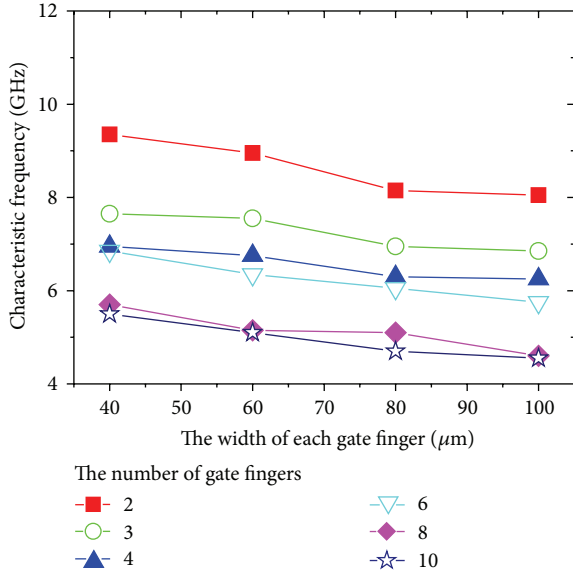


FIGURE 4: Characteristic frequency versus the gate width.

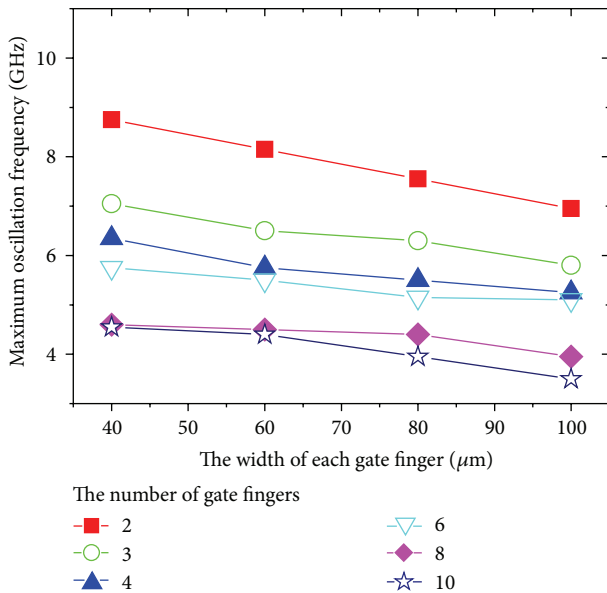


FIGURE 5: The maximum oscillation frequency versus the gate width.

significant for designing AlGaIn/GaN HEMT with excellent performance.

**Acknowledgment**

This work was supported by Natural Science Foundation of Zhejiang Province (no. Z1110937).

**References**

[1] J. G. Cho, Z. J. Li, E. B. Grayeli et al., "Improved thermal interfaces of GaN-diamond composite substrates for HEMT applications," *IEEE Transaction on Components, Packaging and Manufacturing Technology*, vol. 3, no. 1, pp. 79–85, 2013.

[2] A. M. Ho Kwan and K. J. Chen, "A gate overdrive protection technique for improved reliability in AlGaIn/GaN enhancement-mode HEMTs," *IEEE Electron Device Letters*, vol. 34, no. 1, pp. 30–32, 2013.

[3] M. Silvestri, M. J. Uren, and M. Kuball, "Dynamic transconductance dispersion characterization of channel hot-carrier stressed 0.25 μm AlGaIn/GaN HEMTs," *IEEE Electron Device Letters*, vol. 33, no. 11, pp. 1550–1552, 2012.

[4] P. S. Park, D. N. Nath, and S. Rajan, "Quantum capacitance in N-polar GaN/AlGaIn/GaN heterostructures," *IEEE Electron Device Letters*, vol. 33, no. 7, pp. 991–993, 2012.

[5] S. B. Driadi, H. Maher, N. Defrance et al., "AlGaIn/GaN HEMTs on silicon substrate with 206 GHz FMAX," *IEEE Electron Device Letters*, vol. 34, no. 1, pp. 36–38, 2013.

[6] S. Boulay, S. Touati, A. A. Sar et al., "AlGaIn/GaN HEMTs on a (001)-oriented silicon substrate based on 100 nm SiN recessed gate technology for microwave power amplification," *IEEE Transactions on Electron Devices*, vol. 54, no. 11, pp. 2843–2848, 2007.

[7] Y. Hao, L. Yang, X. Ma et al., "High-performance microwave gate-recessed AlGaIn/AlN/GaN MOS-HEMT with 73% power-added efficiency," *IEEE Electron Device Letters*, vol. 32, no. 5, pp. 626–628, 2011.

[8] C. Lee, L. Witkowski, H. Q. Tserng et al., "Effects of AlGaIn GaN HEMT structure on RF reliability," *Electronics Letters*, vol. 41, no. 3, pp. 155–157, 2005.

[9] Z. Cheng, J. Liu, Y. Zhou, Y. Cai, K. J. Chen, and K. M. Lau, "Broadband microwave noise characteristics of high-linearity composite-channel Al<sub>0.3</sub>Ga<sub>0.7</sub>N/Al<sub>0.05</sub>Ga<sub>0.95</sub>N/GaN HEMTs," *IEEE Electron Device Letters*, vol. 26, no. 8, pp. 521–523, 2005.

[10] Z. Q. Cheng, S. Hu, W. J. Zhou, and J. Liu, "Effect of composited-layer Al<sub>y</sub>Ga<sub>1-y</sub>N on performances of AlGaIn/GaN HEMT with unintentionally doping barrier Al<sub>x</sub>Ga<sub>1-x</sub>N," *Microwave and Optical Technology Letters*, vol. 53, no. 6, pp. 1206–1209, 2011.

[11] Z. Q. Cheng, Q. N. Wang, Z. H. Feng, J. B. Song, and J. Y. Yin, "Design and DC parameter extraction of the high linearity Al<sub>0.27</sub>Ga<sub>0.73</sub>N/AlN/Al<sub>0.04</sub>Ga<sub>0.96</sub>N/GaN HEMT," in *Proceedings of the 1st International Conference on Electronics, Communications and Control*, pp. 1979–1981, September 2011.

[12] Z. Cheng, Y. Cai, J. Liu, Y. Zhou, K. M. Lau, and K. J. Chen, "1.9 GHz low noise amplifier using high-linearity and low-noise composite-channel HEMTs," *Microwave and Optical Technology Letters*, vol. 49, no. 6, pp. 1360–1362, 2007.

[13] X. P. Zhou, Z. Q. Cheng, S. Hu, W. J. Zhou, and S. Zhang, "AlGaIn/GaN HEMT device structure optimization design," in *Proceedings of the International Symposium on the Physical and Failure Analysis of Integrated Circuits*, pp. 339–343, July 2009.

[14] Z. Q. Cheng, X. P. Zhou, S. Hu, W. J. Zhou, and S. Zhang, "Optimization design of high linearity Al<sub>x</sub>Ga<sub>1-x</sub>N/Al<sub>y</sub>Ga<sub>1-y</sub>N/GaN high electron mobility transistor," *Acta Physica Sinica*, vol. 59, no. 2, pp. 1252–1257, 2010.

## Research Article

# A Miniaturized Dual-Mode Bandpass Filter Using Slot Spurline Technique

Haiwen Liu,<sup>1,2</sup> Jiuhuai Lei,<sup>2</sup> Jing Wan,<sup>2</sup> Yan Wang,<sup>2</sup> Feng Yang,<sup>1</sup> and Suping Peng<sup>1</sup>

<sup>1</sup> State Key Laboratory of Coal Resources and Safe Mining, China University of Mining & Technology, Beijing 100083, China

<sup>2</sup> School of Information Engineering, East China Jiaotong University, No. 808, East Shuanggang Road, Nanchang 330013, China

Correspondence should be addressed to Haiwen Liu; liuhaiwen@gmail.com

Received 19 February 2013; Revised 21 March 2013; Accepted 16 April 2013

Academic Editor: Amin Abbosh

Copyright © 2013 Haiwen Liu et al. This is an open access article distributed under the Creative Commons Attribution License, which permits unrestricted use, distribution, and reproduction in any medium, provided the original work is properly cited.

A miniaturized dual-mode bandpass filter (BPF) with elliptic function response using slot spurline is designed in this paper. The slot spurline can not only splits the degenerate modes but also determine the type of filter characteristic (Chebyshev or elliptic). To miniaturize the resonator, four sagittate stubs are proposed. For demonstration purpose, a BPF operating at 5.75 GHz for WLAN application was designed, fabricated, and measured. The measured results are in good agreement with the full-wave simulation results.

## 1. Introduction

Dual-mode microstrip filters have been widely used in wireless communications systems because of their advantages in microwave applications requiring high quality narrow-band BPFs with features such as compact size, low cost, and low loss [1–3]. The concept of the dual-mode is based on coupling of the two degenerate modes in a geometrically symmetrical resonator, which is achieved by adding a perturbation element to split the two orthogonal modes. Many research works have been done on microstrip circular ring, square loop, circular disk, and square patch. For example, miniature meander loop resonator structures with microstrip cut perturbation for a dual-mode filter is reported in [4, 5]. In [6], a novel dual-mode resonator with four arrow-shaped patches was proposed. Some modified waveguide structures based on defect ground structure (DGS) are reported to realize bandpass filter (BPF), such as slotline with DGS stubs, defected hairpin resonator, open-loop DGS, and defected SIR [7, 8]. These BPFs with low cost and easy fabrication exhibit excellent bandpass performances. However, dual-mode characteristics of these waveguide structures are not mentioned for circuit synthesis. In our previous work [9], a pentagonal slotline resonator was proposed. The strength and nature of the coupling between the degenerate modes can be adjusted by the defected corner cut perturbation. The

drawback of this resonator is that it has a large circuit size. In [10], a dual-mode bandpass filter using slotline resonator and stubs was designed. The resonant frequency of this resonator was reduced about 7% by loading slotline stubs.

Based on our previous work in dual-mode slotline resonator [9, 10], a miniaturized dual-mode BPF using slotline resonator, slot spurlines, and sagittate stubs is proposed in this paper. The type of filter characteristic (Chebyshev or elliptic) can be controlled by the location of the spurlines. However, in references [9, 10], the type of filter characteristic is adjusted by changing the perturbation's size. In this paper, the filter can be miniaturized to a great extent by using the sagittate stubs. The proposed resonator in this work has a larger size reduction compared to the resonators in [9, 10]. The miniaturization technique is discussed in detail. Finally, this filter with elliptic characteristics is designed and fabricated. Measurements and simulations are given.

## 2. Miniaturization Technique

A conventional square resonator consists of four  $\lambda/4$  transmission lines with the same characteristic impedances, and its size is determined by the guided wavelength of the transmission line. It is possible to reduce the physical length of a transmission line by using a  $\pi$  equivalent topology.

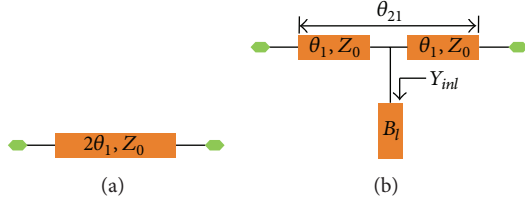


FIGURE 1: (a) Conventional transmission line. (b) The length-reduced transmission line with a reactance part.

Figure 1(a) shows a transmission line with characteristic impedance  $Z_0$  and electrical length  $2\theta_1$ , whereas Figure 1(b) shows a transmission line  $(2\theta_1, Z_0)$  loaded by a stub with reactance  $B_l$ . The admittance of the reactance is marked with  $Y_{inl}$ . To demonstrate size reduction of the transmission line, ABCD matrix is used to analyze equivalent circuit model. The transmission characteristics of the equivalent circuit can be presented by ABCD matrix that normalized to characteristic admittance  $Y_0$ . Let characteristic impedance  $Z_0 = 1/Y_0$  and the normalized admittance  $\bar{Y}_{inl} = Y_{inl}/Y_0$ ; the normalized ABCD matrix is expressed as follows:

$$\begin{aligned} & \begin{bmatrix} A & B \\ C & D \end{bmatrix} \\ &= \begin{bmatrix} \cos \theta_1 & j \sin \theta_1 \\ j \sin \theta_1 & \cos \theta_1 \end{bmatrix} \cdot \begin{bmatrix} 1 & 0 \\ \bar{Y}_{inl} & 1 \end{bmatrix} \cdot \begin{bmatrix} \cos \theta_1 & j \sin \theta_1 \\ j \sin \theta_1 & \cos \theta_1 \end{bmatrix} \\ &= \begin{bmatrix} \cos 2\theta_1 + \left(\frac{j}{2}\right) \cdot \bar{Y}_{inl} \cdot \sin 2\theta_1 & j \sin 2\theta_1 - \bar{Y}_{inl} \cdot \sin^2 \theta_1 \\ j \sin 2\theta_1 + \bar{Y}_{inl} \cdot \cos^2 \theta_1 & \cos 2\theta_1 + \left(\frac{j}{2}\right) \cdot \bar{Y}_{inl} \cdot \sin 2\theta_1 \end{bmatrix}. \end{aligned} \quad (1)$$

Then, the S-parameter of the length-reduced transmission line can be obtained by matrix conversion as follows:

$$S_{21} = \frac{2}{A + B + C + D}. \quad (2)$$

By substituting (1) into (2), we can get

$$|S_{21}| = \left| \frac{2}{2 + \bar{Y}_{inl}} \right|. \quad (3)$$

The total electrical length of the length-reduced transmission line can be obtained by matrix conversion as follows:

$$\theta_{21} = \arctan \left( \frac{\tan 2\theta_1 - (j/2) \cdot \bar{Y}_{inl}}{1 + (j/2) \cdot \bar{Y}_{inl} \cdot \tan 2\theta_1} \right). \quad (4)$$

For getting a real  $\theta_{21}$ ,  $Y_{inl}$  must be a pure imaginary in (4). So, let  $Y_{inl} = jBY_0$  and formula (4) can be simplified as

$$\theta_{21} = 2\theta_1 + \arctan \left( \frac{B}{2} \right). \quad (5)$$

It can be found from (5) that when  $B > 0$  ( $Y_{inl} > 0$ ), the absolute value of the  $\theta_{21}$  is larger than that of  $2\theta_1$ . The

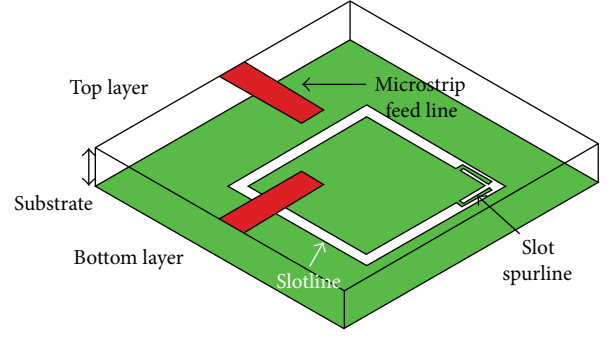


FIGURE 2: Three-dimensional view of a slotline square resonator with a pair of slot spurlines.

fact implies that the physical length of a transmission line can be reduced by a reactance center loaded effectively. Thus, compactness of the structure is achieved.

### 3. Dual-Mode Slot Filter Design

Figure 2 shows the three-dimensional view of a slotline structure. It consists of two layers. On the bottom layer, a full-wavelength ( $\lambda$ ) slot square resonator with a pair slot spurlines is etched on the backside metallic ground plane. On the top layer, there is a pair of microstrip  $50 \Omega$  feed lines.

Using spurlines perturbation to excite the degenerate modes of microstrip square loop resonator is discussed in this paper. A pair of spurlines are located in different corners, the nature of the coupling between the degenerate modes will present inductive (magnetic) or capacitive (electric), and the frequency response characteristic will exhibit a Chebyshev characteristic or an elliptic characteristic, respectively. Just like microstrip square loop resonator, two different dual-mode slotline resonators with slot spurlines are shown in Figures 3(a) and 3(b). The two dual-mode slotline resonators were simulated by *Ansoft HFSS 10* and the results are given in Figure 3(c). When the spurlines are embedded on the corners A and C, seen in Figure 3(b), it exhibits a Chebyshev characteristic. However, when the spurlines are embedded on the corner B, seen in Figure 3(a), it exhibits an elliptic characteristic, as confirmed by our simulations shown in Figure 3(c). The reason is that the slot spurlines perturbation's location can change the nature of the coupling.

Current distributions of the dual-mode resonator are depicted in Figures 4 and 5. Results show that the locations of the higher and the lower density H-field distribution regions of Mode-II ( $f_2$ ) are rotated by 90 degrees from those of Mode-I ( $f_1$ ).

Based on the afore-mentioned analysis, a miniaturized dual-mode slot filter is proposed by using a loaded stub. The three-dimensional view of the miniaturized square resonator is shown in Figure 6. The top view is shown in Figure 7. There is a sagittate stub center loaded on each side of the square slot resonator. The sagittate stub has the advantage of making maximum use of the inner space of the square resonator. Therefore, the sagittate stub can be used to reduce the size of the square resonator to a great extent.

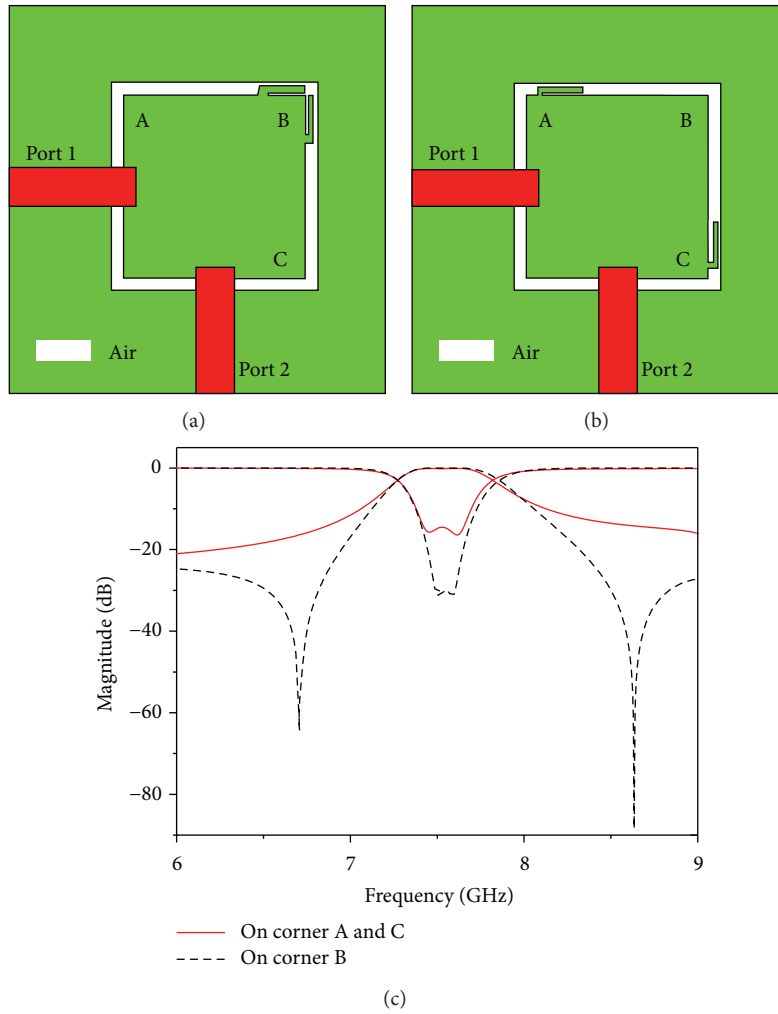


FIGURE 3: (a) Dual-mode square slotline resonator with the slot spurlines on corner B. (b) Dual-mode square slotline resonator with the slot spurlines on corners A and C. (c) Their simulated frequency response, where the black dash line is for (a) and the red line is for (b).

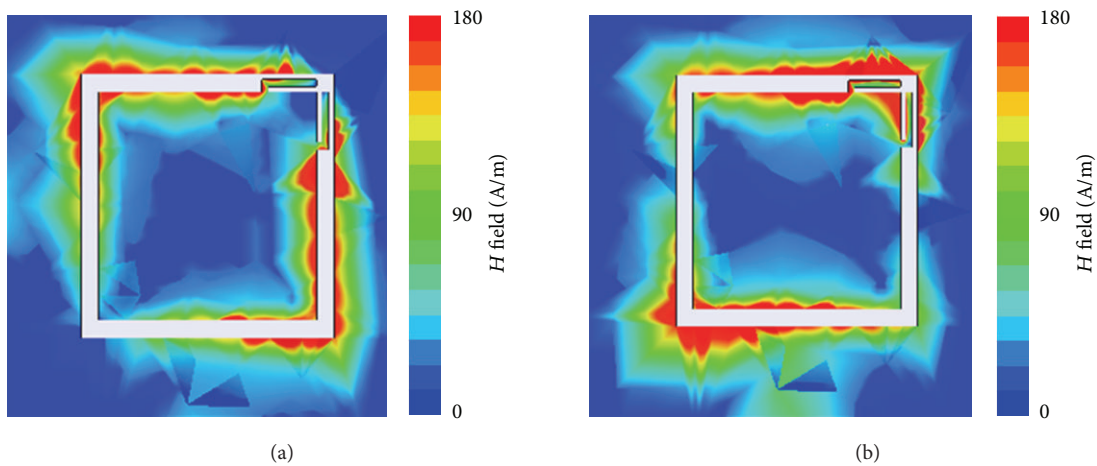


FIGURE 4: Simulated current distributions for two degenerate modes with an elliptic characteristic (spurlines on corner B): (a)  $f_1 = 7.5$  GHz; (b)  $f_2 = 7.59$  GHz.

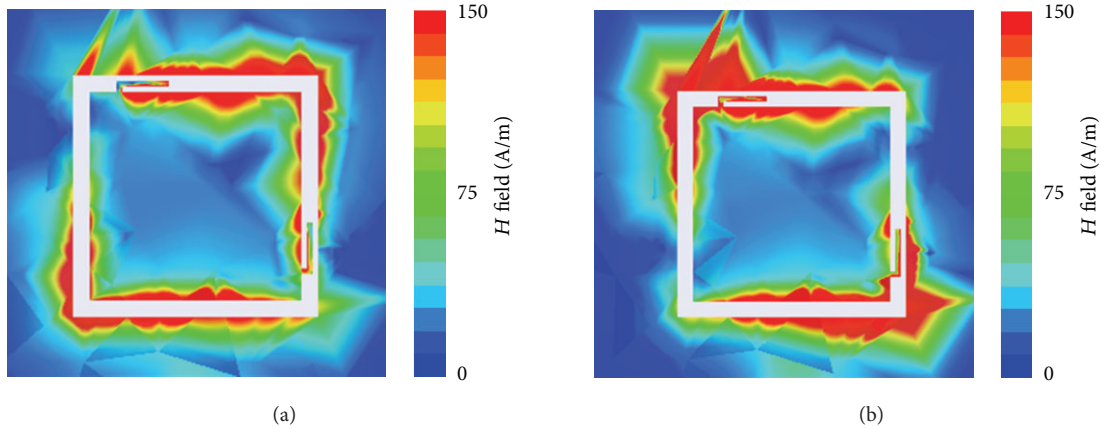


FIGURE 5: Simulated current distributions for two degenerate modes with a Chebyshev characteristic (spurline on corners A and C): (a)  $f_1 = 7.45$  GHz; (b)  $f_2 = 7.63$  GHz.

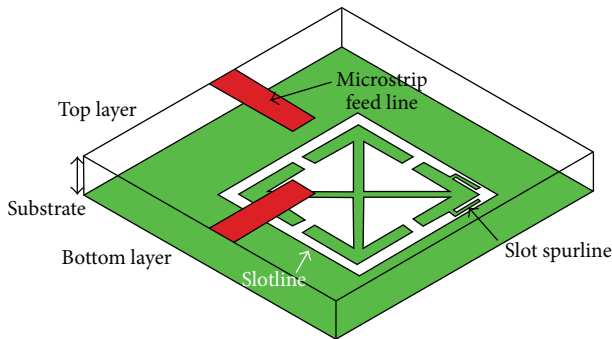


FIGURE 6: The three-dimensional view of the miniaturized square resonator.

#### 4. Measurements

For demonstration purpose, a miniaturized dual-mode BPF operating at 5.75 GHz for WLAN application was designed. The designed filter is designed on a Taconic RF-35A2 substrate with a relative dielectric constant of 3.5, a thickness of 0.76 mm, and a loss tangent of 0.0011. Following the afore-mentioned design method, the dimensions are given as follows:  $w_1 = 0.6$  mm,  $w_2 = 0.2$  mm,  $L_1 = 8.4$  mm,  $L_2 = 0.8$  mm,  $L_3 = 0.3$  mm, and  $L_4 = 2.3$  mm. The overall size of this filter is  $8.4 \times 8.4$  mm<sup>2</sup> (about  $0.175 \lambda_g$  by  $0.175 \lambda_g$ , where  $\lambda_g$  is the guided wavelength at the center frequency of the passband). The size of the conventional resonator at 5.75 GHz is  $12 \times 12$  mm<sup>2</sup>. It means that the proposed resonator has a size reduction of 30% compared to the conventional resonator. The simulated results are illustrated in Figure 10. Current distributions of the miniaturized dual-mode resonator are depicted in Figure 8. The phase difference of the high-density distributions between two degenerate modes is about  $90^\circ$ . This is consistent with the previous analysis.

Figure 9 shows the photographs of the proposed miniaturized dual-mode slot bandpass filter. The measured results are illustrated in Figure 10. Results show that the passband of

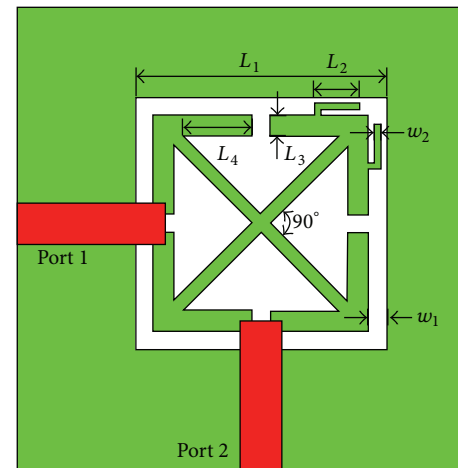


FIGURE 7: Top view of the proposed  $t$  miniaturized dual-mode square filter.

the filter is centered at 5.785 GHz with the fractional bandwidth of 4%. The minimum insertion loss of the measured result is 1.93 dB at the passband. The insertion loss is mainly due to radiation loss of the slotline. In addition, there are two transmission zeros on both sides of the passbands. They are  $-61.2$  dB/ $-78.7$  dB at frequencies of 5.44 GHz/6.56 GHz respectively. They are close to the passband edges and can greatly improve the selectivity and stopband suppression. The transition is usually required to have a flat group delay [11]. Figure 11 illustrates the group delays of the dual-mode filter. The measured result shows that the filter has about 0.45-ns peak-to-peak variation in the group delay. This raised variation is caused by a tradeoff between rejection skirt in  $S_{21}$ -magnitude and linearity in phase [12]. Measured result agrees well with the simulated one and proves the validity of the introduced design principles to produce the dual-mode characteristics.

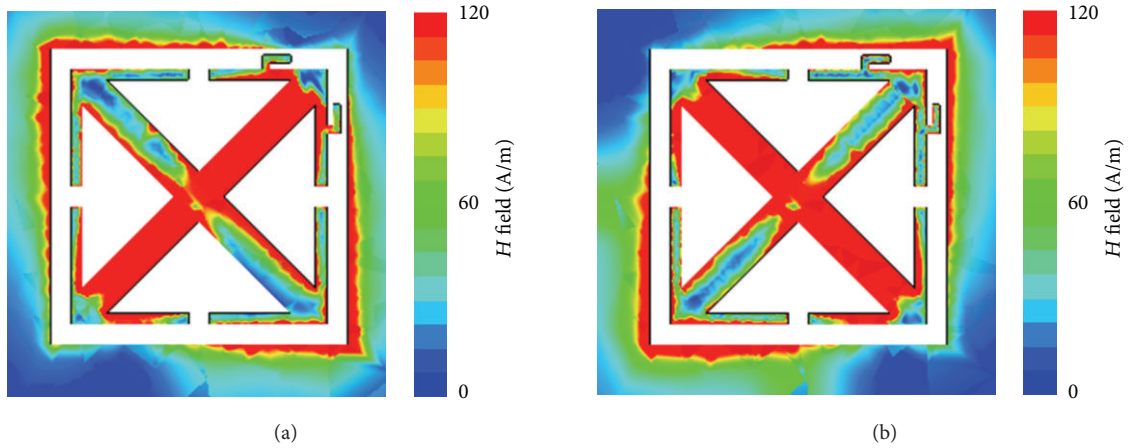


FIGURE 8: Simulated current distributions of the final filter: (a)  $f_1 = 5.77$  GHz; (b)  $f_2 = 5.8$  GHz.

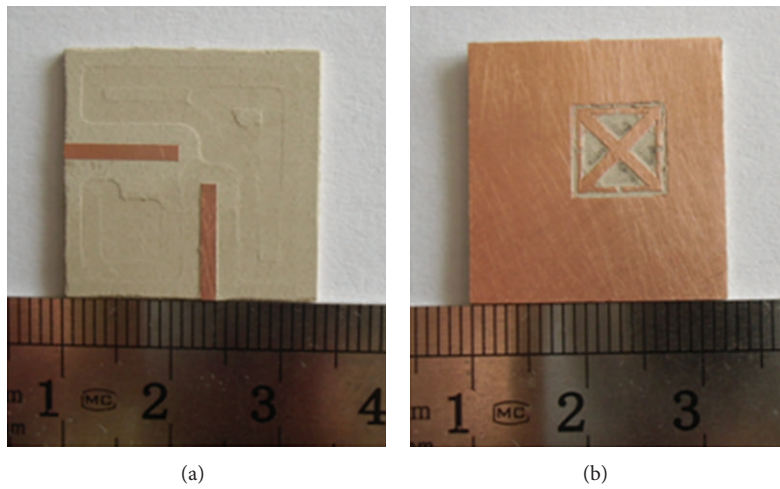


FIGURE 9: Photographs of proposed filter: (a) top view and (b) bottom view.

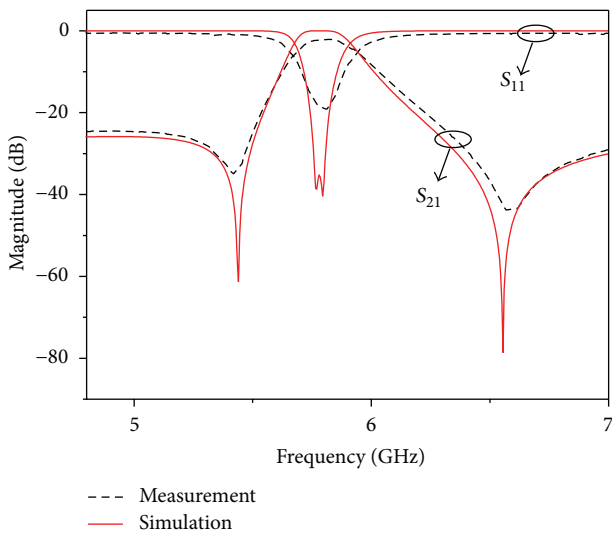


FIGURE 10: Measured and simulated frequency responses of the proposed dual-mode bandpass filter.

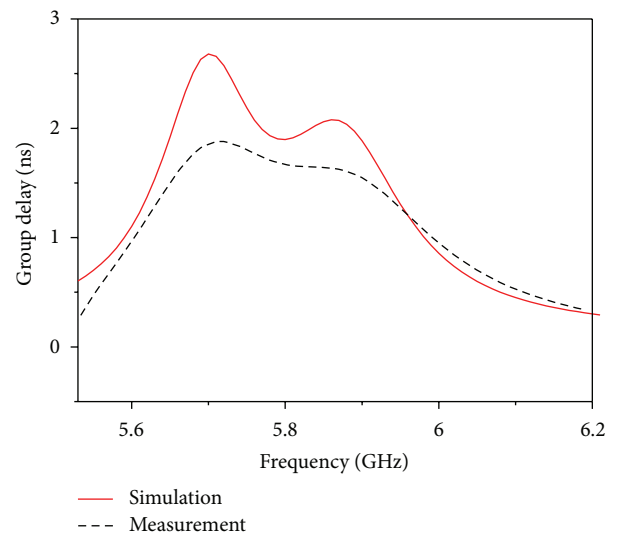


FIGURE 11: Group delay of the proposed miniaturized filter.

## 5. Conclusion

A miniaturized dual-mode slot bandpass filter using slot spurline technique is presented in this paper. The type of filter characteristic (Chebyshev or elliptic) can be controlled by the location of the spurlines. Also, the miniaturization technique is studied. The sagittate stub can make full use of the inner space of the square resonator. Therefore, the filter can be miniaturized to a great extent. A good agreement between the simulated and experimental responses is obtained and demonstrated. The presented compact dual-mode filter is particularly suitable for communication systems.

## Acknowledgments

This work was supported by the National Science Foundation of China (no. 61061001) and International Cooperation Funds and Science and Technology Innovation Team of Jiangxi Province of China (nos. 20121BDH80015 and 20122BCB24025).

## References

- [1] S. Amari, "Application of representation theory to dual-mode microwave bandpass filters," *IEEE Transactions on Microwave Theory and Techniques*, vol. 57, no. 2, pp. 430–441, 2009.
- [2] S. W. Ren, H. L. Peng, J. F. Mao, and A. M. Gao, "Compact quasi-elliptic wideband bandpass filter using cross-coupled multiple-mode resonator," *IEEE Microwave and Wireless Components Letters*, vol. 22, pp. 397–399, 2012.
- [3] A. Görür, "Description of coupling between degenerate modes of a dual-mode microstrip loop resonator using a novel perturbation arrangement and its dual-mode bandpass filter applications," *IEEE Transactions on Microwave Theory and Techniques*, vol. 52, no. 2, pp. 671–677, 2004.
- [4] A. Görür and C. Karpuz, "Miniature dual-mode microstrip filters," *IEEE Microwave and Wireless Components Letters*, vol. 17, no. 1, pp. 37–39, 2007.
- [5] R. Chu, J. F. Mao, and L. Zhou, "A meandering dual-mode bandpass filter with rectangular-loop perturbation," *Microwave and Optical Technology Letters*, vol. 52, no. 10, pp. 2356–2359, 2010.
- [6] S. Fu, B. Wu, J. Chen, S. J. Sun, and C. H. Liang, "Novel second-order dual-mode dual-band filters using capacitance loaded square loop resonator," *IEEE Transactions on Microwave Theory and Techniques*, vol. 60, no. 3, pp. 477–483, 2012.
- [7] W. Feng, K. Deng, W. Che, and S. Dong, "Novel microstrip bandpass filter based on defected ground structure and slotline coupling techniques," *Microwave and Optical Technology Letters*, vol. 52, no. 1, pp. 4–6, 2010.
- [8] Z. Q. Cheng, J. Li, X. G. Mao, S. Tan, and J. K. Chen, "Flip-chip integrated Oscillator with reduced phase noise and enhanced output power by using DGS," *Journal of Infrared and Millimeter Waves*, vol. 27, no. 6, pp. 401–404, 2008.
- [9] H. W. Liu, L. Shen, Z. C. Zhang, J. S. Lim, and D. Ahn, "Dual-mode dual-band bandpass filter using defected ground waveguide," *Electronics Letters*, vol. 46, no. 13, pp. 895–897, 2010.
- [10] H. W. Liu, Y. C. Fan, G. W. Wei et al., "Compact dual-mode bandpass filter using slotline resonator and stubs," *Microwave and Optical Technology Letters*, vol. 54, no. 3, pp. 641–644, 2012.
- [11] A. M. Abbosh, "Multioctave microstrip-to-coplanar waveguide vertical transition," *Microwave and Optical Technology Letters*, vol. 53, no. 1, pp. 187–189, 2011.
- [12] R. Li and L. Zhu, "Compact UWB bandpass filter using stub-loaded multiple-mode resonator," *IEEE Microwave and Wireless Components Letters*, vol. 17, no. 1, pp. 40–42, 2007.

## Research Article

# A Novel Triple-Mode Bandpass Filter Based on a Dual-Mode Defected Ground Structure Resonator and a Microstrip Resonator

Xuehui Guan,<sup>1,2</sup> Ye Yuan,<sup>1</sup> Lan Song,<sup>1</sup> Xiaoyan Wang,<sup>1</sup>  
Jiuhuai Lei,<sup>1</sup> Lei Zhu,<sup>1</sup> and Peng Cai<sup>3</sup>

<sup>1</sup> School of Information Engineering, East China Jiaotong University, Nanchang 330013, China

<sup>2</sup> State Key Laboratory of Millimeter Waves, Southeast University, Nanjing 210096, China

<sup>3</sup> School of Software and Communication Engineering, Jiangxi University of Finance and Economics, Nanchang 330032, China

Correspondence should be addressed to Xuehui Guan; xuehuiguan@yahoo.com.cn

Received 21 February 2013; Accepted 25 March 2013

Academic Editor: Haiwen Liu

Copyright © 2013 Xuehui Guan et al. This is an open access article distributed under the Creative Commons Attribution License, which permits unrestricted use, distribution, and reproduction in any medium, provided the original work is properly cited.

A novel triple-mode bandpass filter (BPF) using a dual-mode defected ground structure (DGS) resonator and a microstrip resonator is proposed in this paper. The dual-mode characteristic is achieved by loading a defected T-shaped stub to a uniform impedance DGS resonator. A uniform impedance microstrip resonator is designed on the top layer of the DGS resonator and a compact bandpass filter with three resonant modes in the passband can be achieved. A coupling scheme for the structure is given and the coupling matrix is synthesized. Based on the structure, a triple-mode BPF with central frequency of 2.57 GHz and equal ripple bandwidth of 15% is designed for the Wireless Local Area Network. Three transmission zeros are achieved at 1.48 GHz, 2.17 GHz, and 4.18 GHz, respectively, which improve the stopband characteristics of the filter. The proposed filter is fabricated and measured. Good agreements between measured results and simulated results verify the proposed structure well.

## 1. Introduction

Recent decades have seen the rapid development of wireless technology; as a result, there is an increasing demand on high performance microwave filters [1]. The appearance of dual-mode resonators has found its way into the application of filters and gained increasing popularity among the microwave filters for their capability to make a reduction of the numbers of resonating components. Since a microstrip ring dual-mode bandpass filter (BPF) was firstly proposed by Wolff in 1972 [2], various forms of dual-mode microstrip resonators and filters have been reported, including square patch resonators [3], square loop resonators [4], triangular loop resonators [5], and hexagonal loop resonators [6]. Degenerate modes are excited by the perturbations within dual-mode resonators. Dual-mode or triple-mode characteristics can also be achieved

by loading a stub to a resonator [7]. When changing the size of loading stub, the even-mode resonant frequencies can be easily controlled whereas the odd-mode resonant frequencies keep almost unchanged. Recently, microwave circuits are popularly designed on the ground plane [8–10], such as slotline with defected ground structure (DGS) stubs [11], defected resonator [12], and defected stepped impedance resonator [13]. It provides a novel way for realizing dual-mode filters and multimode filters by fully utilizing the printed circuit board. Multimode filters can also be realized by using dual-mode resonator doublets [14]. In our previous work [15], a four-mode BPF is achieved by combination of two dual-mode microstrip resonators. By setting two stub-loaded dual-mode resonators in parallel, a BPF with four poles is realized. However, the resonators could be properly arranged to minimize the circuit size.

In this paper, a novel triple-mode bandpass filter is proposed using a dual-mode defected structure resonator and a microstrip resonator. A coupling scheme for the filter is given and the coupling matrix is synthesized. The ideal response of the filter agrees well with the simulated results. Compared with traditional filter of the same characteristic, the size of proposed filter reduces approximately 2/3. Three transmission zeros are achieved at 1.48 GHz, 2.17 GHz, and 4.18 GHz in the stopband of the filter, which greatly improve the selectivity and rejection of the filter. The proposed BPF is simulated, implemented, and measured. Good agreement is observed between simulated results and measured results.

## 2. Theoretical Analysis

**2.1. Analysis of Filter Structure.** Figure 1 is the 3D structure of the proposed triple-mode filter. The filter structure can be divided into three layers: the top layer is covered with a microstrip open-loop resonator and a pair of microstrip feed lines, the middle layer is the substrate, and the bottom layer is metal ground that is loaded by a dual-mode DGS resonator. The microstrip resonator on the top layer and the DGS resonator in the bottom layer are both directly coupled to the microstrip feed lines. Since the microstrip resonator and the DGS resonator are located on different layer of the circuit, the space of the circuit is fully utilized and the size of filter is reduced.

The coupling scheme of the triple-mode filter is presented in Figure 2. The dark circles and the white circles indicate resonant modes of resonators and source/load, respectively. Mode 1 is generated by the microstrip resonator; modes 2 and 3 are even and odd modes of the dual-mode DGS resonator [16]. These modes are all directly coupled to both the source and the load. The coupling between microstrip resonator and source/load can be modified by changing their distance and overlap length. The coupling between dual-mode resonator and source/load also can be tuned by changing the location of the resonator. Commonly, the coupling between the microstrip resonator and source or load and the coupling between the even mode of the dual-mode DGS resonator and input or output are all positive. The coupling between the odd mode of the dual-mode DGS resonator and source is positive, while the coupling between this mode and load is negative. The dashed line indicates the coupling between source and load that is determined by the gap between input and output microstrip line. Therefore, the corresponding coupling matrix of the coupling scheme is given by

$$M = \begin{bmatrix} 0 & M_{S1} & M_{S2} & M_{S3} & M_{SL} \\ M_{1S} & M_{11} & 0 & 0 & M_{1L} \\ M_{2S} & 0 & M_{22} & 0 & M_{2L} \\ M_{3S} & 0 & 0 & M_{33} & M_{3L} \\ M_{LS} & M_{L1} & M_{L2} & M_{L3} & 0 \end{bmatrix}. \quad (1)$$

Due to symmetrical geometry of the proposed filter, the coupling coefficients agree with  $M_{S1} = M_{L1}$ ,  $M_{S2} = M_{L2}$ , and  $M_{S3} = -M_{L3}$ . A transmission zero is produced by the coupling between source and load which improve the

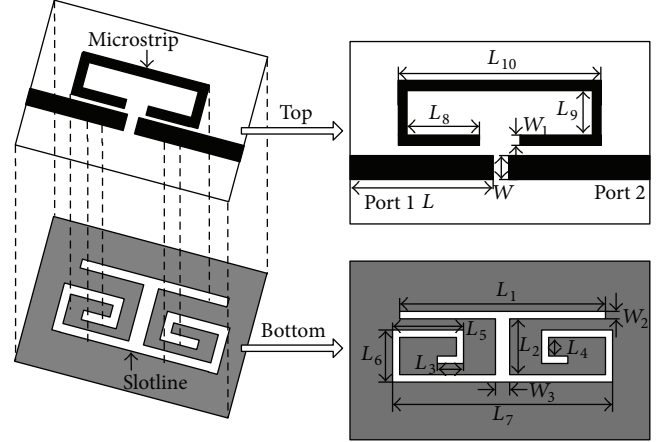


FIGURE 1: Configuration of slotline-microstrip triple-mode BPF.

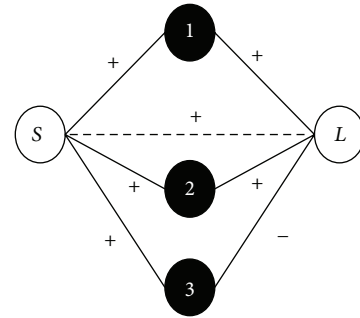


FIGURE 2: The coupling scheme of proposed triple-mode BPF.

selectivity of the proposed BPF. Therefore, the generalized coupling matrix for the proposed BPF with central frequency of 2.57 GHz can be obtained on the basis of the approach of synthesis in [17] as follows:

$$M = \begin{bmatrix} 0 & 0.6369 & 0.3645 & 0.7824 & 0.0282 \\ 0.6369 & -1.5130 & 0 & 0 & 0.6369 \\ 0.3645 & 0 & 1.3070 & 0 & 0.3645 \\ 0.7824 & 0 & 0 & 0.5266 & -0.7824 \\ 0.0282 & 0.6369 & 0.3645 & -0.7824 & 0 \end{bmatrix}. \quad (2)$$

The synthesized scattering characteristic of the proposed filter is shown in Figure 3. The solid line and the dashed line indicate insertion loss and return loss, respectively. Three transmission poles are clearly observed in the passband of the filter. In addition, three transmission zeros are created at 1.41 GHz, 2.17 GHz, and 4.18 GHz, which improve the selectivity in the transition band and attenuation in the stopband. The return loss in the passband is larger than 20 dB and the minimum insertion loss in the stopband is almost greater than 20 dB.

**2.2. Analysis of Transmission Zeros.** Figure 4 shows the transmission characteristics of the filter versus the length of microstrip feed line. When the length of microstrip feed line

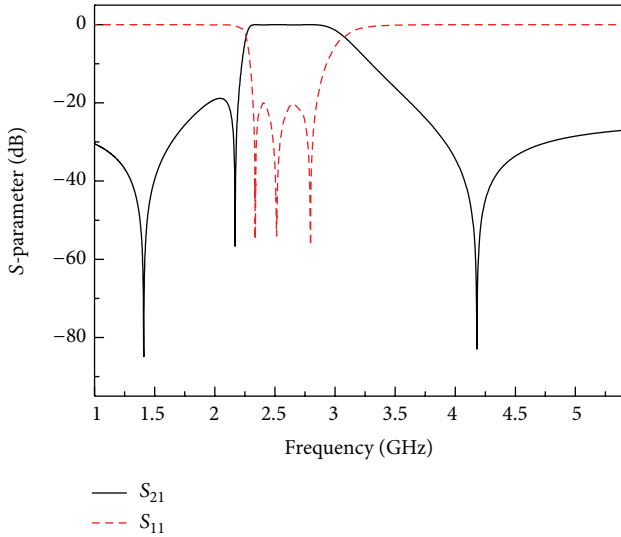


FIGURE 3: Synthesized theory result of triple-mode BPF.

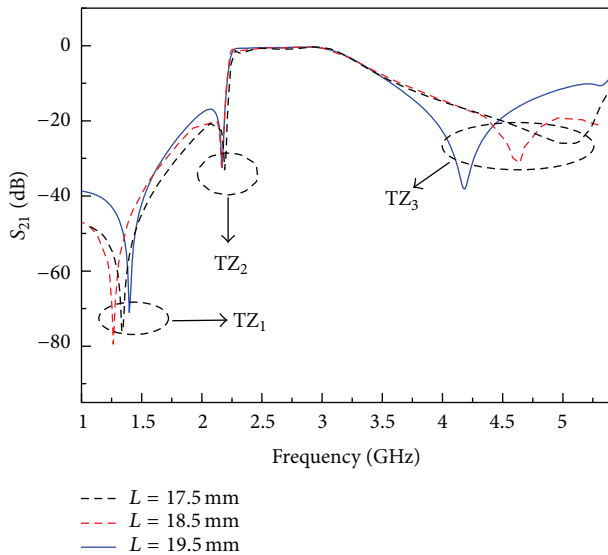


FIGURE 4: The changes of transmission zeros versus  $L$ .

$L$  increases, that is, the coupling gap between input line and output line decreases, the coupling between source and load increases accordingly. Consequently, the third transmission zero ( $TZ_3$ ) moves towards the passband, whereas the other two transmission zeros almost remain unchanged. Thus, it turns out to be convenient to realize filters with sharp transition band. Simultaneously, increment of the length of microstrip feed line may increase the coupling between source/load and resonators, and the transmission zero ( $TZ_1$ ) will shift to the passband.

To study the influence of the microstrip resonator on the characteristic of the filter, frequency responses of triple-mode BPF and dual-mode resonator are compared in Figure 5. The dotted curve indicates the transmission characteristic of DGS dual-mode resonator and the solid line indicates the transmission characteristic of proposed structure. It is

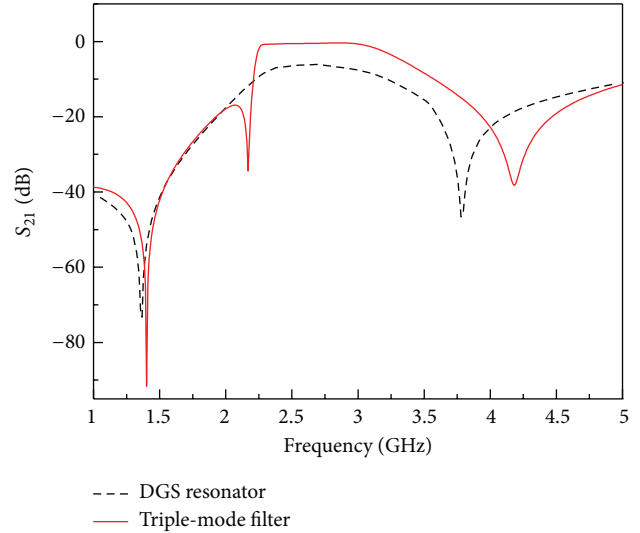


FIGURE 5: The comparison of frequency responses between triple-mode BPF and dual-mode resonator.

clearly observed that an additional transmission zero is created at about 2.17 GHz when the microstrip open-loop resonator is loaded. The phenomenon can be explained by the fact that the microstrip open-loop resonator adds an extra transmission path to the circuit, and it will counteract with signal from another path at certain frequency. In addition, the first transmission zero  $TZ_1$  almost keeps stable and the transmission zero in the upper stopband of the filter shifts away from the pass band, when the microstrip open-loop resonator is added to the circuit.

Figure 6 gives the simulated transmission characteristics of the filter versus  $L_8$ . When  $L_8$  increases from 4.5 mm to 5.5 mm,  $TZ_2$  moves towards lower frequency and  $TZ_3$  shifts to higher frequency, while  $TZ_1$  seems to keep unchanged. When  $L_8$  increases from 5.5 mm to 6.5 mm, three transmission zeros shift accordingly. It is obvious that the bandwidth of the filter will enlarge with the increment of  $L_8$ . Changing  $L_8$  will modify the overlapping length between feed line and microstrip resonator, and the coupling between source/load and microstrip resonator will vary accordingly. Moreover, resonant frequency of the microstrip resonator will change with  $L_8$ , so that  $L_8$  influences not only the bandwidth of the filter but also the location of the transmission zeros.

### 3. Simulation and Experimental Results

For the sake of validating above-mentioned theory, a compact and high selectivity triple-mode BPF is designed and fabricated. The designed filter has a central frequency of 2.57 GHz and fractional bandwidth of 15% with equal ripple of 0.0432 dB. A substrate with a relative dielectric constant of 3.5 and a thickness of 0.8 mm is used in the design. Obtained parameters of the filter shown in Figure 1 are as follows:  $L = 19.5$  mm,  $L_1 = 15$  mm,  $L_2 = 3$  mm,  $L_3 = 1.8$  mm,  $L_4 = 1$  mm,  $L_5 = 5.5$  mm,  $L_6 = 3$  mm,  $L_7 = 16$  mm,

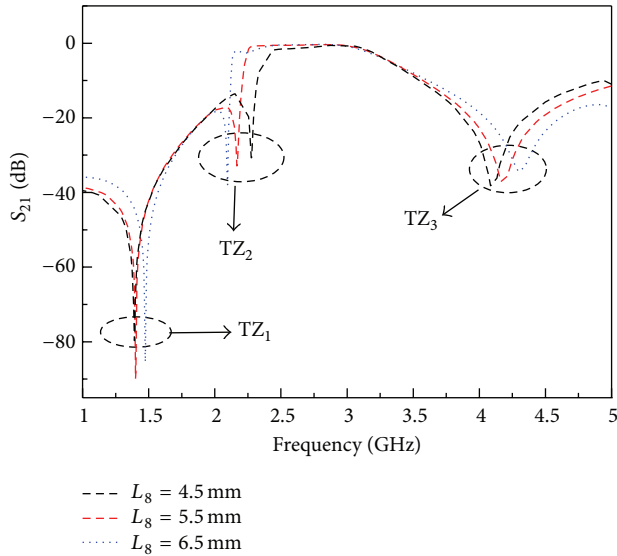


FIGURE 6: Transmission characteristics of the filter versus  $L_8$ .

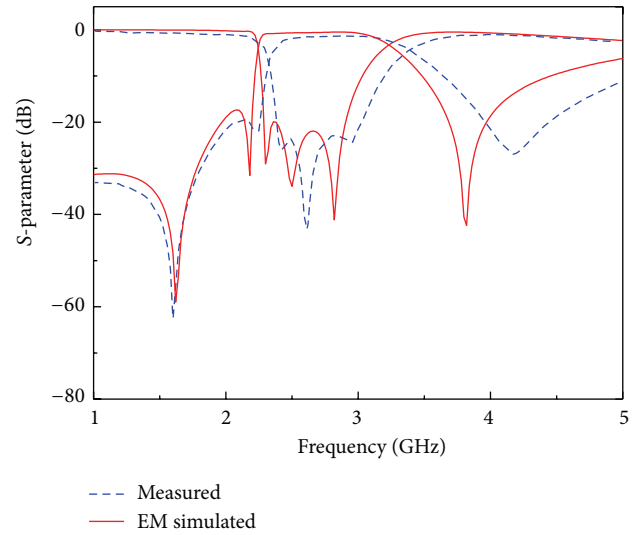
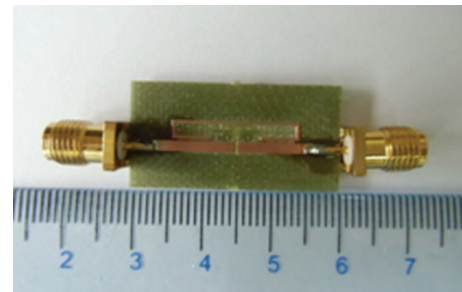


FIGURE 7: Comparison between EM simulated and measured results of the proposed filter.

$L_8 = 5.5$  mm,  $L_9 = 2.6$  mm,  $L_{10} = 18$  mm,  $W = 1.5$  mm,  $W_1 = 0.5$  mm,  $W_2 = 0.5$  mm, and  $W_3 = 1$  mm. The filtering performance is measured by using Network Analyzer AV3926, and a comparison between EM simulated results and measured results is shown in Figure 7. Solid lines and dotted lines indicate the simulated and measured results, respectively. The passband of the proposed filter is from 2.2 GHz to 3.68 GHz, and its passband return loss is larger than 20 dB. Three transmission poles are clearly observed at 2.31 GHz, 2.5 GHz, and 2.82 GHz in the passband of the filter. Three transmission zeros are generated at 1.48 GHz, 2.17 GHz, and 4.18 GHz, which improve the selectivity of the filter. The simulated and measured maximum insertion loss in the passband are 1 dB and 1.12 dB, respectively. Apart from the frequency shift that may be caused by the discrepancy of the dielectric constant between its nominal value and real value, measured results agree well with the simulated results. The photograph of the fabricated filter is shown in Figure 8. The designed filter circuit occupies the overall size of about 30 mm  $\times$  15 mm.

#### 4. Conclusion

A novel miniature microstrip triple-mode bandpass filter is proposed in this paper. Three modes are obtained by combination of a dual-mode DGS resonator and a microstrip resonator. The coupling matrix of proposed structure is established to further explain the proposed design. Three transmission zeros are realized in the stopband of the filter, which greatly improve the selectivity and attenuation of proposed filter. Measured results agree well with the simulated results, verifying the proposed structure and design methodology.



(a)



(b)

FIGURE 8: Photographs of the fabricated filter: (a) top view and (b) bottom view.

#### Acknowledgments

This work is supported by National Science Foundation Committee of China (no. 61061001, no. 61161005), Open Fund from State Key Laboratory of Millimeter Wave (K201210), Training Program for Young Scientists of Jiangxi Province, and Natural Science Foundation of Jiangxi Province (20114BAB211011).

## References

- [1] S. W. Ren, H. L. Peng, J. F. Mao, and A. M. Gao, "Compact quasi-elliptic wideband bandpass filter using cross-coupled multiple-mode resonator," *IEEE Microwave and Wireless Components Letters*, vol. 22, no. 8, pp. 397–399, 2012.
- [2] I. T. H. Wolff, "Microstrip bandpass filter using degenerate modes of a microstrip ring resonator," *Electronics Letters*, vol. 8, no. 12, pp. 302–303, 1972.
- [3] L. Zhu, P. M. Wecowski, and K. Wu, "New planar dual-mode filter using cross-slotted patch resonator for simultaneous size and loss reduction," *IEEE Transactions on Microwave Theory and Techniques*, vol. 47, no. 5, pp. 650–654, 1999.
- [4] J. S. Hong and M. J. Lancaster, "Bandpass characteristics of new dual-mode microstrip square loop resonators," *Electronics Letters*, vol. 31, no. 11, pp. 891–892, 1995.
- [5] R. Wu and S. Amari, "New triangular microstrip loop resonators for bandpass dual-mode filter applications," in *Proceedings of the IEEE MTT-S International Microwave Symposium*, pp. 941–944, June 2005.
- [6] R. J. Mao and X. H. Tang, "Novel dual-mode bandpass filters using hexagonal loop resonators," *IEEE Transactions on Microwave Theory and Techniques*, vol. 54, no. 9, pp. 3526–3533, 2006.
- [7] J. S. Hong and H. Shaman, "Dual-mode microstrip open-loop resonators and filters," *IEEE Transactions on Microwave Theory and Techniques*, vol. 55, no. 8, pp. 2099–2109, 1996.
- [8] Z. Q. Cheng, J. Li, X. G. Mao, S. Tan, and J. K. Chen, "Flip-chip integrated oscillator with reduced phase noise and enhanced output power by using DGS," *Journal of Infrared and Millimeter Waves*, vol. 27, no. 6, pp. 401–404, 2008.
- [9] A. Boutejdar, A. El-Sherbini, and A. S. Omar, "Method for widening the reject-band in lowpass/bandpass filters by employing coupled C-shaped defected ground structure (DGS)," *IET Microwaves, Antennas & Propagation*, vol. 17, no. 12, pp. 1405–1408, 2008.
- [10] A. Boutejdar, A. Elsherbini, A. Balalem, J. Machac, and A. S. Omar, "Design of new DGS hairpin microstrip bandpass filter using coupling matrix method," in *Progress in Electromagnetics Research Symposium*, pp. 261–265, Prague, Czech Republic, 2007.
- [11] W. Feng, K. Deng, W. Che, and S. Dong, "Novel microstrip bandpass filter based on defected ground structure and slotline coupling techniques," *Microwave and Optical Technology Letters*, vol. 52, no. 1, pp. 4–6, 2010.
- [12] A. Mohan and A. Biswas, "Dual-band bandpass filter using defected ground structure," *Microwave and Optical Technology Letters*, vol. 51, no. 2, pp. 475–479, 2009.
- [13] B. Wu, C. H. Liang, P. Y. Qin, and Q. Li, "Compact dual-band filter using defected stepped impedance resonator," *IEEE Microwave and Wireless Components Letters*, vol. 18, no. 10, pp. 674–676, 2008.
- [14] Z. Ma, W. He, C. P. Chen, Y. Kobayashi, and T. Anada, "A novel compact ultra-wideband bandpass filter using microstrip stub-loaded dual-mode resonator doublets," in *Proceedings of the IEEE MTT-S International Microwave Symposium Digest (MTT '08)*, pp. 435–438, Atlanta, Ga, USA, June 2008.
- [15] X. Guan, X. Wang, B. Wang, Y. Yuan, and H. W. Liu, "Design and implementation of compact hybrid four-mode bandpass filter with multi-transmission zeros," *Progress in Electromagnetics Research Letters*, vol. 34, pp. 65–74, 2012.
- [16] X. Guan, W. Fu, H.-W. Liu, D. Ahn, and J.-S. Lim, "A novel dual-mode bandpass filter based on a defected waveguide resonator," *ETRI Journal*, vol. 33, no. 6, pp. 953–956, 2011.
- [17] S. Amari, U. Rosenberg, and J. Bornemann, "Adaptive synthesis and design of resonator filters with source/load-multiresonator coupling," *IEEE Transactions on Microwave Theory and Techniques*, vol. 50, no. 8, pp. 1969–1978, 2002.

## Review Article

# Overview on Multipattern and Multipolarization Antennas for Aerospace and Terrestrial Applications

Aixin Chen,<sup>1</sup> Weiwei Jiang,<sup>1</sup> Zhizhang Chen,<sup>2</sup> and Jiaheng Wang<sup>1</sup>

<sup>1</sup> School of Electronic and Information Engineering, Beihang University, Beijing 100191, China

<sup>2</sup> Department of Electrical and Computer Engineering, Dalhousie University, Halifax, NS, Canada B3J 2X4

Correspondence should be addressed to Aixin Chen; [axchen@buaa.edu.cn](mailto:axchen@buaa.edu.cn)

Received 17 February 2013; Accepted 12 March 2013

Academic Editor: Haiwen Liu

Copyright © 2013 Aixin Chen et al. This is an open access article distributed under the Creative Commons Attribution License, which permits unrestricted use, distribution, and reproduction in any medium, provided the original work is properly cited.

In recent years, reconfigurable antennas, with the ability to radiate wave in more than one pattern and polarization, play a great role in modern telecommunication systems. Compared with conventional antennas, multipattern and multipolarization antennas have more advantages and better prospects. They can be used to improve system gain and security, satisfy system requirements, avoid noisy environment, and adapt to the environment flexibly. This paper discusses different patterns and polarizations of reconfigurable antennas according to current research work in this area. In the opinion of this paper, the radiation pattern states of antennas include beam direction, shape, and gain. The polarization states of antennas include horizontal/vertical linear,  $\pm$ slant  $45^\circ$  linear, left-hand or right-hand circular polarized. Different multipattern and multipolarization antennas with various structures and working mechanisms are compared and discussed. Multipattern and multipolarization antennas have been well applied for aerospace and terrestrial applications, such as dynamic scenarios, adaptive beam scanning, and multiple-input-multiple-output (MIMO) systems.

## 1. Introduction

Generally, as we know, the conventional antennas only can work in one radiation pattern and polarization. When the environmental conditions or system requirements change, we need to reconfigure an antenna. It is inconvenient and costs too much. Reconfigurable antennas are a solution to solve this problem. They can change their radiation pattern and polarization timely to address complex system requirements by modifying their geometry and electrical behavior. Reconfigurable antennas can either increase the capabilities of wireless integrated information systems, expand their functionality, or widen their bandwidths, with efficient spectrum and power utilization.

Compared to today's radio technology which depends on incompatible communication systems with inflexible hardware, the technology of reconfigurability will significantly reduce the hardware complexity, the number of components, and the cost. As described above, reconfigurable antennas promise to bring a host of benefits to future generation of wireless systems. Next-generation communication systems

will rely upon reconfigurable antennas, such as wireless systems in dynamic scenarios (e.g., satellite/terminal tracking), adaptive beam scanning (e.g., radar/remote sensing), and MIMO systems (e.g., active management of channel correlation/diversity/interference). Among diversity of schemes at antenna level, multipattern and multipolarization antennas are important ones. They can be used to improve system gain and security, satisfy system requirement, avoid noisy environment, and adapt to the environment flexibly.

The concept of reconfigurable antenna was first presented in 1983 [1] and further investigation and realization were carried out and results were reported in [2]. In the recent years, reconfigurable antennas attracted more and more attention due to their capability of providing multipattern and multipolarization. One of the important applications is in aerospace and terrestrial wireless communication systems.

In the following sections, the classification of the multipattern and multipolarization antennas, the comparison between the different antennas with various structures and working mechanisms, the field of their application, and the vision and goal are to be discussed.

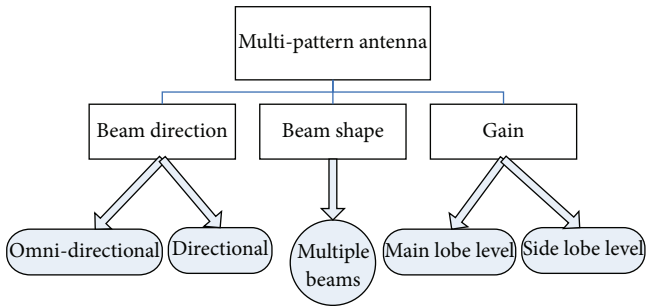


FIGURE 1: Classification of multipattern antennas.

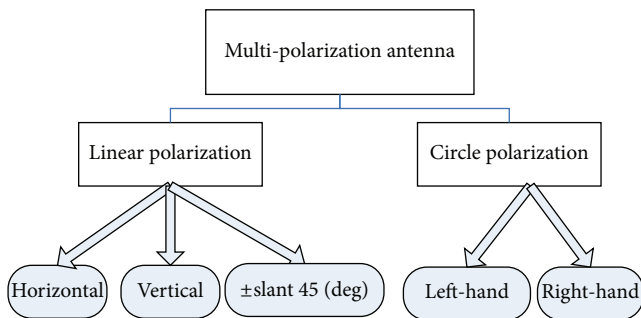


FIGURE 2: Classification of multipolarization antennas.

## 2. Classification and Technologies of Reconfigurable Antennas

In this paper, the reconfigurable antennas (mainly multipattern and multipolarization antennas here) can be classified into three categories: multipattern antennas, multipolarization antennas, and multipattern-multipolarization mixed reconfigurable antennas.

The multipattern antennas are divided into three major types achieved by changing the beam direction, beam shape, and gain, as indicated in Figure 1. The beam direction includes the omnidirectional and directional direction. Antennas which alter between omni-directional and directional radiation patterns [3–8] or vary the direction from one side to another side [9–17] are called the beam direction reconfigurable antennas. Beam shape reconfigurable antennas can be achieved by changing the number of beams (multiple beams) [18–21]. Finally, the gain reconfigurable antennas are able to be realized by changing the shape of beam's main lobe and side lobe [22–24].

The multipolarization antennas include linearly polarized antennas and circularly polarized antennas, as shown in Figure 2. A radiating structure that is able to change its polarization (horizontal, vertical, and radiations, and  $\pm$ slant  $45^\circ$ ) is called linear polarization reconfigurable antennas [25–30]. Circular polarization reconfigurable antennas are achieved by varying polarization between left-hand circular and right-hand circular [31–39]. The antennas switching between the linear polarization and circular polarization are mixed polarization reconfigurable antennas [40–51].

The multipattern-multipolarization mixed reconfigurable antennas are the antennas which combine multipattern with multipolarization [52–61].

In order to realize various reconfigurable antennas, five major technologies are introduced.

- (i) Electronically tuned reactance: alter the capacitors or inductors by varying the bias voltage. The common elements are varactor diodes and microelectromechanical-system- (MEM-S) tunable capacitors/inductors.
- (ii) Radio frequency (RF) electrical switches: by controlling the voltage, achieve the switches to be “on” state or the “off” state. PIN diodes, field effect transistor (FET) switches, and MEMS are popularly used.
- (iii) Photoconductive switches: activate the semiconductor material (silicon, gallium arsenide) by controlling the laser light to realize the “on” state or the “off” state. It results in exciting electrons from the valence to the conduction band and thus creates a conductive connection.
- (iv) Exotic materials: a static applied electric/magnetic field or voltage can change the relative material permittivity/permeability. The smart materials which are used in the substrate of the reconfigurable antennas include nematic liquid crystals, nonlinear materials, and ferroelectric films.
- (v) Structural alteration: by altering the height, acreage, and shape of antenna, the physical structural is able to be modified. The altering structure is the antenna radiating parts.

The multipattern and multipolarization antennas are designed by implying the five major technologies to change surface current distribution, and the feeding network, the physical structure, the effective radiating aperture of antennas. The different patterns or polarizations correspond to different states caused by the technologies.

## 3. Multipattern Antennas

*3.1. Beam Direction Reconfigurable Antennas.* The conventional antennas can only work in the omni-directional or directional beam direction. The beam of omni-directional antenna homogeneously directs all the direction. The beam of directional antenna only directs in some range, but its radiated effect is better than that the omni-directional antenna. Consequently, we can choose the suitable type to meet the need of communication system. For example, in the case that the wireless access points distribute in different places and are close to the antenna, we should choose the omni-directional antenna. On the contrary that the wireless access points are put together in one direction and long away from the antenna, the directional antenna is our choice. So we can see that the reconfigurable antenna with either omni-directional or directional radiation pattern is very useful in wireless system. In addition, when the target is unique and always moves, for example, in the radar and terminal

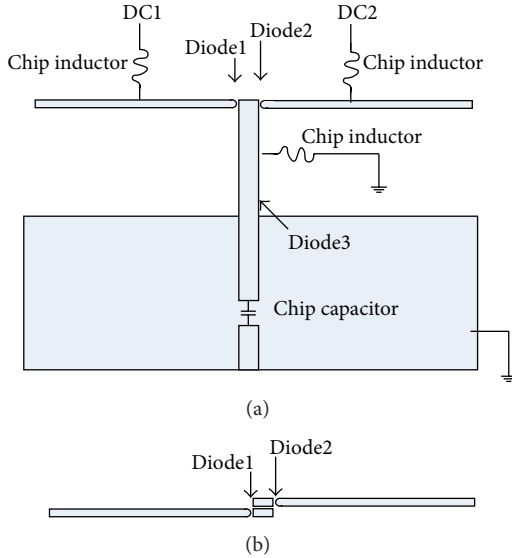


FIGURE 3: Radiation pattern reconfigurable antenna. (a) Side view. (b) Top view (redrawn after).

tracking system, the beam direction of antenna should change at the same time. The directional reconfigurable antenna fits it well. Next, three different examples of beam direction of reconfigurable antennas are described.

**3.1.1. Beam Direction Reconfigurable Antennas with Omnidirectional and Directional Characteristics.** This type of antennas can realize omni-directional and directional radiation. The antenna shown in Figure 3 is a simple radiation pattern reconfigurable antenna. The antenna is a combination of a monopole antenna and a dipole antenna with reflector [3]. Three switches are inserted to control the radiation pattern of antenna. The reconfigurable antenna can be operated as either a monopole antenna with an omnidirectional radiation pattern at the switches “on” state or a dipole antenna with reflector, which has directional radiation pattern at the switches “off” state. The antenna is compact and easy to control.

**3.1.2. Beam Direction Reconfigurable Antennas with Varied Directional Characteristics.** This is a type of complex radiation pattern reconfigurable antennas. A reconfigurable leaky-wave antenna capable of steering its radiation beam over a wide range is discussed in [9]. The antenna system is a microstrip composite right/left-hand (CRLH) leaky-wave antenna composed by 25 cascaded metamaterial unit cells, as shown in Figure 4. To achieve the CRLH behavior, insert an artificial series capacitance and a shunt inductance into a conventional microstrip line by means of an interdigital capacitor and a shorted stub, respectively. By tuning the bias voltage of varactor diodes  $D_S$  and  $D_{SH}$  separately, we can steer the radiation beam from  $-55^\circ$  to  $50^\circ$ .

The fabricated antenna shown in Figure 5(a) is a planar  $6 \times 6$  fully reconfigurable array operating at 5.7 GHz, capable of functioning both as a reconfigurable array lens and

a reconfigurable reflectarray [10]. The array element consists of two varactor diode-loaded patches coupled by a varactor diode-loaded slot, as shown in Figure 5(b). In the lens mode, the antenna has a broadside directivity of 20.8 dBi and a beam-scanning range of  $50^\circ$  by  $50^\circ$ . The array as a reflectarray can achieve a directivity of 19.4 dBi at broadside and a beam-scanning range of  $60^\circ$  by  $30^\circ$ . This array is able to demonstrate full 2D beamforming with low cost and is easy to fabricate.

**3.2. Beam Shape Reconfigurable Antennas.** The antennas which radiate multiple beams at the same time are called multibeam antennas. Multibeam antennas are able to both transmit signal in multiple directions at the same time with high gain and achieve the low side lobe by controlling the amplitude and phase of the feeds. To meet the different demand of communication system, we can change the number and shape of beams. Beam shape reconfigurable antennas are important and have been studied by many scientists.

A multifunctional reconfigurable antenna (MRA) capable of steering its radiation beam in the azimuth plane into one of 4 and 8 directions with variable beamwidth is presented in [20] (see Figure 6). The antenna is composed of a planar array of electrically small metallic square-shaped pixels which are interconnected by MEMS switches. By activating or deactivating the interconnecting MEMS switches, the geometry of the MRA dipole is changed. The antenna with optimum performance is able to apply for a wireless communication system.

**3.3. Gain Reconfigurable Antennas.** The beam makes up by main lobe and side lobe. In general, to improve the gain of antenna, we should increase the mainlobe level and lower the side lobe level as far as possible.

A flexible microstrip patch antenna incorporates a novel multilayer construction consisting of a liquid metal (eutectic gallium indium) encased in an elastomer [24]. The antenna is flexible and durable as its combined properties of the fluid and the elastomeric substrate, as shown in Figure 7(a). Injecting the metal into micro-fluidic channels provides a simple way to define the shape of the liquid, which is stabilized mechanically by a thin oxide skin that forms spontaneously on its surface. In Figure 7(b), a multilayer patch antenna is fabricated using specially designed serpentine channels that take advantage of the unique rheological property of the liquid metal alloy. And in Figure 7(c), by controlling the shape of antenna static, curving a low dielectric mandrel with a radius of 12.7 mm, and curving around a similar mandrel with a radius of 25.4 cm, separately, the antenna can realize three different values of gain. The flexibility antenna is well suited for conformal antenna applications.

## 4. Multipolarization Antennas

Comparing with classical antennas with single polarization, the multipolarization antennas offer advantages of reduction in installation space, low coupling effect, and low installation cost. Their intrinsic polarization diversity advantage is very useful in mitigating the multipath fading and increasing the

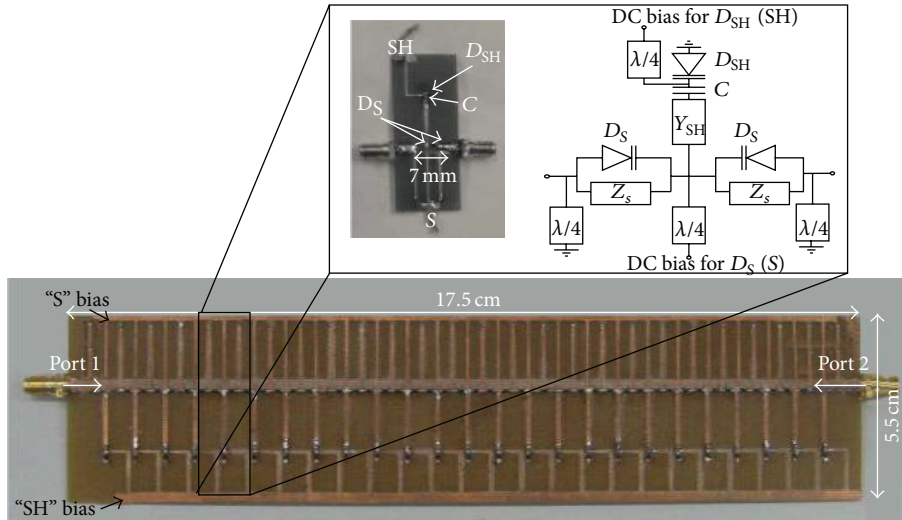
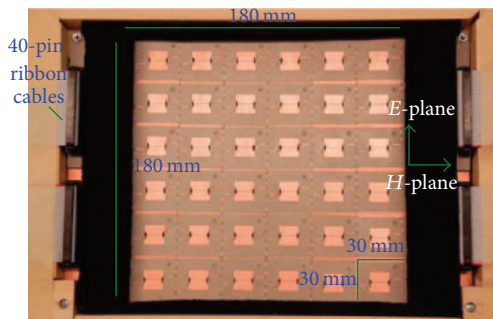
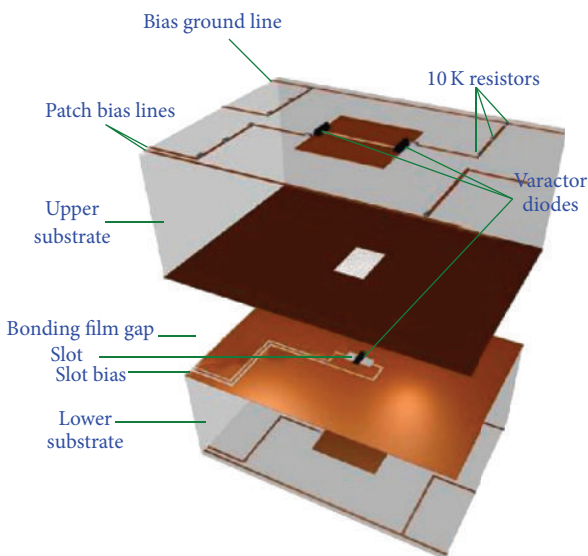


FIGURE 4: Two-port reconfigurable leaky-wave antenna and its tunable unit cell design (with permission from IEEE).



(a)



(b)

FIGURE 5: (a) Fabricated  $6 \times 6$  planar reconfigurable array. (b) Array element and bias network design (vertically exaggerated) (with permission from IEEE).

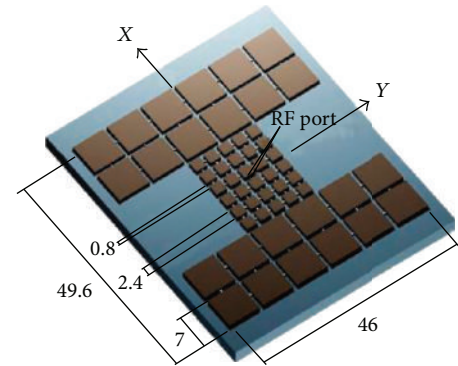


FIGURE 6: Multifunctional reconfigurable antenna (with permission from IEEE).

channel capacity, especially in polarization-varied environment. Such antennas can switch between linear polarization (LP) and circle polarization (CP), depending on the system requirements. The kinds of linear polarization include horizontal, vertical, and  $\pm$ slant  $45^\circ$  polarization. The types of circular polarization are right-hand circular polarization (RHCP) and left-hand circular polarization (LHCP). In this section, three different polarization reconfigurable antennas to adjust the different propagation environment are presented as examples.

**4.1. Linear Polarization Reconfigurable Antennas.** A polarization reconfigurable slot antenna with compact feed is presented in [27]. Fed by dual modes of coplanar waveguide, dual orthogonal linear polarizations are excited in the slot and controlled by two PIN diodes. The antenna is composed by a rectangular slot, a coplanar waveguide (CPW), a capacitively coupled strip, and two PIN diodes. The rectangular slot

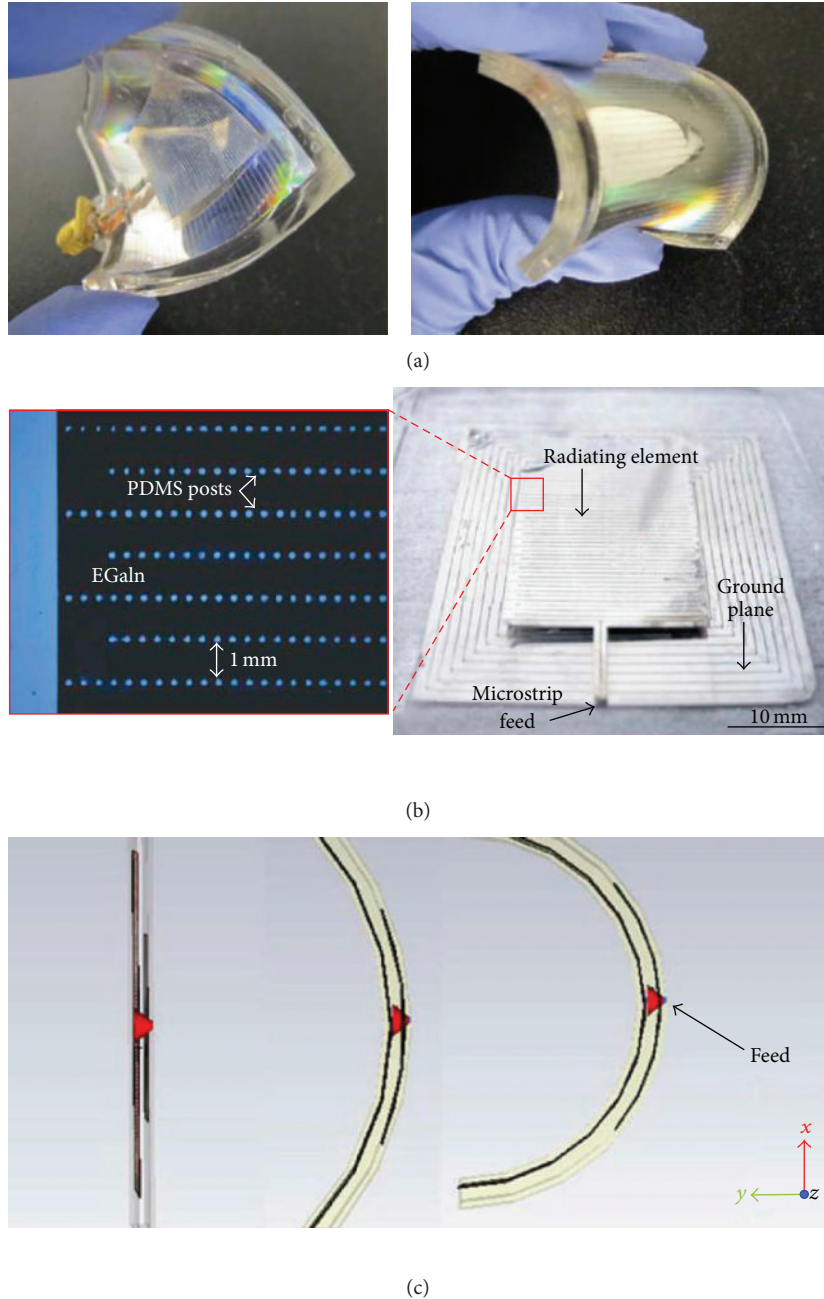


FIGURE 7: (a) Reconfigurable liquid metal alloy microstrip patch antenna. (b) The patch antenna and ground plane. (c) Cross-sectional view of the conformal configurations: (right) static, (middle) curved to a 25.4 mm radius, and (left) curved to a 12.7 mm radius (with permission from IEEE).

with the dimensions of  $53 \times 50 \text{ mm}^2$  serves as the radiation aperture, etched in the front side of FR4 ( $\epsilon_r = 4.4$ ,  $\tan\delta = 0.01$ ). A switchable feed, including a C-shaped capacitively coupled strip at the back side and a CPW at the front side through, is controlled by two PIN diodes. The front side of fabricated antenna topology is shown in Figure 8(a). The back side of fabricated antenna structure is shown in Figure 8(b). The bias circuit of the feed is shown in Figure 8(c). And the geometry of the slot antenna is shown in Figure 8(d). When PIN1 is “on” and PIN2 is “off,” the antenna is fed through the C-shaped strip, which is capacitively coupled to the CPW.

As a result, the horizontal polarization of the slot is excited. When PIN1 is “off” and PIN2 is “on,” the vertical polarization is excited by typical CPW feed structure. Dual orthogonal polarizations are achieved by dual orthogonal modes of CPW independently, making the feed structure compact.

4.2. *Circular Polarization Reconfigurable Antennas.* A circularly polarized reconfigurable microstrip array antenna with conical-beam radiation is shown in Figure 9 [39]. The array antenna structure consists of four L-shaped patch elements

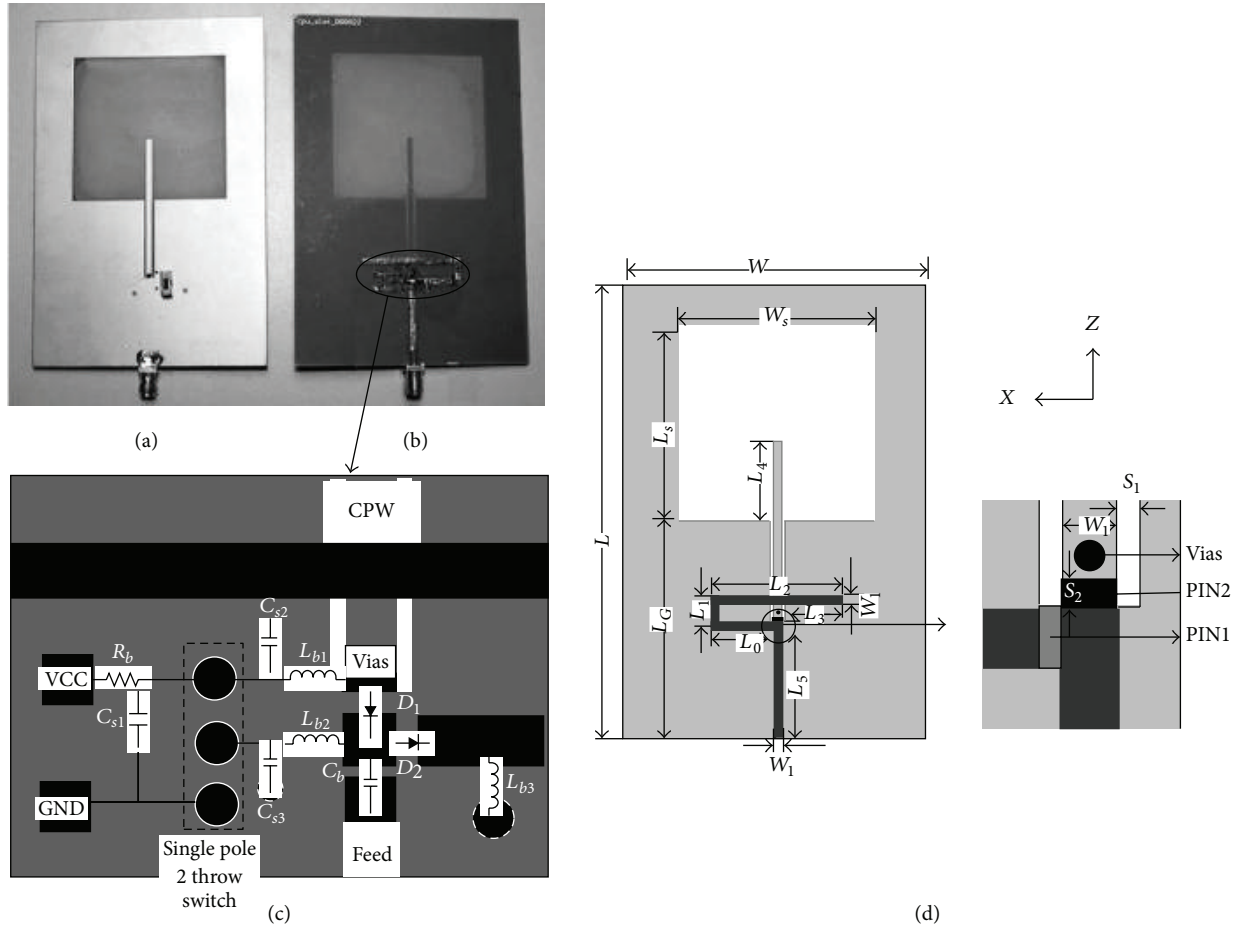


FIGURE 8: (a) Front side of fabricated polarization reconfigurable antenna. (b) Back side. (c) Bias circuit of the feed. (d) Geometric structure (with permission from John Wiley and Sons).

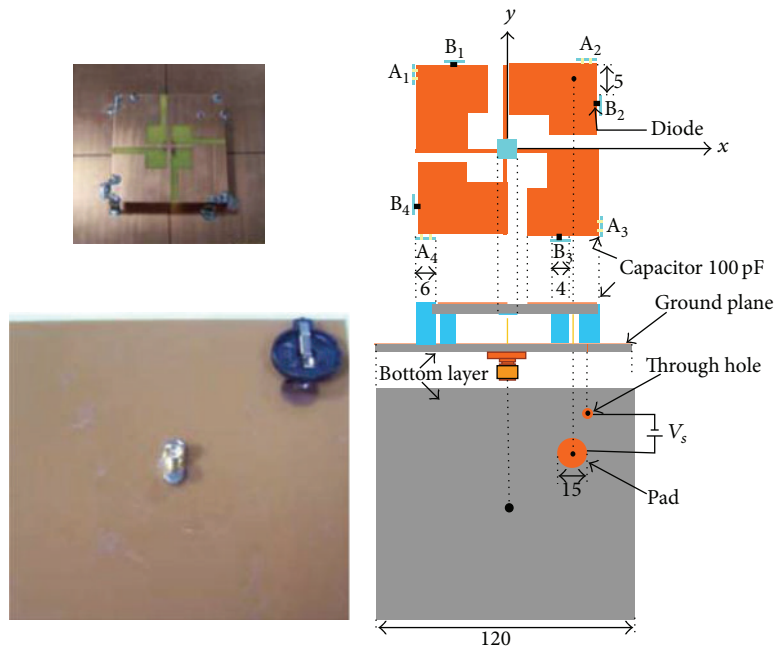


FIGURE 9: Layout of a reconfigurable CP microstrip array and the finished prototype (with permission from IEEE).

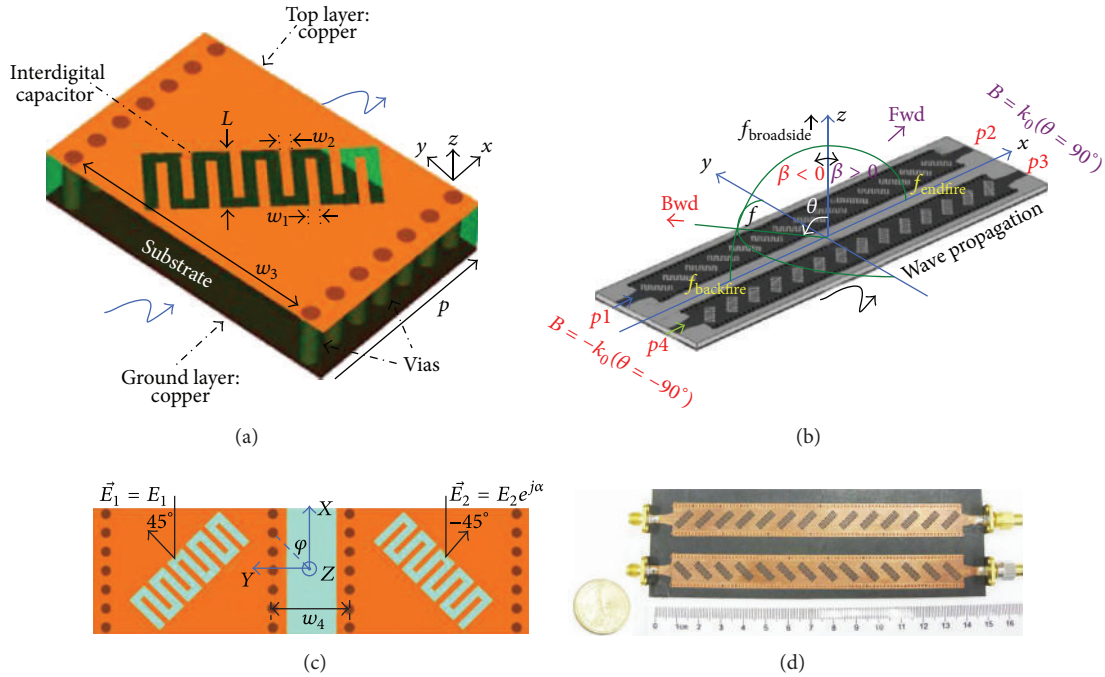


FIGURE 10: Polarization reconfigurable CRLH-SIW antenna. (a) Single radiating element. (b) Two-element unit cell of the whole structure. (c) Overall LW antenna prototype. (d) fabricated antenna (with permission from IEEE).

arranged in a square-ring formation. Each patch is shorted to the ground plane through conducting walls. With a top-loaded monopole feed, two orthogonal resonant modes, loop mode and monopole mode, can be excited simultaneously. When the monopole mode and the loop mode are properly coupled, the microstrip array can generate a CP radiation. By controlling the frequency, the antenna can switch between LHCP and RHCP. In addition the array has the characteristic of omnidirectional radiation and conical beam.

**4.3. Mixed Polarization Reconfigurable Antennas.** A composite right/left-handed (CRLH) leaky-wave (LW) antenna with flexible polarization is presented in [41]. The leaky transmission line (TL) is a planar passive circuit built using the substrate integrated waveguide technology. It consists of two symmetrical waveguide lines loaded with series interdigital capacitors which radiate orthogonal 45 linearly polarized waves, as shown in Figure 10. The configuration of single radiating element is shown in Figure 10(a). Two-element unit cell of the whole structure is shown in Figure 10(b). The overall LW antenna prototype is shown in Figure 10(c). Photograph of the fabricated LW antennas is shown in Figure 10(d). The antenna is able to generate arbitrary different polarization states by changing the way of excitation, including LP and CP. This leaky TL is fabricated by the standard printed-circuit board process. Two broadband couplers are also designed and fabricated for the specified excitation purpose. Six different polarization states, including four LP cases (horizontal, vertical, and  $\pm$ slant  $45^\circ$ ) and two CP ones (left

hand and right hand), can be realized. The LW structure shows some desirable merits, such as the simplicity in design, low-cost fabrication, and beam-steering and polarization-flexible capabilities, providing a high degree of flexibility for the real application.

## 5. Multipattern-Multipolarization Mixed Reconfigurable Antennas

This type of antennas realizes multipattern and multipolarization characteristics by using one reconfigurable antenna. A novel reconfigurable microstrip antenna with radiation pattern selectivity and polarization diversity is discussed in [57]. As shown in Figure 11(a), A four-way power divider made by three Wilkinson power dividers and interconnected with switches (switch A and switch B) is designed to feed-four-rectangular-radiating-patchantenna. By controlling the state of the switches, the antenna characteristics can be changed into two modes. When switch A is closed and switch B is open, the four rectangular radiating patches are excited by four sources with equal amplitude and phase. A metamaterial antenna with conical beam and linear polarization is achieved. When switch A is open and switch B is closed, four sources with equal amplitude but 90-phase difference for each adjacent output lead to a wideband antenna with broadside beam and circular polarization. The photographs of measurement setup and fabricated antenna are shown in Figure 11(b). This single-port antenna is useful for terrestrial land mobile or other wireless applications.

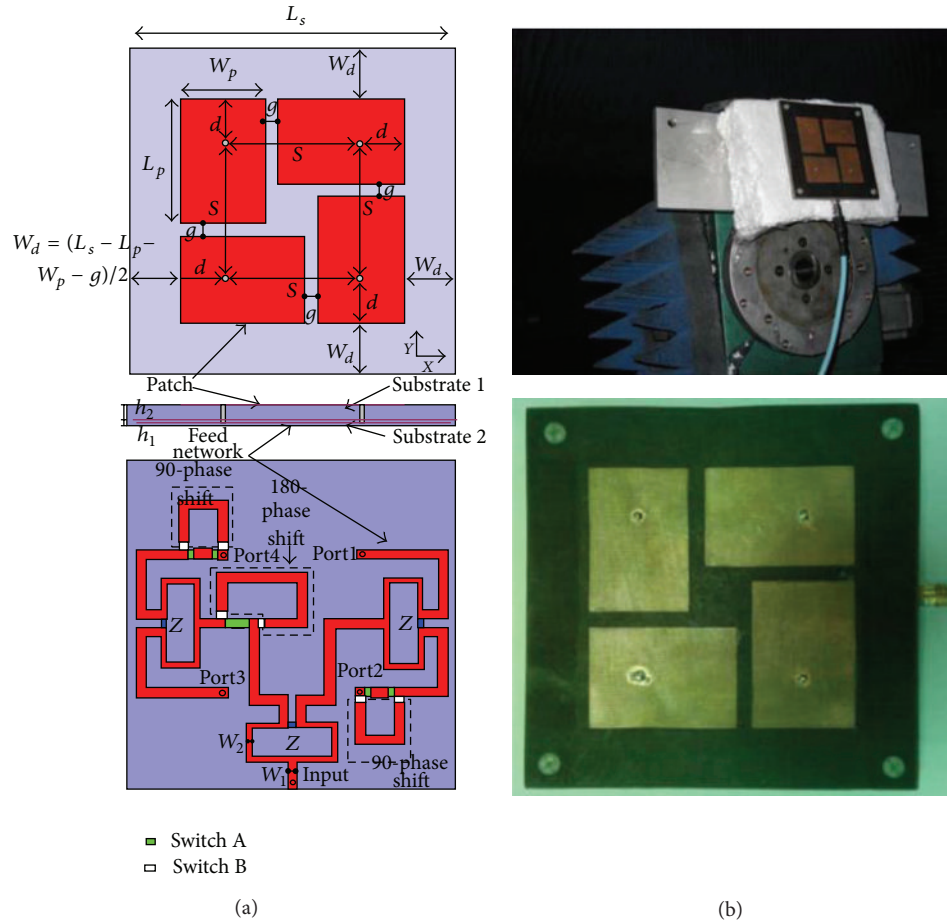


FIGURE 11: (a) The pattern and polarization reconfigurable microstrip antenna. (top) Top view. (middle) Side view. (bottom) Bottom view. (b) Measurement setup photograph and the fabricated antenna (with permission from IEEE).

## 6. Comparison between Multipattern and Multipolarization Antennas

As shown in Figure 12, multipattern and multipolarization antennas described above can be divided into two types according to the method of feed: connected feed or spatial feed. The classification criteria are whether the feed of the antenna is connected to the radiator or not. The reconfigurable reflectarray antennas and lens antennas, which are classified as spatial feed, generally fed by horn antennas or others, as described in [10, 13, 15, 25, 26, 29, 61]. Most antennas presented in this paper have a connected feed. Compared with the connected-feed antennas, the spatial-feed reconfigurable reflectarray antennas and lens antennas have the advantages of the gain of a reflector antenna changeable with the flexibility of an array, feed losses and layout problems eliminated through the use of a spatial feed, and system amenable to closed-loop control. However, they have limitations of scanning range, feed blockage, and profile.

The reconfigurable antennas with a connected feed include planer antennas and nonplanar antennas. The nonplanar reconfigurable antennas in the form of waveguide

antenna and cubic antenna are discussed in [19, 36], respectively. They are able to avoid outside interference and radiation loss due to their simple closed structure. Nevertheless, paralleling with planar reconfigurable antenna, they are more difficult to integrate with the circuit because of nonplanar structure and are less popular in reconfigurable area due to inflexible structure.

The planar reconfigurable antennas fed by coaxial or coplanar waveguide are mainly made up of microstrip antennas [7–9, 33–35, 37–39, 42–46, 48–52, 57–60], substrate integrated waveguide (SIW) antennas [11, 12, 40, 41], and monopole or dipole antennas [3–5, 16, 17, 20, 53, 55]. The microstrip antennas are widely used in reconfigurable antennas with the advantages of small size, light weight, low profile, and ease of integration. The SIW antennas have both the microstrip antenna's advantages of low profile and being easy to integrate and the waveguide antenna's merits of low radiation loss and high efficiency. But, compared to the microstrip-reconfigurable antenna, they are more difficult to process and have lower flexibility. The monopole or dipole antennas have flexible structure, but their ordinary is gain lower than SIW antennas.

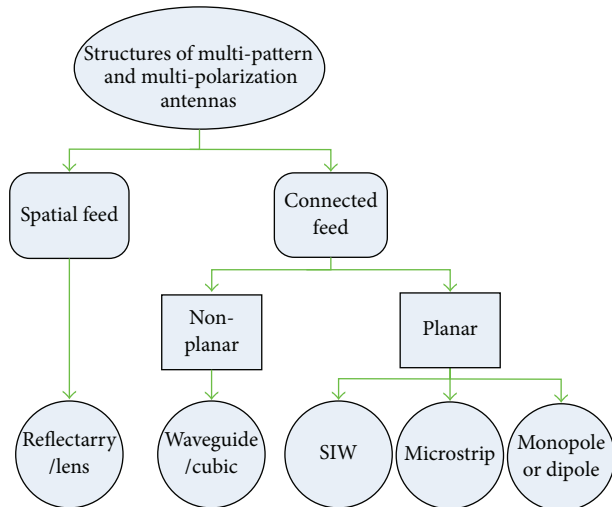


FIGURE 12: The different structures of multipattern and multipolarization antennas.

## 7. Applications

The reconfigurable antennas with multipattern and multipolarization have been used in both aerospace and terrestrial wireless communication to improve spectrum efficiency, such as wireless systems in dynamic scenarios, adaptive beam scanning, and MIMO systems. In dynamic scenarios, it is necessary to reconfigure the antenna radiation pattern to maintain high data rate, serve a new coverage zone, and limit fading in rainy areas at all possible frequency bands of operation. The dynamic scenarios including satellite and terminal tracking are discussed in [26, 50, 62–64]. In the adaptive beam scanning system, the antenna should automatically change its radiation beam direction corresponding to the various propagation environments or moving target, such as in the system of radar and remote sensing [65–68]. A MIMO system employs multiple antennas at both the transmitter and receiver front ends. Pattern and polarization reconfigurable antennas are widely studied and adopted in MIMO systems for their intrinsic pattern and polarization diversity advantage in mitigating the multipath fading and increasing the channel capacity, especially in pattern and polarization varied environments. The MIMO system with reconfigurable antennas is able to actively manage channel correlation, diversity, and interference [9, 17, 18, 27, 31, 59, 69, 70].

## 8. Vision and Goal

Even though the research on the multipattern and multipolarization antennas has got some achievements, we still have a long way to go. Until now, the reconfigurable antennas which have been studied and researched are not smart enough that they are not completely multifunctional and software controlled with machine. In addition, the antennas still only play a role of the transducers. A very interesting goal is that we can create field programmable antenna system which enjoys

the same flexibility as other field-programmable devices. In the field-programmable antenna system, the reconfigurable antennas can detect changes in their RF environment and react accordingly. If such system is realized, the antennas are evolved from simple transducers to advanced wave processors, along with the advantages of the utilization of radiation pattern selectivity and polarization diversity to transmit over already “busy” frequencies. And the reconfigurable antennas will play more an important role in aerospace and terrestrial applications.

## 9. Conclusion

This paper presents an overview on the multipattern and multipolarization antennas. The concepts, characteristics, and typical antennas of radiation patterns and polarizations are introduced. A comparison between different multipattern and multipolarization antennas with different structures and working mechanisms are also discussed. The reconfigurable antennas can be well applied to dynamic scenarios, adaptive beam scanning, and MIMO systems. The goal in the future work is to realize the field programmable antenna system to evolve antennas from simple transducers to advanced wave processors.

## Acknowledgments

This work was supported in part by the National Science Foundation of China and NSAF under their joint Grant no. 11076031.

## References

- [1] D. H. Schaubet, F. G. Farrar, S. T. Hayes et al., “Frequency-agile polarization diverse microstrip antennas and frequency scanned arrays,” U.S. Patent 4,367,474, Jan. 1983.
- [2] C. G. Christodoulou, Y. Tawk, S. A. Lane, and S. R. Erwin, “Reconfigurable antennas for wireless and space applications,” *Proceedings of the IEEE*, vol. 100, no. 7, pp. 2250–2261, 2012.
- [3] W. S. Kang, J. A. Park, and Y. J. Yoon, “Simple reconfigurable antenna with radiation pattern,” *Electronics Letters*, vol. 44, no. 3, pp. 182–183, 2008.
- [4] M. I. Lai, T. Y. Wu, J. C. Hsieh, C. H. Wang, and S. K. Jeng, “Design of reconfigurable antennas based on an L-shaped slot and PIN diodes for compact wireless devices,” *IET Microwaves, Antennas and Propagation*, vol. 3, no. 1, pp. 47–54, 2009.
- [5] L. G. Maloratsky, “Switched directional/omnidirectional antenna module for amplitude monopulse systems,” *IEEE Antennas and Propagation Magazine*, vol. 51, no. 5, pp. 90–102, 2009.
- [6] F. Peruani and A. Maiti, “Modeling broadcasting using omnidirectional and directional antenna in delay tolerant networks as an epidemic dynamics,” *IEEE Journal on Selected Areas in Communications*, vol. 28, no. 4, pp. 524–531, 2010.
- [7] M. Ding, R. Jin, J. Geng, X. Guo, and J. Chen, “A high-gain dual-band directional/omnidirectional reconfigurable antenna for WLAN systems,” *International Journal of RF and Microwave Computer-Aided Engineering*, vol. 18, no. 3, pp. 225–232, 2008.
- [8] M. Donelli, R. Azaro, L. Fimognari, and A. Massa, “A planar electronically reconfigurable wi-fi band antenna based on a

- parasitic microstrip structure," *IEEE Antennas and Wireless Propagation Letters*, vol. 6, pp. 623–626, 2007.
- [9] D. Piazza, M. D'Amico, and K. R. Dandekar, "Performance improvement of a wideband MIMO system by using two-port RLWA," *IEEE Antennas and Wireless Propagation Letters*, vol. 8, pp. 830–834, 2009.
- [10] J. Y. Lau and S. V. Hum, "A planar reconfigurable aperture with lens and reflectarray modes of operation," *IEEE Transactions on Microwave Theory and Techniques*, vol. 58, no. 12, pp. 3547–3555, 2010.
- [11] A. Suntives and S. V. Hum, "A fixed-frequency beam-steerable half-mode substrate integrated waveguide leaky-wave antenna," *IEEE Transactions on Antennas and Propagation*, vol. 60, no. 5, pp. 2540–2544, 2012.
- [12] A. Suntives and S. V. Hum, "An electronically tunable half-mode substrate integrated waveguide leaky-wave antenna," in *Proceedings of the 5th European Conference on Antennas and Propagation (EUCAP '11)*, pp. 3670–3674, April 2011.
- [13] C. Liu and S. V. Hum, "An electronically tunable single-layer reflectarray antenna element with improved bandwidth," *IEEE Antennas and Wireless Propagation Letters*, vol. 9, pp. 1241–1244, 2010.
- [14] L. Boccia, I. Russo, G. Amendola, and G. Di Massa, "Multilayer antenna-filter antenna for beam-steering transmit-array applications," *IEEE Transactions on Microwave Theory and Techniques*, vol. 60, no. 7, pp. 2287–2300, 2012.
- [15] W. Hu, M. Y. Ismail, R. Cahill et al., "Liquid-crystal-based reflectarray antenna with electronically switchable monopulse patterns," *Electronics Letters*, vol. 43, no. 14, pp. 744–745, 2007.
- [16] C. J. Panagamuwa, A. Chauraya, and J. C. Vardaxoglou, "Frequency and beam reconfigurable antenna using photoconducting switches," *IEEE Transactions on Antennas and Propagation*, vol. 54, no. 2, pp. 449–454, 2006.
- [17] D. Piazza, N. J. Kirsch, A. Forenza, R. W. Heath, and K. R. Dandekar, "Design and evaluation of a reconfigurable antenna array for MIMO systems," *IEEE Transactions on Antennas and Propagation*, vol. 56, no. 3, pp. 869–881, 2008.
- [18] Z. Li, Z. Du, and K. Gong, "Compact reconfigurable antenna array for adaptive MIMO systems," *IEEE Antennas and Wireless Propagation Letters*, vol. 8, pp. 1317–1320, 2009.
- [19] J. Sarrazin, Y. Mahé, S. Avrillon, and S. Toutain, "Pattern reconfigurable cubic antenna," *IEEE Transactions on Antennas and Propagation*, vol. 57, no. 2, pp. 310–317, 2009.
- [20] H. Eslami, C. P. Sukumar, D. Rodrigo et al., "Reduced overhead training for multi reconfigurable antennas with beam-tilting capability," *IEEE Transactions on Wireless Communications*, vol. 9, no. 12, pp. 3810–3821, 2010.
- [21] Y. Yang, X. Zhao, and T. Wang, "Design of arbitrarily controlled multi-beam antennas via optical transformation," *Journal of Infrared, Millimeter, and Terahertz Waves*, vol. 30, no. 4, pp. 337–348, 2009.
- [22] A.-H. Tsai, L.-C. Wang, J.-H. Huang, and R.-B. Hwang, "Stable subchannel allocation for OFDMA femtocells with switched multi-beam directional antennas," in *Proceedings of the IEEE Global Telecommunications Conference (GLOBECOM '11)*, pp. 1–6, December 2011.
- [23] G. Krieger, N. Gebert, and A. Moreira, "Multidimensional waveform encoding: a new digital beamforming technique for synthetic aperture radar remote sensing," *IEEE Transactions on Geoscience and Remote Sensing*, vol. 46, no. 1, pp. 31–46, 2008.
- [24] G. J. Hayes, J.-H. So, A. Qusba, M. D. Dickey, and G. Lazzi, "Flexible liquid metal alloy (EGaIn) microstrip patch antenna," *IEEE Transactions on Antennas and Propagation*, vol. 60, no. 5, pp. 2151–2156, 2012.
- [25] M. F. Jamlos, T. A. Rahman, and M. R. Kamarudin, "The effects of air stacked on reconfigurable quadratic slots antenna for WiMAX and 4G applications," *Microwave and Optical Technology Letters*, vol. 54, no. 9, pp. 2139–2144, 2012.
- [26] T. Takano, K. Miura, M. Natori et al., "Deployable antenna with 10-m maximum diameter for space use," *IEEE Transactions on Antennas and Propagation*, vol. 52, no. 1, pp. 2–11, 2004.
- [27] Y. Li, Z. Zhang, J. Zheng, and Z. Feng, "Channel capacity study of polarization reconfigurable slot antenna for indoor MIMO system," *Microwave and Optical Technology Letters*, vol. 53, no. 6, pp. 1209–1213, 2011.
- [28] B. Q. Wu and K. M. Luk, "The design of wideband reconfigurable antenna with four polarizations," in *Proceedings of the 39th European Microwave Conference (EuMC '09)*, pp. 759–762, September 2009.
- [29] A. Clemente, L. Dussopt, R. Sauleau et al., "1-bit reconfigurable unit cell based on PIN diodes for transmit-array applications in X-band," *IEEE Transactions on Antennas and Propagation*, vol. 60, no. 5, pp. 2260–2269, 2012.
- [30] G. Wang, R. Bairavasubramanian, B. Pan, and J. Papapolymerou, "Radiofrequency MEMS-enabled polarisation-reconfigurable antenna arrays on multilayer liquid crystal polymer," *IET Microwave Antenna and Propagation*, vol. 5, no. 13, pp. 1594–1599, 2011.
- [31] A. Grau, J. Romeu, M. J. Lee, S. Blanch, L. Jofre, and F. de Flaviis, "A dual-Linearly-polarized MEMS-reconfigurable antenna for narrowband MIMO communication systems," *IEEE Transactions on Antennas and Propagation*, vol. 58, no. 1, pp. 4–17, 2010.
- [32] P. Seongmin and S. Imseob, "A miniaturized switchable circularly polarized patch antenna controlled by a single diode operation," *Microwave and Optical Technology Letters*, vol. 54, no. 10, pp. 2375–2378, 2012.
- [33] K. F. Tong and J. Huang, "New proximity coupled feeding method for reconfigurable circularly polarized microstrip ring antennas," *IEEE Transactions on Antennas and Propagation*, vol. 56, no. 7, pp. 1860–1866, 2008.
- [34] W. S. Yoon, J. W. Baik, H. S. Lee, S. Pyo, S. M. Han, and Y. S. Kim, "A reconfigurable circularly polarized microstrip antenna with a slotted ground plane," *IEEE Antennas and Wireless Propagation Letters*, vol. 9, pp. 1161–1164, 2010.
- [35] P. Seongmin and S. Youngje, "A circular polarized microstrip antenna with an arrow-shaped slotted ground," *Microwave and Optical Technology Letters*, vol. 54, no. 1, pp. 271–273, 2012.
- [36] J. A. Ruiz-Cruz, M. M. Fahmi, S. A. Fouladi, and R. R. Mansour, "Waveguide antenna feeders with integrated reconfigurable dual circular polarization," *IEEE Transactions on Microwave Theory and Techniques*, vol. 59, no. 12, pp. 3365–3374, 2011.
- [37] S. H. Hsu and K. Chang, "A novel reconfigurable microstrip antenna with switchable circular polarization," *IEEE Antennas and Wireless Propagation Letters*, vol. 6, pp. 160–162, 2007.
- [38] A. Khaleghi and M. Kamyab, "Reconfigurable single port antenna with circular polarization diversity," *IEEE Transactions on Antennas and Propagation*, vol. 57, no. 2, pp. 555–559, 2009.
- [39] J. S. Row and M. C. Chan, "Reconfigurable circularly-polarized patch antenna with conical beam," *IEEE Transactions on Antennas and Propagation*, vol. 58, no. 8, pp. 2753–2757, 2010.

- [40] Y. J. Cheng, W. Hong, and K. Wu, "Millimeter-wave half mode substrate integrated waveguide frequency scanning antenna with quadri-polarization," *IEEE Transactions on Antennas and Propagation*, vol. 58, no. 6, pp. 1848–1855, 2010.
- [41] Y. Dong and T. Itoh, "Millimeter-Wave half mode substrate integrated waveguide frequency scanning antenna with quadri-polarization," *IEEE Transactions on Antennas and Propagation*, vol. 60, no. 2, pp. 760–771, 2012.
- [42] X.-X. Yang, B.-C. Shao, F. Yang et al., "A polarization reconfigurable patch antenna with loop slots on the ground plane," *IEEE Antennas and Wireless Propagation Letters*, vol. 11, pp. 69–72, 2012.
- [43] Y. F. Wu, C. H. Wu, D. Y. Lai, and F. C. Chen, "A reconfigurable quadri-polarization diversity aperture-coupled patch antenna," *IEEE Transactions on Antennas and Propagation*, vol. 55, no. 3, pp. 1009–1012, 2007.
- [44] R. H. Chen and J. S. Row, "Single-fed microstrip patch antenna with switchable polarization," *IEEE Transactions on Antennas and Propagation*, vol. 56, no. 4, pp. 922–926, 2008.
- [45] O. H. Karabey, S. Bildik, and S. Strunck, "Continuously polarisation reconfigurable antenna element by using liquid crystal based tunable coupled line," *Electronics Letters*, vol. 48, no. 3, pp. 141–143, 2012.
- [46] B. Kim, B. Pan, S. Nikolaou, Y. S. Kim, J. Papapolymerou, and M. M. Tentzeris, "A novel single-feed circular microstrip antenna with reconfigurable polarization capability," *IEEE Transactions on Antennas and Propagation*, vol. 56, no. 3, pp. 630–638, 2008.
- [47] H. Emami, N. Sarkhosh, and E. R. L. Lara, "Reconfigurable photonic feed for sinuous antenna," *Journal of Light Wave Technology*, vol. 30, no. 16, pp. 2725–2732, 2012.
- [48] P. Y. Qin, A. R. Weily, Y. J. Guo, and C. H. Liang, "Polarization reconfigurable U-slot patch antenna," *IEEE Transactions on Antennas and Propagation*, vol. 58, no. 10, pp. 3383–3388, 2010.
- [49] M. S. Nishamol, V. P. Sarin, D. Tony et al., "An electronically reconfigurable microstrip antenna with switchable slots for polarization diversity," *IEEE Transactions on Antennas and Propagation*, vol. 59, no. 9, pp. 3424–3427, 2011.
- [50] J. H. Lim, G. T. Back, and T. Y. Yun, "Polarization-diversity cross-shaped patch antenna for satellite-DMB systems," *ETRI Journal*, vol. 32, no. 2, pp. 312–318, 2010.
- [51] X. Yuan, Z. Li, D. Rodrigo et al., "A parasitic layer-based reconfigurable antenna design by multi-objective optimization," *IEEE Transactions on Antennas and Propagation*, vol. 60, no. 6, pp. 2690–2701, 2012.
- [52] X.-S. Yang, B.-Z. Wang, S.-H. Yeung et al., "Circularly polarized reconfigurable crossed-vagi patch antenna," *IEEE Antennas and Propagation Magazine*, vol. 53, no. 5, pp. 65–80, 2011.
- [53] Y. Dong and T. Itoh, "Planar ultra-wideband antennas in ku- and k-band for pattern or polarization diversity applications," *IEEE Transactions on Antennas and Propagation*, vol. 60, no. 6, pp. 2886–2895, 2012.
- [54] B. Poussot, J. M. Laheurte, L. Cirio, and O. Picon, "Diversity gain measurements of a reconfigurable antenna with switchable polarization," *Microwave and Optical Technology Letters*, vol. 49, no. 12, pp. 3154–3158, 2007.
- [55] B. Poussot, J. M. Laheurte, L. Cirio, O. Picon, D. Delcroix, and L. Dussopt, "Diversity measurements of a reconfigurable antenna with switched polarizations and patterns," *IEEE Transactions on Antennas and Propagation*, vol. 56, no. 1, pp. 31–38, 2008.
- [56] P. Daniele and D. Michele, "Pattern and polarization reconfigurable CRLH leaky wave antenna," in *Proceedings of the 4th European Conference on Antennas and Propagation (EuCAP '10)*, pp. 1–5, April 2010.
- [57] W. Cao, B. Zhang, A. Liu et al., "A reconfigurable microstrip antenna with radiation pattern selectivity and polarization diversity," *IEEE Antennas and Wireless Propagation Letters*, vol. 11, pp. 453–456, 2012.
- [58] W. Chen, J. Sun, and Z. Feng, "A novel compact reconfigurable polarization and pattern antenna," *Microwave and Optical Technology Letters*, vol. 49, no. 11, pp. 2802–2805, 2007.
- [59] D. Piazza, P. Mookiah, M. D'Amico, and K. R. Dandekar, "Experimental analysis of pattern and polarization reconfigurable circular patch antennas for MIMO systems," *IEEE Transactions on Vehicular Technology*, vol. 59, no. 5, pp. 2352–2362, 2010.
- [60] W. L. Liu, T. R. Chen, S. H. Chen, and J. S. Row, "Reconfigurable microstrip antenna with pattern and polarisation diversities," *Electronics Letters*, vol. 43, no. 2, pp. 77–78, 2007.
- [61] A. G. Besoli and F. D. Flaviis, "A multifunctional reconfigurable pixelated antenna using mems technology on printed circuit board," *IEEE Transactions on Antennas and Propagation*, vol. 59, no. 12, pp. 4413–4424, 2011.
- [62] M. Ali, A. T. M. Sayem, and V. K. Kunda, "A reconfigurable stacked microstrip patch antenna for satellite and terrestrial links," *IEEE Transactions on Vehicular Technology*, vol. 56, no. 2, pp. 426–435, 2007.
- [63] M. D. van de Burgwal, K. C. Rovers, K. C. H. Blom et al., "Mobile satellite reception with a virtual satellite dish based on a reconfigurable multi-processor architecture," *Microprocessors and Microsystems*, vol. 35, no. 8, pp. 716–728, 2011.
- [64] J. A. Lee, S. B. Byun, J. H. Lim, and T. Y. Yun, "Reconfigurable antenna for wideband code division multiple access and korean satellite digital multimedia broadcasting controlled by PIN-diodes," *Microwave and Optical Technology Letters*, vol. 49, no. 6, pp. 1334–1337, 2007.
- [65] M. Alshershby and J. Q. Lin, "Reconfigurable plasma antenna produced in air by laser-induced filaments: passive radar application," in *Proceedings of the International Conference on Optoelectronics and Microelectronics (ICOM '12)*, pp. 364–371, August 2012.
- [66] N. Romano, G. Prisco, and F. Soldovieri, "Design of a reconfigurable antenna for ground penetrating radar applications," *Progress in Electromagnetics Research*, vol. 94, pp. 1–18, 2009.
- [67] F. Soldovieri and N. Romano, "The mutual interaction between the reconfigurable transmitting and receiving antennas in ground penetrating radar surveys," *Journal of Electromagnetic Waves and Applications*, vol. 23, no. 14–15, pp. 1919–1928, 2009.
- [68] M. F. Jamlos, O. A. Aziz, T. A. Rahman et al., "A reconfigurable radial line slot array (RLSA) antenna for beam shape and broadside application," *Journal of Electromagnetic Waves and Applications*, vol. 24, no. 8–9, pp. 1171–1182, 2010.
- [69] P. A. Martin, P. J. Smith, and R. Murch, "Improving space-time code performance in slow fading channels using reconfigurable antennas," *IEEE Communications Letters*, vol. 16, no. 4, pp. 494–497, 2012.
- [70] F. Fazel, A. Grau, H. Jafarkhani, and F. de Flaviis, "Space-time-state block coded MIMO communication systems using reconfigurable antennas," *IEEE Transactions on Wireless Communications*, vol. 8, no. 12, pp. 6019–6029, 2009.